Hydrogen Incorporation in Rutile- and Perovskite-Structured Minerals and Their Analogues

Thesis by

William Richard Palfey

In Partial Fulfillment of the Requirements for
the degree of
Doctor of Philosophy in Geochemistry

CALIFORNIA INSTITUTE OF TECHNOLOGY
Pasadena, California

2024
Defended May 24, 2024

William Richard Palfey
ORCID: 0000-0002-9555-7877

ACKNOWLEDGEMENTS

First, I would like to thank my advisor, Prof. George Rossman. I have greatly appreciated your enthusiasm for science and the many interesting research discussions we've had during my time at Caltech. I am extremely grateful for the space you gave me to pursue and develop new ideas, and it has been an absolute privilege to have you as a mentor.

I would also like to thank the other members of my thesis committee: Prof. Paul Asimow, Prof. Bill Goddard, Prof. Jennifer Jackson, and Prof. John Eiler. In particular, I want to thank Bill for his generosity with his time and resources, which made all of the computational components of my research possible, and heavily influenced the direction of my work. I would also like to thank Paul for being my committee chair and for helpful research discussions, Jennifer for bringing me into her lab as a collaborator, and John for providing crucial lab space throughout my whole PhD.

There were many other individuals who I collaborated with or who otherwise provided guidance and support in my research efforts, including Nami Kitchen, Dr. Son-Jong Hwang, Dr. Cullen Quine, Dr. Channing Ahn, Dr. Mike Baker, Charles Musgrave, Dr. Olivia Pardo, Dr. Paul Oyala, and Dr. Lena Wolff. The work outlined in the following chapters was certainly not the product of a single lab, and I am deeply appreciative of everything you've done.

I was fortunate enough to have been welcomed into several other research groups during my time at Caltech, including those of Prof. Bill Goddard, Prof. Jennifer Jackson, Prof. Katherine Faber, and Prof. Brent Fultz. Thank you all for being excellent colleagues and friends.

I am also thankful to the staff and admin in both GPS and APhMS including Julie Lee, Mark Garcia, Chelsea Terrill, Claire Fredrickson, Christy Jenstad, and Katie Pichotta.

I also need to thank my friends from Caltech and beyond. From the members of the Rossman lab, to my first-year cohort, officemates, roommates, support groups, companions in mineral collecting, and friends back home, you have all made my experience in grad school truly memorable.

Lastly, I would like to acknowledge my loved ones. To Celia, your love and support has meant so much these last few years. You've been by my side through the many ups and downs of my PhD, and I can't imagine having gone on this journey without you. To my family, who has always encouraged me to pursue my academic interests, thank you for everything. Thank you to my sister, Dagmar, who's been my greatest lifelong friend, and to my mom, who endured many years of finding rocks in unusual places, and whose strength inspires me every day. Finally, I would like to thank my dad. You were only able to witness the very start of my PhD, but I know that this wouldn't have been possible without you, too.

This work was funded by the National Science Foundation (Grants EAR-1322082 and EAR-2149559) and the Liquid Sunlight Alliance, which is supported by the U.S. Department of Energy, Office of Science, Office of Basic Energy Sciences, Fuels from Sunlight Hub, under Grant DE-SC0021266

ABSTRACT

For several decades now, it has been known that large quantities of hydrogen can be stored in the earth's mantle. This hydrogen, which is disseminated as defect components in nominally anhydrous minerals (NAMs), can have an outsized influence on minerals' bulk properties, potentially impacting planetary-scale processes. However, a description of how this hydrogen is sequestered in NAMs — its distribution between phases, its inhomogeneity between different mantle regimes, and the variety of defects involved — has evolved significantly with time. Deciphering hydrogen's role in the deep earth requires a detailed understanding of how hydrogen incorporates into mantle phases, beginning at an atomistic and structural level. Unfortunately, for a variety of reasons, directly measuring the crystallographic positions of hydrogen in most NAMs represents an exceptionally high technical barrier. Thus, hydrogen's structural state is, in many phases, incompletely understood. One approach for addressing this is to incorporate the use of computational methods like density functional theory (DFT) in the interpretation of analytical methods that can provide indirect structural information, like Fourier transform infrared spectroscopy (FTIR). This is the methodology employed by the work outlined in subsequent chapters.

This thesis focuses on two specific mineral structures found within the deep earth — the rutile and perovskite structures — and explores some of the many possible hydrogen defect states in these phases. These include not only the conventionally considered hydroxyl (OH^-) group, but also hydride (H^-), an anionic form of hydrogen whose role in the mantle has yet to be considered in detail. The predictive and interpretive capabilities of DFT are utilized in studies on stishovite, rutile-type TiO_2, $SrTiO_3$, and davemaoite to both elucidate hydrogen's incorporated state in these phases and make predictions about yet-to-be-observed hydrogen defects. Detailed spectroscopic studies on rutile-type TiO_2 and $SrTiO_3$ perovskite provide new insights into both hydrogen and non-hydrogen related defect structures in these materials, with implications for future studies of NAMs.

PUBLISHED CONTENT AND CONTRIBUTIONS

[1] Palfey, W. R.; Rossman, G. R.; Goddard, W. A. Structure, Energetics, and Spectra for the Oxygen Vacancy in Rutile: Prominence of the Ti–H $_{O}$ –Ti Bond. *J. Phys. Chem. Lett.* **2021**, *12* (41), 10175–10181. https://doi.org/10.1021/acs.jpclett.1c02850.

W.R. Palfey participated in designing the study, writing the manuscript, and carried out the DFT calculations.

[2] Palfey, W. R.; Rossman, G. R.; Goddard III, W. A. Behavior of Hydrogarnet-Type Defects in Hydrous Stishovite at Various Temperatures and Pressures. *Journal of Geophysical Research: Solid Earth* **2023**, *128*. https://doi.org/10.1029/2022JB024980.

W.R. Palfey participated in designing the study, writing the manuscript, and carried out the DFT calculations.

[3] Palfey, W. R.; Hwang, S.J.; Oyala, P.H., Rossman. G.R. Defect chemistry of H_2-reduced rutile crystals: insights from infrared and ^{1}H NMR spectroscopy. *In Preparation.* **n.d.**

W.R. Palfey participated in designing the study and writing the manuscript, carried out the sample treatments and preparation for measurements, and carried out FTIR measurements.

[4] Palfey, W. R.; The spectroscopy of hydride in single crystals of $SrTiO_3$. *In Preparation.* **n.d.**

W.R. Palfey participated in designing the study and writing the manuscript, carried out the sample treatments and preparation for measurements, carried out FTIR and visible light measurements, and performed DFT calculations.

[5] Palfey, W. R.; Investigation of possible hydrogen coupling to K and Na in Davemaoite. *In Preparation.* **n.d.**

W.R. Palfey participated in designing the study, writing the manuscript, and carried out the DFT calculations.

TABLE OF CONTENTS

LIST OF ILLUSTRATIONS

Number *Page*

LIST OF TABLES

Number *Page*

NOMENCLATURE

This thesis makes use of Kröger-Vink notation, which may be confusing for those unaccustomed to it. A brief description of the notation:

In this notation, defects are described with respect to lattice site and relative charge. Defect formation is written like a chemical reaction, where charges must balance out on either side. Each component of the equation has the style:

$$A_B^C$$

where **A** is the species in question, **B** is the lattice site, and **C** is the charge relative to a reference state.

A can be any element, a vacancy (denoted v or V) or an electron (e).

B can be any element in the defect-free phase, or interstitial (i)

C can be either / (negative charge), · (positive charge), or × (no charge)

Example: Cr^{3+} and Nb^{5+} replace two Ti^{4+} in TiO_2:

$$2Ti_{Ti}^{\times} \rightarrow Cr_{Ti}^{/} + Nb_{Ti}^{\cdot}$$

Another example: Cr^{3+} and H^{+} replace Ti^{4+} in TiO_2 through formation of OH^{-} (hydrogen technically occupies an interstitial site):

$$Ti_{Ti}^{\times} \rightarrow Cr_{Ti}^{/} + H_i^{\cdot}$$

Chapter 1

INTRODUCTION

1.1 Nominally Anhydrous Minerals: the importance of hydrogen

Water is a centrally important component of the earth. This is true not just for earth's surface, where the importance of water in the atmosphere, oceans, and biosphere is obvious, but also its interior. For example, water is likely a key component to subduction, which helps to facilitate plate tectonics[1]. Subduction also drives water into earth's interior, where it becomes incorporated into mantle minerals as structural hydrogen (OH^- groups), affecting several mantle processes[2]. However, for how important this hydrogen is to earth's planetary scale processes, there are fundamental gaps in the narrative of hydrogen's fate in earth's interior. Notably, an active area of discussion has been how much hydrogen the mantle (and the earth overall) actually contains, and where that hydrogen is distributed[3–5]. Foundational to this conversation is an understanding of what minerals can take up structural hydrogen, how much hydrogen they can incorporate, and the atomic-level processes that facilitate this incorporation. This thesis focuses on these smaller-scale components to the larger story of hydrogen in the earth.

Hydrogen incorporation in rock-forming minerals has a subject of study for over 60 years. Early studies discovered structural hydrogen contained in quartz in the form of OH^- and H_2O[6], followed by studies on beryl[7]. These minerals, which do not contain stochiometric hydrogen, but could still incorporate small amounts of hydrogen, were eventually dubbed nominally anhydrous minerals (NAMs). However, it wasn't until later that the potential importance of NAMs in the Earth was made fully clear. Bell and Rossman (1992) demonstrated that major mantle phases like olivine, garnet, and pyroxene derived from the mantle contained hydrogen in concentrations ranging from 1 to 1000 μg/g, depending on the phase[3]. Although the individual concentrations of OH^- in these minerals are relatively small, over the large volume of earth's interior, this could amount to a significant quantity. Thus, more credence was given to the previously suggested idea that NAMs could sequester hydrogen in earth's mantle as OH^-, in amounts potentially

approaching earth's oceans. Subsequent discoveries, such as the high water content of a natural specimen of ringwoodite (the most abundant phase in the lower transition zone), supported the possibility that the mantle may have a carrying capacity of many oceans worth of water, and probably contains extremely hydrogen-rich regions[5]. The geophysical consequences of OH^- incorporation have also become a target of active study. Hydroxyl incorporation in quartz was found to facilitate deformation[8], and similar effects have been observed in olivine[9] (although the magnitudes of these effects can vary significantly[10]). Additionally, surveys of other major mantle phases find that hydrogen impacts their equations of state[2]. Importantly, these material properties can change significantly with only small amounts of hydrogen incorporation, meaning that hydrogen potentially has an outsized influence on earth's interior.

1.2 The challenges of measuring hydrogen

In the conversation on NAMs, it is important to recognize that in most cases, experimentally constraining the position of H^+ in a crystal structure presents a significant technical challenge. This comes down to three fundamental factors: **(1)** H^+ has an extremely low associated electron density compared to other species, **(2)** In many phases, H^+ is present in relatively low concentrations (non-stochiometric), and **(3)** In NAMs, H^+ almost universally occupies interstitial sites, of which there are very many, especially when compared to lattice points. In many instances, X-ray diffraction would be an ideal method for determining the positions or occupancies of a dopant species, but points **(1)** and **(2)** rule out this possibility. The extremely low electron density of H means that very few X-rays will scatter from an incorporated H^+ ion, a factor that can be compounded by low concentrations of H. Neutron scattering, on the other hand, is generally well-suited for observing structural H. However, it should be mentioned that neutron scattering is limited in its ability to detect hydrogen some situations, especially when samples are extremely small in size, cannot be quenched to ambient conditions, or in cases where hydrogen concentrations are too low.

The three factors listed above also result in significant barriers for determining the concentration of H^+ in a given sample. The low electron density (i.e., total lack of multiple valence electrons) of H^+ means that normally reliable techniques that depend on characteristic X-ray emission, like X-ray fluorescence (XRF) or electron probe microanalysis (EPMA), cannot directly detect H at all. Additionally, relying on low oxide totals (a typical indicator of structural H for these methods) is not a viable method for determining H contents, especially at the concentrations typical for NAMs. At low concentrations of OH^-, methods that would otherwise be reliable for quantifying large H_2O concentrations, like thermogravimetric analysis (TGA), are foiled by surface OH^-/H_2O contamination and small sample volumes. For mass spectrometry-based techniques, like secondary ion mass spectrometry (SIMS), hydrogen can be measured with great precision, but externally calibrated, matrix-specific standards are needed to accurately match these values to absolute concentrations. Although the question of where hydrogen goes in minerals is inherently linked to the question of how much hydrogen those same minerals contain, concentration measurements are in many ways a separate challenge unto themselves. The author has spent significant time developing these and other analytical methods for measuring hydrogen concentrations, but this thesis deals primarily with determining the structures of hydrogen-based defects.

Despite the challenges associated with the direct observation of structural hydrogen, there are other analytical methods that can convey this information, albeit indirectly. Methods of vibrational spectroscopy like Raman spectroscopy, and especially Fourier transform infrared (FTIR) spectroscopy produce spectra whose features are inherently linked to atomic structure. Transmission FTIR in particular has demonstrated an extremely high sensitivity to structurally incorporated OH^- and is a central focus of the work described in the following chapters. The utility of FTIR in studying structural OH^- boils down to the fundamental factors that: the O-H bond forms a strong dipole (and thus strong infrared absorptions), and that these absorptions occur in a spectral range that is generally free from other features. This means that the presence of OH^- is typically unambiguous; OH^- modes are usually present as prominent features in an otherwise featureless spectral region. Typically, O-H stretching modes occur in the range of 3600 to 3000 cm^{-1}, shifted down in energy from the asymmetric stretching of free water modes.

These shifts occur due to hydrogen bonding. When an OH^- group is confined to a fixed field of surrounding O^{2-} ions, it forms a hydrogen bond. Stronger hydrogen bonds shift the O-H stretching mode to lower energy positions, and stronger bonds are a consequence of shorter hydrogen bonding distances. This link between hydrogen bond length (typically measured as an oxygen-oxygen distance) and vibrational frequency is predictable, and the relation has been experimentally derived[11]. Because unique OH^- defects should have unique associated hydrogen bonding distances, this means that individual O-H stretching modes should each correspond to a structurally unique defect state. By coupling this with other information, such as a mode's polarization dependence, one could begin to work out the possible positions for H in a crystal lattice. Another technique that produces a similar type of information is solid state ^1H nuclear magnetic resonance (NMR), where an equivalent hydrogen bonding distance relation has been derived[12]. Although NMR has its own limitations, such as an incompatibility with Fe-bearing phases and a lower sensitivity than FTIR, it can still serve a unique role in studying NAMs and is utilized in later chapters.

1.3 The most versatile dopant

As a structural component in minerals, the flexibility displayed by hydrogen is virtually unmatched. There are numerous mechanisms through which hydrogen may be incorporated into NAMs, but all these mechanisms can be considered through the lens of defect chemistry. As a dopant species, hydrogen itself can be conceptualized as a form of point defect. To accommodate hydrogen defects, a crystal structure must contain other defects states that enable hydrogen incorporation (this is almost always done through charge balance between the hydrogen and other defect state). Put another way, the non-hydrogen-based defect chemistry of minerals facilitates hydrogen incorporation. Thus, the possible methods for hydrogen incorporation in NAMs are a function of the many possible defect chemistries. Here, I summarize the commonly encountered methods of hydrogen incorporation, defined with respect to the coupled non-hydrogen defect.

1.3.1 OH^- as a halogen-like species

A straightforward method of OH^- incorporation is the occupation of a halogen site by OH. Protonation effectively renders the O^{2-} ion a monovalent, anionic species with a crystal radius similar to halogen anions, making this exchange favorable (especially with F^-). In many cases, there is a full solid solution series between a hydroxide and halogen end member, and the two are stochiometric, meaning the phase is not truly "nominally anhydrous". The apatite group ($Ca_5(PO_4)_3(OH,F,Cl)$) and topaz ($Al_2(SiO_4)(F,OH)_2$) are good examples of this. However, there are also instances where a full solid solution series between end-member halogen and OH^- species does not exist, and these cases could fall under the banner of NAMs. For example, sodalite ($Na_4(Si_3Al_3)O_{12}Cl$) may incorporate some OH^- in place of Cl^-, but OH^- concentrations don't typically become stochiometric and there is no natural pure OH^- endmember of the sodalite group. Nevertheless, in the earth's interior, stochiometric halogen-bearing minerals are not common, so this substitution mechanism will not be considered much from this point on.

1.3.2 The coupled substitution

When no halogen site is available, H^+ must occupy an interstitial site and bond to oxygen to be incorporated. Protonating an existing O^{2-} to form OH^- results in a net positive charge that must be accommodated by some other defect in a crystal structure. A coupled substitution or "co-doping" defect is one way to accomplish this. This type of mechanism proceeds through a substitution of a native cation with a lower valence cation. The cation substitution results in a net negative charge which is compensated by the net positive charge of H^+. One well-known example of this occurs in stishovite (SiO_2), where OH^- formation is facilitated by the substitution of Al^{3+} for Si^{4+} [13,14]:

$$Si_{Si}^{\times} + O_O^{\times} \rightarrow Al_{Si}^{/} + OH_i^{\cdot}$$

In the stishovite system, Fe incorporation is also a viable pathway for OH^- incorporation[14]. These types of substitutions are also well-documented in rutile (TiO_2), where OH^- is found to couple to substitutions for Ti^{4+} by Al^{3+}, Cr^{3+}, Fe^{3+}, and Mn^{3+} [15–18]. These types of defects

are what make rutile among the most hydrous of the naturally observed mantle NAMs, capable of incorporating up to 0.8 wt% H_2O[16]. Minerals with more flexible chemistries that can incorporate large quantities of lower valence cations are good potential targets for studying coupled substitution mechanisms. Compared to some other types of hydrogen defects, coupled substitutions are potentially more straightforward to identify. For example, the relative intensities of particular OH^- modes can be tied to corresponding changes in chemistry that are measurable via methods like EPMA.

1.3.3 Cation reduction

In phases with reducible cations, OH^- incorporation may also proceed via the reduction of a native cation, rather than the substitution of a lower valence species. This has mainly been documented in the TiO_2 system, specifically with rutile[19]. The charge balance can be described as follows:

$$Ti_{Ti}^{\times} + O_O^{\times} \rightarrow Ti_{Ti}^{/} + OH_i^{\cdot}$$

wherein every incorporated interstitial H^+ is charge compensated by a Ti^{3+} center. It is for this reason that the incorporation of hydrogen into rutile is predicted to have a dependence on fO_2. Notably, the incorporation of H^+ through this pathway will necessarily compete with other positively charged defects to balance Ti^{3+} centers under reduced conditions. In the case of rutile, oxygen vacancies (v_O), which can be formed very easily, are the typical coexisting defect[20,21]. In theory, any other positively charged defect could fill this role, for example, substitution of one Ti^{4+} for Nb^{5+}. Thus, OH^- incorporation via cation reduction is potentially sensitive to many factors beyond just fO_2. Because the reduced cation pathway for OH^- incorporation does not result in a measurable change in overall composition, this pathway usually requires different methods for detection compared to coupled substitution mechanisms, like visible light spectroscopy. This type of defect is investigated in Chapters 3 and 4.

1.3.4 Cation vacancies - the hydrogarnet-type defect

This class of defects borrows its name from the most well-known minerals in which it occurs: the calcium (usually grossular) garnets. Garnets are found to incorporate OH^- groups through a cation vacancy mechanism, in which a Si vacancy (v_{Si}) is charge compensated by the incorporation of four OH^- groups[22]:

$$Si_{Si}^{\times} + 4O_O^{\times} \rightarrow V_{Si}^{////} + 4OH_i^{\cdot}$$

The vacant tetrahedral Si site is essentially propped up by the four OH^- groups, which are formed by protonating the four oxygens of the silica site. Within grossular garnets, this substitution is extremely favorable to the point that all Si atoms may be replaced in this manner, forming the fully hydrated garnet endmember katoite. Colloquially, substitutions of OH^- for Si tend to be described as "hydrogarnet" or "hydrogarnet-type" defects, even in other silicate systems[23]. This is true even for higher pressure phases with octahedrally coordinated Si, like stishovite[24–26] or davemaoite . Additionally, this class of defects can be expanded to include to all cation vacancy-OH substitutions. For example, Mg^{2+} vacancies are thought to be one potential mechanism of OH^- incorporation in olivine[27]. The compositional simplicity of this defect type (hydrogen only needs to couple to a native defect), along with its demonstrated prevalence in garnets and likely high concentrations in ringwoodite[5], makes it an attractive and common choice for modeling hydrogen solubility in deep earth phases. Chapter 2 deals with an example of this defect type.

1.4 Hydride: the other hydrogen ion

Based on the conventional understanding of hydrogen's behavior in oxide materials, it would appear safe to assume that the H^+ ion is the only major hydrogen species that should be considered in NAMs. Considering a typical silicate or oxide structure as essentially a field of oxide ions coordinated to cations, it is reasonable to conclude that a hydrogen atom introduced to this structure would oxidize, bond to O^{2-}, and form OH^-. However, an increasing number of oxide phases have been demonstrated to incorporate an alternate form of hydrogen that is rarely considered: hydride (H^-). When this highly

reduced form of hydrogen is incorporated into an oxide phase, the process occurs through a direct substitution of O^{2-} for H^-. The typical radius of H^- is quite comparable to O^{2-}, making the substitution structurally feasible. Almost as a parallel to OH^- incorporation, the net positive charge difference between these ions is then balanced elsewhere through complimentary negatively charged defects (discussed in more detail below). If the concentration of H^- is high enough to be considered stoichiometric (which is frequently the case), then these materials may be referred to as oxyhydrides.

Currently, hydride is virtually absent from the conversation surrounding NAMs. This is probably in no small part due to how unusual this form of hydrogen is; most earth scientists would probably assume hydride is unstable in oxide-based minerals. However, this could present a major oversight in the study of deep earth hydrogen. In materials science literature, hydride has an unexpectedly high solubility in the material class most relevant to the deep earth: perovskites. In titanium and other transition metal perovskites, hydride can be exchanged with oxide in concentrations ranging from trace to stochiometric levels[28].

Compared to studies of hydroxide, the study of hydride in oxide materials is a relatively untapped subject, even in the fields of materials science, inorganic chemistry and solid-state physics. Although hydride had been successfully introduced in crystalline oxides at least as early as 1981[29], much of the progress in studying these materials has come in the last decade or so. A few dozen conclusive examples of hydride incorporation have emerged in that time, and research has been expanding to new classes of materials[30,31]. Although the current list of these materials is still relatively limited, there are a few commonalities that seem to be typical for oxyhydrides. First is that oxyhydrides are most typically comprised of electropositive cations, typically the alkali metals and alkaline earth metals, and less commonly, rare earth elements[32]. Slightly less electropositive metals like Sc and Ti are also common components of oxyhydrides[33]. Additionally, other cation species like Si, and P may also be constituents in oxyhydrides, although it appears that highly electropositive elements must also be present to stabilize H^- [34,35]. Structurally, there is no known limitation on hydride incorporation, but perovskites seem to have a predilection for hydride incorporation. Other material structures that demonstrate hydride

solubility to varying degrees are apatite ($Ca_5(PO_4)_3OH$) , rock-salt (MgO), and wurtzite (ZnO), among others[36–38].

1.5 Mechanisms of hydride incorporation

Although there are relatively few examples hydride incorporation into oxides when compared to hydroxide, multiple mechanisms can be identified from the literature, hinting at a broad landscape of potential compatible defect chemistries. In the same vein as OH^- incorporation mechanisms, H^- incorporation mechanisms typically involve a complimentary defect state that serves as a relatively negative charge to balance the relatively positive charge of substituted H^-. As alluded to previously, many of these defect categories are essentially equivalents to categories of OH^- defects.

1.5.1 Reduced cation valence

Much like in systems with OH^- defects, H^- can be accommodated via a cation reduction mechanism. Prime examples of this incorporation mechanism can be found among transition metal perovskites, particularly the titanate perovskites. H^- is found to incorporate in the entire $(Ca,Sr,Ba)TiO_3$ perovskite series through reactions with hydride salts (particularly CaH_2)[28,39,40]. Once H^- is incorporated, Ti^{4+} is reduced to Ti^{3+} to compensate for H^-. By simple charge balance, this substitution should be limited by the available Ti^{4+} that can be reduced to Ti^{3+}:

$$Ti_{Ti}^{\times} + O_O^{\times} \rightarrow Ti_{Ti}^{/} + H_O^{\cdot}$$

In practice, H^- can replace about 20% of all O^{2-}, representing an unusually high hydride solubility[39]. It is feasible that other cations with variable oxidation states could participate in similar coupled defects, although they likely have to resist complete reduction enough to avoid decomposing into metal hydrides. Examples of this defect type are investigated in Chapters 3, 4, and 5.

1.5.2 Coupled substitutions

Again, this mechanism draws strong parallels to OH^- defects. In this case, H^- substitutes for O^{2-}, while a lower valence cation simultaneously substitutes for a native cation. The difference in charge between the native and substituted cation can apparently vary, as studies on $SrTiO_3$ have demonstrated a Sc^{3+}-Ti^{4+} substitution[33]:

$$Ti_{Ti}^{\times} + O_O^{\times} \rightarrow Sc_{Ti}^{/} + H_O^{\cdot}$$

And studies of $BaTiO_3$ document a Na^+-Ti^{4+} substitution[41]:

$$Ti_{Ti}^{\times} + O_O^{\times} \rightarrow Na_{Ti}^{///} + 3H_O^{\cdot}$$

The same substitution was successfully carried out for V- and Cr-based perovskites, too. Note that in both cases, the substituting cation is one that meets the general criteria for stabilizing H^-; Na^+ is highly electropositive with a fixed valence, and Sc^{3+} is in the first column of the d-block. However, this may not be strictly necessary. For example, both Al-substituted and Fe-substituted $SrTiO_3$ have been studied with respect to hydride incorporation, although the presence of hydride in these materials was not as conclusive, and the concentrations were likely not high[42,43]. Overall, there is a strong implication that a wide range of coupled substitution mechanisms could greatly increase hydride solubility in, at the very least, perovskites. Co-doping with lower valence cations often results in stochiometric hydride concentrations that far exceed the maximum concentrations attained through just cation reduction[41]. Coupled substitutions are explored in Chapter 6.

1.5.3 Interstitial coupled species

Yet another distinct mechanism of hydride incorporation was observed by Jollands and Balan (2022) in Be-doped corundum crystals[44]. The mechanism proposed by these authors was one in which H^- bonds directly to Be^{2+}, and the resulting Be-H group occupies an interstitial site in the vicinity of an Al^{3+} vacancy. Although this mechanism does involve a coupled substitution of sorts between Be and H, it differs from the coupled substitutions outlined above in two critical ways. First, neither the Be nor the H directly or nearly directly

occupy either Al^{3+} or O^{2-} sites. Be only coordinates to three of the six O atoms surrounding the Al vacancy, and H coordinates only to Be. Second, the coordination of H^- differs significantly from other cases of hydride incorporation. In most other instances, hydride will bond to multiple or many cations, much like the oxygen it is directly replacing. In this mechanism, H's single bond results in a dangling Be-H bond, almost akin to the hydride-equivalent of an OH^- group. Jollands and Balan present this defect mechanism as carrying a net charge, rather than being fully neutral like the other mechanisms described above. A possible remedy to this could be a coupling to an additional defect in the form of an oxygen vacancy:

$$Al_{Al}^{X} + O_{O}^{X} \rightarrow V_{Al}^{///} + v_{O}^{\cdot\cdot} + Be_{i}^{\cdot\cdot} + H_{i}^{/}$$

wherein H_i refers to the H^- ion, rather than the more typical designation of H^+. With the addition of the oxygen vacancy, the difference between this mechanism and true coupled substitutions comes down to site occupancies; because neither the cation nor the anion site is directly occupied, there are effectively four coexisting defect states.

1.5.4 Hydride acting as a halogen

Within oxides, the hydride ion is generally found to have a radius similar to not just O^{2-}, but also F^-. Given the charge and radius compatibility with F^-, it is natural to speculate that H^- may be capable of directly substituting for F^- in typical halogen-containing phases. Especially intriguing is the possibility of mixed-valence hydrogen systems; OH^- is also exchangeable with halogens in many phases. This exact defect type has been successfully induced in two synthetic systems to date: apatite[36] and mayenite[45]. In both cases, it is possible to completely occupy $OH^-/F^-/Cl^-$ sites entirely with H^-, resulting in stoichiometric oxyhydride phases. However, only the direct exchange of OH^- and H^- has been demonstrated. Direct exchange with halogens is only implied as feasible because H^- can occupy sites that OH^- occupies, which are also sites that F^- or Cl^- can occupy.

1.5.5 F-centers

In oxygen-deficient, binary group II oxides, H^- has successfully been substituted in place of O^{2-}. Such defects have been achieved in analytically pure crystals of MgO, CaO, and SrO[29]. The inflexible valence of the group II elements means that charge balance for H^- cannot generally be accounted for via cation reduction, and a lack of other dopants means that coupled substitutions with monovalent cations are also unavailable. Thus, to maintain a charge balance, the formation of F-centers (i.e. trapped electrons) has been proposed[37]. Such H^- defects seem to have a low limit for incorporation, so they will not be considered much in this work.

1.6 Detection of hydride

Other than its relative obscurity in comparison to hydroxide, there is another significant reason that hydride has probably not been considered much in the study of NAMs. Although hydride may be detected through essentially the same techniques as hydroxide, this detection carries significant caveats. First, consider FTIR, historically the most important method for hydrogen detection and speciation analysis in NAMs. As was discussed previously, OH^- is unambiguously identified by FTIR in the vast majority of cases, because O-H stretching modes overlap with virtually no other infrared features. This predictability comes down to the relatively limited structural possibilities for the OH^- group: H^+ forms a single bond to just O^{2-}, and the majority of the variation in the vibrational frequency can be attributed to hydrogen bonding to the surrounding O atoms. The O-H bond is always strongly IR active and can be identified even in low concentrations. This isn't to say that studies of OH^- groups are simple (they are not), but rather that the structural parameter space that the H^+ ion operates in has well-defined and extensively studied limits.

In contrast, H^- is far more unpredictable and far less intuitive to deal with. Recall how the infrared spectrum of OH^- is a direct consequence of local structure. This is also true for hydride, which is what makes the spectroscopy of hydride difficult. H^- can bond to essentially any cation species and seems capable of bonding to many cations at once (the limitations to this are not known). Once in the O^{2-} site, H^- could possibly bond

asymmetrically to the surrounding cations, maybe even forming multiple coexisting structural states. The result of these variations in bonding species and bonding geometries is an unpredictable range of H^- vibrational modes with unknown IR activities. Added to this is that H^- modes tend to occur below 1500 cm^{-1}, a region typically populated with highly absorbing native modes that is overlooked in many studies of NAMs. These native modes are usually themselves unassigned to a particular vibration, which makes distinguishing them from H^- modes potentially difficult. In summary, there is currently no "intuitive" way to assign a mode to H^- in an infrared spectrum, and even if hydride is present, it will probably be difficult to identify. Nonetheless, examples of H^- vibrational modes have been identified in oxides via FTIR or other methods. A handful of examples have been published for materials including MgO, ZnO, Sr-hydroxyapatite, $BaTiO_3$, and corundum. Several of these are presented in Figure 1.1.

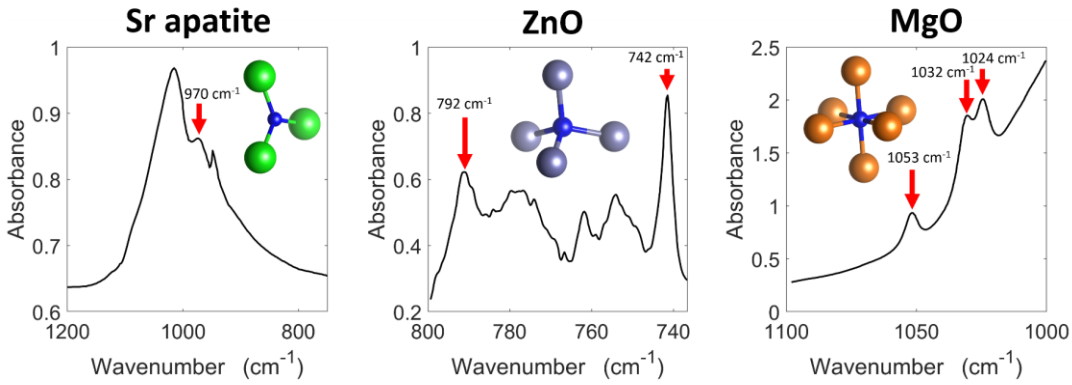

Figure 1.1 *Spectra showing hydride modes (red arrows) in three materials: Sr-hydride-apatite[34], ZnO[38] and MgO[37]. The bonding environment for hydride (blue sphere) is pictured in each plot. From left to right: trigonal planar coordination with Sr, tetrahedral coordination with Zn, octahedral coordination with Mg. Absorbance values are arbitrary*

By far the most instrumental technique for recent advances in oxyhydride studies has been solid state ^1H NMR. Partially a consequence of its highly varied bonding environments, the ^1H NMR behavior of hydride can diverge widely in different materials. When hydride is bonded strictly to cations without valence electrons (i.e., group I and II cations), its associated features occupy a low positive shift region, overlapping with the positions of OH^- features[32]. However, this can change significantly when hydride bonds to transition metal species. In the (Ca,Sr,Ba)TiO_3 family of perovskites, hydride features

occur in a negatively shifted position, have a much broader line shape, and become more negatively shifted with increased H^- concentrations. These negative shifts ("Knight shifts") indicate that electrons associated with the H-Ti bonds are delocalized (i.e. in the conduction band). As more electrons are added to the conduction band, the degree of this negative shift increases (this means that oxygen vacancies can also contribute to this shift in titanates as well)[46,47]. Therefore, while hydride can occasionally be mistaken for hydroxide via ^1H NMR, cases where features experience a Knight shift unambiguously indicate the presence of structural hydride. This has made ^1H NMR an essential component of the literature on oxyhydrides thus far. However, even ^1H NMR has limitations.

Despite the difficulties associated with FTIR detection of H^-, and its relative underdevelopment for this application, FTIR may prove to be an essential component to future studies of hydride in the deep earth. Consider some of the alternate techniques used to identify H^- in oxides: ^1H NMR, neutron scattering and TGA. These techniques generally either require substantial sample material (at least 20 mg or more) or cannot be performed on samples *in-situ* (both in the context of natural samples and high-pressure experiments). This means that these techniques are generally unsuitable for analyses of small inclusions in diamonds, *in-situ* analyses during diamond anvil experiments, and analyses of small grains in natural materials. By contrast, FTIR can operate in all of these analysis conditions, which are the ones most relevant to studies of the deep earth. Thus, although the currently used analyses are good choices for learning more about the structure and chemistry of H^- in oxides, further development of FTIR will be necessary for more mantle-relevant studies of H^-.

1.7 The role of theory for studying NAMs

Computational techniques (e.g., density functional theory, or DFT) are becoming increasingly instrumental to studies of NAMs, including the interpretation of infrared spectra. As mentioned previously, individual OH^- and H^- stretching modes are indicative of unique structural states. Therefore, infrared spectra directly record which defect states are present in a material and in what relative quantities, but only if these spectra can be

accurately interpreted. In the case of OH^-, basic structural information can be ascertained from a given spectrum (as was previously mentioned), except this is usually only enough to make an educated guess about the affiliated defect state. DFT can help to bridge the gap between these educated guesses and spectroscopic data to produce more accurate models of hydrogen's structural state. However, when dealing with these computational methods, it is important to understand their limitations.

Generally, the structures (i.e., atomic positions) produced by DFT methods are quite reliable, tending to match experimentally measured structures well. Predictions related to vibrational spectroscopy, on the other hand, can be quite variable, at least for the methods employed in periodic structures like NAMs. The behaviors of OH^- groups in particular have proven to be consistently difficult to accurately simulate, with errors associated with band positions commonly ranging from less than 10 cm^{-1} to 200 cm^{-1}, even when the identity of the affiliated OH structure is known (keep in mind, though, that this amounts to, at most, an error of a few percent when considering the energy of the associated vibration). In cases of materials with numerous, closely-spaced O-H modes, like olivine or garnet[22,48], this can hamper band assignments. The reasons for these errors are usually not immediately apparent. However, this does not mean that DFT cannot be effectively used for this application. Rather, the information that can be gleaned from calculations must not be treated in absolute terms. For example, one could understand that while absolute mode positions will probably be offset, DFT can simulate other diagnostic characteristics of a spectrum, like line shape, polarization behavior, or systematic shifts in relative band positions.

As mentioned in the prior section, FTIR identification of H^- is inherently more difficult than OH^-, mostly due to the unknown positions and characteristics of hydride modes. This presents an ideal use case for DFT. In the case of hydride, mode positions are unintuitive due to the high variabilities in bonding environments and bonded species, so mode position estimates that are off by even 100 cm^{-1} can still prove valuable. For example, because hydride modes are usually in very absorbing regions, DFT-predicted mode positions can be quite helpful in guiding decisions related to measurements, like how thin samples must be made to achieve appropriate transmission. Thus, in future studies of

hydride in oxides, DFT will probably play a key role. However, whether the accuracy of DFT applied to hydride is better or worse than that of OH^-, or if its accuracy is highly situation dependent (reliant on bonding species, for example) has not been rigorously tested. A systematic review would be desirable, but not enough test cases have been produced yet to make overall assessments.

1.8 Thesis outline

This thesis takes a joint computational-experimental approach to studying the crystal chemistry of hydrogen in rutile- and perovskite-structured materials, giving attention to both hydroxyl and hydride. This is discussed mostly through the lens of infrared spectroscopy, and particular focus is placed on assessing the utility of DFT in making predictions related to this analytical technique. The rutile and perovskite structures are singled out for study not just for their importance to the mantle, but also their unique abilities to incorporate hydrogen in numerous ways. Moving through the chapters, this work begins in the well-defined and conventional cases of hydrogen incorporation that will be familiar to earth scientists, before shifting towards the study of more unusual and foreign forms of hydrogen chemistry.

First, Chapter 2 begins with a computational study that seeks to clarify the arrangement of OH^- groups in an unusually hydrous form of stishovite. An emphasis is placed on deriving stable structural configurations of hydroxyl, and then simulating their infrared behaviors to test them against experimentally collected data.

Chapter 3 moves on to studying the interaction between oxygen vacancies and structurally incorporated hydrogen, also through DFT. Unexpectedly, hydride is found to be exceptionally stable, with potential consequences for "hidden" hydrogen in rutile. Predictions are then made about the spectroscopic behavior of the H^- ion. As a follow up to these calculations, Chapter 4 details an experimental study on H_2-annealed, synthetic rutile crystals. At the outset, the experiments are designed to look for the expected hydride-related modes via infrared spectroscopy and ^1H NMR. Ultimately, these measurements,

used in combination with EPR, document the competition between oxygen vacancies and hydrogen-based defects in rutile.

Chapter 5 centers entirely on hydride in $SrTiO_3$ perovskite, a structural analogue to davemaoite. The experiments in this chapter make use of a well-documented reaction using CaH_2 to introduce hydride into the $SrTiO_3$ structure. DFT is used to predict the infrared behavior of these hydride ions, then these infrared signatures are documented for the first time. In addition to the incorporated hydride, other interesting spectroscopic phenomena are recorded as well. After Chapter 5 documents the path from theory to experiment for analyzing hydride in $SrTiO_3$, Chapter 6 proposes new hydride- and hydroxide-based defects to be investigated in davemaoite. The unusually high alkali content of the type-specimen is put forward as a possible means for hydrogen incorporation in davemaoite, potentially making it a hydrogen carrier in the deep earth. DFT is used to predict what hydrogen- based structures might be stable in davemaoite, and a variety of techniques are used to try and anticipate what spectral signatures a hydroxyl- or hydride-containing davemaoite sample might have.

References

(1) Stern, R. J. The Evolution of Plate Tectonics. *Phil. Trans. R. Soc. A.* **2018**, *376* (2132), 20170406. https://doi.org/10.1098/rsta.2017.0406.

(2) Jacobsen, S. D. Effect of Water on the Equation of State of Nominally Anhydrous Minerals. *Reviews in Mineralogy and Geochemistry* **2006**, *62* (1), 321–342. https://doi.org/10.2138/rmg.2006.62.14.

(3) Bell, D. R.; Rossman, G. R. Water in Earth's Mantle: The Role of Nominally Anhydrous Minerals. *Science* **1992**, *255* (5050), 1391–1397. https://doi.org/10.1126/science.255.5050.1391.

(4) Bolfan-Casanova, N. Water in the Earth's Mantle. *Mineral. mag.* **2005**, *69* (3), 229–257. https://doi.org/10.1180/0026461056930248.

(5) Pearson, D. G.; Brenker, F. E.; Nestola, F.; McNeill, J.; Nasdala, L.; Hutchison, M. T.; Matveev, S.; Mather, K.; Silversmit, G.; Schmitz, S.; Vekemans, B.; Vincze, L. Hydrous Mantle Transition Zone Indicated by Ringwoodite Included within Diamond. *Nature* **2014**, *507* (7491), 221–224. https://doi.org/10.1038/nature13080.

(6) Wood, D. L. Infrared Absorption of Defects in Quartz∗. *Journal of Physics and Chemistry of Solids* **1960**, *13* (3–4), 326–336. https://doi.org/10.1016/0022-3697(60)90017-2.
(7) Wood, D. L.; Nassau, K. The Characterization of Beryl and Emerald by Visible and Infrared Absorption Spectroscopy, 1968.
(8) Griggs, D. Hydrolytic Weakening of Quartz and Other Silicates*. *Geophysical Journal of the Royal Astronomical Society* **1967**, *14* (1–4), 19–31. https://doi.org/10.1111/j.1365-246X.1967.tb06218.x.
(9) Tielke, J. A.; Zimmerman, M. E.; Kohlstedt, D. L. Hydrolytic Weakening in Olivine Single Crystals: Hydrolytic Weakening in Olivine. *J. Geophys. Res. Solid Earth* **2017**, *122* (5), 3465–3479. https://doi.org/10.1002/2017JB014004.
(10) Kumamoto, K. M.; Hansen, L. N.; Breithaupt, T.; Wallis, D.; Li, B.; Armstrong, D. E. J.; Goldsby, D. L.; Li, Y. (Will); Warren, J. M.; Wilkinson, A. J. The Effect of Intracrystalline Water on the Mechanical Properties of Olivine at Room Temperature. *Geophysical Research Letters* **2024**, *51* (4), e2023GL106325. https://doi.org/10.1029/2023GL106325.
(11) Libowitzky, E. Correlation of O-H Stretching Frequencies and O-H···O Hydrogen Bond Lengths in Minerals. *Chemical Monthly* **1999**, *130*, 1047–1059.
(12) Eckert, H.; Yesinowski, J. P.; Silver, L. A.; Stolper, E. M. Water in Silicate Glasses: Quantitation and Structural Studies by Proton Solid Echo and Magic Angle Spinning NMR Methods. *J. Phys. Chem.* **1988**, *92* (7), 2055–2064. https://doi.org/10.1021/j100318a070.
(13) Pawley, A. R.; McMillan, P. F.; Holloway, J. R. Hydrogen in Stishovite, with Implications for Mantle Water Content. *Science* **1993**, *261* (5124), 1024–1026. https://doi.org/10.1126/science.261.5124.1024.
(14) Litasov, K. D.; Kagi, H.; Shatskiy, A.; Ohtani, E.; Lakshtanov, D. L.; Bass, J. D.; Ito, E. High Hydrogen Solubility in Al-Rich Stishovite and Water Transport in the Lower Mantle. *Earth and Planetary Science Letters* **2007**, *262* (3–4), 620–634. https://doi.org/10.1016/j.epsl.2007.08.015.
(15) Swope, R. J.; Smyth, J. R.; Larson, A. C. H in Rutile-Type Compounds: I. Single-Crystal Neutron and X-Ray Diffraction Study of H in Rutile. *American Mineralogist* **1995**, *80* (5–6), 448–453. https://doi.org/10.2138/am-1995-5-604.
(16) Vlassopoulos, D.; Rossman, G. R.; Haggerty, S. Coupled Substitution of H and Minor Elements in Rutile and the Implications of High OH Contents in Nb- and Cr-Rich Rutile from the Upper Mantle. *American Mineralogist* **1993**, *78* (11–12), 1181–1191.
(17) Bromiley, G. Solubility of Hydrogen and Ferric Iron in Rutile and TiO_2 (II): Implications for Phase Assemblages during Ultrahigh-Pressure Metamorphism and for the Stability of Silica Polymorphs in the Lower Mantle. *Geophys. Res. Lett.* **2004**, *31* (4), L04610. https://doi.org/10.1029/2004GL019430.
(18) Wang, S.; Su, Y.; Wang, Q.; Smyth, J. R.; Liu, D.; Zhu, X.; Miao, Y.; Hu, Y.; Ye, Y. Crystal Structure, Vibrational Spectra on Trivalent-Cation-Doped Rutile and Application in Optical Materials. *J. Phys. Chem. C* **2023**, *127* (25), 12160–12170. https://doi.org/10.1021/acs.jpcc.3c00400.
(19) Colasanti, C. V.; Johnson, E. A.; Manning, C. E. An Experimental Study of OH Solubility in Rutile at 500-900 C, 0.5-2 GPa, and a Range of Oxygen Fugacities.

American Mineralogist **2011**, *96* (8–9), 1291–1299. https://doi.org/10.2138/am.2011.3708.

(20) Palfey, W. R.; Rossman, G. R.; Goddard, W. A. Structure, Energetics, and Spectra for the Oxygen Vacancy in Rutile: Prominence of the Ti–H_O–Ti Bond. *J. Phys. Chem. Lett.* **2021**, *12* (41), 10175–10181. https://doi.org/10.1021/acs.jpclett.1c02850.

(21) Norby, T.; Widerøe, M.; Glöckner, R.; Larring, Y. Department of Chemistry, University of Oslo, Centre for Materials Science and Nanotechnology (SMN), Gaustadalléen 21, NO-0349 Oslo, Norway. *Dalton Trans.* **2004**, 7.

(22) Geiger, C. A.; Rossman, G. R. IR Spectroscopy and OH– in Silicate Garnet: The Long Quest to Document the Hydrogarnet Substitution. *American Mineralogist* **2018**, *103* (3), 384–393. https://doi.org/10.2138/am-2018-6160CCBY.

(23) Panero, W. R. First Principles Determination of the Structure and Elasticity of Hydrous Ringwoodite. *J. Geophys. Res.* **2010**, *115* (B3), 2008JB006282. https://doi.org/10.1029/2008JB006282.

(24) Spektor, K.; Nylen, J.; Stoyanov, E.; Navrotsky, A.; Hervig, R. L.; Leinenweber, K.; Holland, G. P.; Haussermann, U. Ultrahydrous Stishovite from High-Pressure Hydrothermal Treatment of SiO_2. *Proceedings of the National Academy of Sciences* **2011**, *108* (52), 20918–20922. https://doi.org/10.1073/pnas.1117152108.

(25) Spektor, K.; Nylen, J.; Mathew, R.; Edén, M.; Stoyanov, E.; Navrotsky, A.; Leinenweber, K.; Häussermann, U. Formation of Hydrous Stishovite from Coesite in High-Pressure Hydrothermal Environments. *American Mineralogist* **2016**, *101* (11), 2514–2524. https://doi.org/10.2138/am-2016-5609.

(26) Palfey, W. R.; Rossman, G. R.; Goddard III, W. A. Behavior of Hydrogarnet-Type Defects in Hydrous Stishovite at Various Temperatures and Pressures. *Journal of Geophysical Research: Solid Earth* **2023**, *128*. https://doi.org/10.1029/2022JB024980.

(27) Tollan, P. M. E.; Smith, R.; O'Neill, H. St. C.; Hermann, J. The Responses of the Four Main Substitution Mechanisms of H in Olivine to H_2O Activity at 1050 °C and 3 GPa. *Prog. in Earth and Planet. Sci.* **2017**, *4* (1), 14. https://doi.org/10.1186/s40645-017-0128-7.

(28) Sakaguchi, T.; Kobayashi, Y.; Yajima, T.; Ohkura, M.; Tassel, C.; Takeiri, F.; Mitsuoka, S.; Ohkubo, H.; Yamamoto, T.; Kim, J. eun; Tsuji, N.; Fujihara, A.; Matsushita, Y.; Hester, J.; Avdeev, M.; Ohoyama, K.; Kageyama, H. Oxyhydrides of (Ca,Sr,Ba)TiO_3 Perovskite Solid Solutions. *Inorg. Chem.* **2012**, *51* (21), 11371–11376. https://doi.org/10.1021/ic300859n.

(29) González, R.; Chen, Y.; Mostoller, M. Substitutional H − -Ion Vibrations in the Alkaline-Earth Oxides Reduced at High Temperatures. *Phys. Rev. B* **1981**, *24* (12), 6862–6869. https://doi.org/10.1103/PhysRevB.24.6862.

(30) Mutschke, A.; Bernard, G. M.; Bertmer, M.; Karttunen, A. J.; Ritter, C.; Michaelis, V. K.; Kunkel, N. Na_3SO_4H—The First Representative of the Material Class of Sulfate Hydrides. *Angew Chem Int Ed* **2021**, *60* (11), 5683–5687. https://doi.org/10.1002/anie.202016582.

(31) Mutschke, A.; Schulz, A.; Bertmer, M.; Ritter, C.; Karttunen, A. J.; Kieslich, G.; Kunkel, N. Expanding the Hydride Chemistry: Antiperovskites A_3MO_4H (A = Rb, Cs; M = Mo, W) Introducing the Transition Oxometalate Hydrides. *Chem. Sci.* **2022**, *13* (26), 7773–7779. https://doi.org/10.1039/D2SC01861F.

(32) Hayashi, K.; Sushko, P. V.; Hashimoto, Y.; Shluger, A. L.; Hosono, H. Hydride Ions in Oxide Hosts Hidden by Hydroxide Ions. *Nat Commun* **2014**, *5* (1), 3515. https://doi.org/10.1038/ncomms4515.

(33) Takeiri, F.; Aidzu, K.; Yajima, T.; Matsui, T.; Yamamoto, T.; Kobayashi, Y.; Hester, J.; Kageyama, H. Promoted Hydride/Oxide Exchange in $SrTiO_3$ by Introduction of Anion Vacancy via Aliovalent Cation Substitution. *Inorg. Chem.* **2017**, *56* (21), 13035–13040. https://doi.org/10.1021/acs.inorgchem.7b01845.

(34) Alexander Mutschke; Thomas Wylezich; Clemens Ritter; Antti J. Karttunen; Nathalie Kunkel. An Unprecedented Fully H- -Substituted Phosphate Hydride $Sr_5(PO_4)_3H$ Expanding the Apatite Family. *European Journal of Inorganic Chemistry* **2019**, *48*, 5073–5076. https://doi.org/10.1002/ejic.201901151.

(35) Gehlhaar, F.; Finger, R.; Zapp, N.; Bertmer, M.; Kohlmann, H. $LiSr_2SiO_4H$, an Air-Stable Hydride as Host for Eu(II) Luminescence. *Inorg. Chem.* **2018**, *57* (19), 11851–11854. https://doi.org/10.1021/acs.inorgchem.8b01780.

(36) Hayashi, K.; Hosono, H. Green Apatites: Hydride Ions, Electrons and Their Interconversion in the Crystallographic Channel. *Phys. Chem. Chem. Phys.* **2016**, *18* (11), 8186–8195. https://doi.org/10.1039/C6CP00515B.

(37) Monge, M. A.; González, R.; Popov, A. I.; Pareja, R.; Chen, Y.; Kotomin, E. A.; Kuklja, M. M. The Dynamics of the Hydride Ion in MgO Single Crystals. *DDF* **1999**, *169–170*, 1–0. https://doi.org/10.4028/www.scientific.net/DDF.169-170.1.

(38) Koch, S. G.; Lavrov, E. V.; Weber, J. Photoconductive Detection of Tetrahedrally Coordinated Hydrogen in ZnO. *Phys. Rev. Lett.* **2012**, *108* (16), 165501. https://doi.org/10.1103/PhysRevLett.108.165501.

(39) Kobayashi, Y.; Hernandez, O. J.; Sakaguchi, T.; Yajima, T.; Roisnel, T.; Tsujimoto, Y.; Morita, M.; Noda, Y.; Mogami, Y.; Kitada, A.; Ohkura, M.; Hosokawa, S.; Li, Z.; Hayashi, K.; Kusano, Y.; Kim, J. eun; Tsuji, N.; Fujiwara, A.; Matsushita, Y.; Yoshimura, K.; Takegoshi, K.; Inoue, M.; Takano, M.; Kageyama, H. An Oxyhydride of $BaTiO_3$ Exhibiting Hydride Exchange and Electronic Conductivity. *Nature Mater* **2012**, *11* (6), 507–511. https://doi.org/10.1038/nmat3302.

(40) Nedumkandathil, R.; Jaworski, A.; Grins, J.; Bernin, D.; Karlsson, M.; Eklöf-Österberg, C.; Neagu, A.; Tai, C.-W.; Pell, A. J.; Häussermann, U. Hydride Reduction of $BaTiO_3$ − Oxyhydride Versus O Vacancy Formation. *ACS Omega* **2018**, *3* (9), 11426–11438. https://doi.org/10.1021/acsomega.8b01368.

(41) Yajima, T.; Takahashi, K.; Nakajima, H.; Honda, T.; Ikeda, K.; Otomo, T.; Hiroi, Z. High-Pressure Synthesis of Transition-Metal Oxyhydrides with Double-Perovskite Structures. *Inorg. Chem.* **2022**, *61* (4), 2010–2016. https://doi.org/10.1021/acs.inorgchem.1c03162.

(42) Widerøe, M. Proton and Apparent Hydride Ion Conduction in Al-Substituted SrTiO3. *Solid State Ionics* **2002**, *154–155*, 669–677. https://doi.org/10.1016/S0167-2738(02)00702-6.

(43) Steinsvik, S.; Larring, Y.; Norby, T. Hydrogen Ion Conduction in Iron-Substituted Strontium Titanate, $SrTi_{1-x}Fe_xO_{3-x}$ ($0 \leq x \leq 0.8$). **2001**.

(44) Jollands, M. C.; Balan, E. Beryllium Incorporation in Corundum. *MinMag* **2022**, *86* (5), 758–766. https://doi.org/10.1180/mgm.2022.63.

(45) Hayashi, K.; Sushko, P. V.; Hashimoto, Y.; Shluger, A. L.; Hosono, H. Hydride Ions in Oxide Hosts Hidden by Hydroxide Ions. *Nat Commun* **2014**, *5* (1), 3515. https://doi.org/10.1038/ncomms4515.
(46) Aleksis, R.; Nedumkandathil, R.; Papawassiliou, W.; Carvalho, J. P.; Jaworski, A.; Häussermann, U.; Pell, A. J. Probing the Electronic Structure and Hydride Occupancy in Barium Titanium Oxyhydride through DFT-Assisted Solid-State NMR. *Phys. Chem. Chem. Phys.* **2022**, *24* (46), 28164–28173. https://doi.org/10.1039/D2CP04675J.
(47) Misaki, T.; Oikawa, I.; Takamura, H. Negative Knight Shift in Ba-Ti Oxyhydride: An Indication of the Multiple Hydrogen Occupation. *Chem. Mater.* **2019**, *31* (18), 7178–7185. https://doi.org/10.1021/acs.chemmater.9b01434.
(48) Bell, D. R.; Rossman, G. R.; Maldener, J.; Endisch, D.; Rauch, F. Hydroxide in Olivine: A Quantitative Determination of the Absolute Amount and Calibration of the IR Spectrum: Hydroxide in Olivine. *J. Geophys. Res.* **2003**, *108* (B2). https://doi.org/10.1029/2001JB000679.

Chapter 2

BEHAVIOR OF HYDROGARNET-TYPE DEFECTS IN HYDROUS STISHOVITE AT VARIOUS TEMPERATURES AND PRESSURES

The contents of this chapter are published as an article titled "Behavior of Hydrogarnet-Type Defects in Hydrous Stishovite at Various Temperatures and Pressures" by W.R. Palfey, G.R. Rossman, and W.A. Goddard III in the Journal of Geophysical Research, Solid Earth. In this work, W.R. Palfey led the DFT calculations, supervised by both W.A. Goddard III and G.R. Rossman. All authors were involved in designing the study and preparation of the manuscript.

2.1 Introduction

Stishovite has long been established as an important phase among nominally anhydrous minerals (NAMs). Previous experimental work revealed that stishovite is capable of incorporating H_2O in concentrations up to 0.3 weight percent via a coupled substitution involving Al^{3+} (Litasov et al., 2007; Pawley et al., 1993), in a manner similar to coupled substitutions in rutile (Bromiley & Hilairet, 2005; Koudriachova et al., 2004). This resembles the mantle-stable phases δ-AlOOH and phase H ($MgSiO_2(OH_2)$), among others. Such coupled substitutions were previously accepted as the primary manner by which hydrogen is dissolved in stishovite in the high temperature and pressure conditions of the lower mantle.

However, subsequent work by Spektor et al. (2011) showed that stishovite is also capable of incorporating up to 3 wt% H_2O in the absence of Al at temperature and pressure conditions of 400 to 550 ˚C and 10 GPa, a result confirmed by both Spektor et al. (2016) and Nisr et al. (2017). Further synthesis experiments by Lin et al. (2020) and Nisr et al. (2020) found that hydrous Al-free dense silica phases (including $CaCl_2$- and niccolite-type SiO_2) remain stable at significantly higher pressures (up to 55 GPa) and temperatures (up to 1835 K) incorporating even higher concentrations of H_2O upon successive phase transitions (possibly up to 11.3 wt%). These experiments suggest that dense silica phases

may provide a hydrogen reservoir beyond subduction zones into deeper mantle regimes and large planetary interiors.

Hydrogen is thought to be incorporated into Al-free stishovite at a Si vacancy (V_{Si}) on an octahedral site ($(SiO_6)^{8-}$), which is charge compensated by forming four OH groups ($O_2(OH^-)_4$) around the vacancy (Spektor et al., 2011). Nuclear magnetic resonance (NMR) studies carried out by Spektor et al. (2011) and Spektor et al. (2016) revealed that certain populations of H in Al-free hydrous stishovite correlate directly to Si, implying a possible link to V_{Si}. This is similar to the hydrogarnet defect in Ca-rich garnets, but with one key difference: true hydrogarnet defects occur on tetrahedral sites, whereas the equivalent defect in stishovite occurs on an octahedral site. In the six-coordinated stishovite system, these silicon vacancy defects are also structurally analogous to Ruetschi defects found in various MnO_2 polymorphs, where protons compensate for Mn (IV) vacancies on six-coordinated sites (Ruetschi and Giovanoli, 1988). However, Reutschi-type defects in MnO_2 polymorphs also carry fundamental differences from their analogues in dense silica; these defects are characterized only in γ- and ε-MnO_2, neither of which has the rutile-type structure of stishovite. More similar to hydrogarnet-type structures in stishovite are V_{Ti} defects in rutile-type TiO_2 and MnO_2. Such defects have been proposed for H incorporation in rutile (Bjørheim et al., 2010, Bjørheim et al., 2013) and pyrolusite (Balachandran et al., 2003), but these defects may also differ from their counterparts in stishovite. The smaller oxygen-oxygen distances in stishovite leave less room for OH groups than in rutile, which could lead to different restrictions on which oxygen atoms form OH.

Spektor et al. (2011, 2016) concluded from their NMR studies that multiple configurations of these Si-linked hydrogens are likely to coexist in stishovite. However, they proposed only one configuration wherein the four H atoms are arranged with tetrahedral symmetry and the four OH groups form strong hydrogen bonds with the two remaining unoccupied oxygen atoms. Subsequent Raman measurements by Nisr et al. (2017) observed several OH modes suggesting coexistence of multiple types of hydrogarnet defects. Nevertheless, it is unclear if the multiple modes are due to multiple defect configurations, lower symmetry defects, or proton dynamics. Additionally, infrared

data from Spektor et al. (2011, 2016) show the existence of sharp bands centered at 1420 cm^{-1} associated with hydrogen, possibly related to SiOH bending.

Here, we use density functional theory (DFT) methods to predict the energies, geometries, and OH vibrational frequencies for configurations of OH surrounding the V_{Si} site in stishovite. We predict the most energetically favorable configurations of the $(OH^-)_4$ Ruetschi-like hydrogarnet defect in stishovite, the positions of their associated hydrogen-related vibrational modes, and their behavior at the synthesis and analysis conditions of Spektor et al. (2011 and 2016).

2.2 Materials and Methods

2.2.1 Details of Calculations

We performed three varieties of calculations: structural minimizations, phonon calculations of the minimized structures using density functional perturbation theory (DFPT), and quantum mechanics molecular dynamics (QM MD) at various temperatures and pressures. All DFT calculations used the Vienna Ab initio Simulation Package (VASP, version 5.4.4.18Apr17). These calculations used the Perdew-Burke-Ernerhof (PBE) generalized gradient approximation to describe the exchange correlation (Blöchl, 1994; Kresse & Furthmüller, 1996a, 1996b; Kresse & Hafner, 1993; Kresse & Joubert, 1999; Perdew et al., 1996; Perdew et al., 1997), along with the empirical D3 van Der Waals correction (Grimme et al., 2010, 2011). The cutoff energy for the plane-wave basis set was 500 eV and energy smearing near the Fermi energy was handled through the tetrahedron method with a smearing width of 0.05 eV and Blöchl corrections (Blöchl et al., 1994). A 5×5×5 Monkhorst−Pack mesh was found to be sufficient to optimize structures for our unit cell size (discussed below) to converge energy values within 1 meV for structural minimizations. Atomic forces were minimized to a value of 0.01 eV/Å. The DFPT calculations used a reduced 2×2×2 k-point mesh and estimated infrared intensities were calculated from the Born effective charges.

QM MD was performed via VASP using an NVT ensemble with a Nosé-Hoover thermostat, using 1 fs time steps and temperature corrections every 40 fs. These parameters

were found to be sufficient for stabilizing temperature, pressure, and the kinetic and potential energies of the simulated system. For all configurations tested, the QM MD calculations consisted of three parts: heating the system from 10 K to the target temperature over the course of 10 ps, allowing the system to equilibrate at the target temperature for 3 ps, and holding the system at the target temperature for 20 ps. The final 20 ps run was then used to calculate the temperature, pressure, and energy of the system at simulated conditions.

QM MD calculations were carried out at four different temperatures: 450 ˚C (representing optimal experimental synthesis conditions from Spektor et al. (2016)), 25 ˚C (representative of the conditions under which experimental data were collected on quenched samples), 500 ˚C (to estimate behavior just above optimal conditions) and 262 ˚C (the temperature halfway between the highest and lowest simulated). The results of the QM MD calculations were then used to calculate the phonon density of states (DoS) in a manner similar to Wilson and Stixrude (2021) via Fourier transform of the velocity autocorrelation function using the two phase thermodynamics (2PT) code (Lin et al., 2003; Lin et al., 2010; Pascal et al., 2011).

2.2.2 Creation of Defect Structures

We used a 2×2×3 unit cell containing 24 Si sites and 48 O sites. When one Si atom is removed and four H are placed in the 2×2×3 cell, the resulting concentration of H_2O is 2.54 wt%. For all calculations, the unit cell parameters were fixed at a=4.1953 Å, c=2.665 Å, consistent with the dimensions measured for hydrous, Al-free stishovite by Spektor et al. (2011) and Spektor et al. (2016). Based on unit cell volumes, this corresponds to ~ 2.0 wt% H_2O at 10 GPa (Nisr et al., 2017).

A conventional hydrogarnet defect occurs on a tetrahedral Si site, where all four O atoms surrounding V_{Si} form OH bonds. In contrast, the Ruetschi-style hydrogarnet defect proposed for stishovite occurs on a distorted octahedral Si site, leading to many possible configurations for the four OH. This has been suggested by prior authors as a factor contributing to the breadth of the OH bands observed in Al-free stishovite (Spektor et al.,

2011). Additionally, other systems with six-coordinated silica have been predicted to simultaneously incorporate several configurations of hydrogarnet-type defects (Shim et al., 2022). Thus, to thoroughly test the likely arrangement of OH around V_{Si}, we tested many arrays of OH, taking into account both the selection of O sites for protonation and the resulting OH orientations.

Our initial studies of various configurations revealed that OH almost exclusively orients itself skew to both *a* and *c*, at a slight slant from the edges of the octahedral Si site, regardless of starting position. Subsequent configurations tested were restricted to include only OH oriented in this manner. Operating under this constraint, and accounting for the orthorhombic symmetry of the V_{Si} site, we derived and tested 64 possible arrangements for 4 OH groups around V_{Si} (details of these arrangements are found in the supplementary material).

2.3 Results

2.3.1 Structural minimizations

Starting with the 64 possible unique arrays of OH around V_{Si}, we found that all configurations converged to just one of seven structures, briefly summarized below:

- The most favorable configuration is the tetrahedral case shown in Figure 2.1. This is the only structure important at 25 ˚C.
- The next most favorable is the square planar case shown in Figure 2.1. It is ~ 0.140 eV higher energy than the tetrahedral case. Based on this energy difference, it would be populated ~ 0.65% at 25 ˚C and ~11.5% at 450 ˚C.
- The other five cases have energies ~0.50 to 1.31 eV higher and hence are not important at temperatures of 450 ˚C and below.

Thus, we predict that only two configurations are likely to be relevant in Al-free stishovite at elevated temperatures and only one is important at 298 K. We focused on just these two structures for the remaining calculations. Models of the two structures are presented in

Figure 2.1. Details of the remaining five configurations are included in the supplementary material.

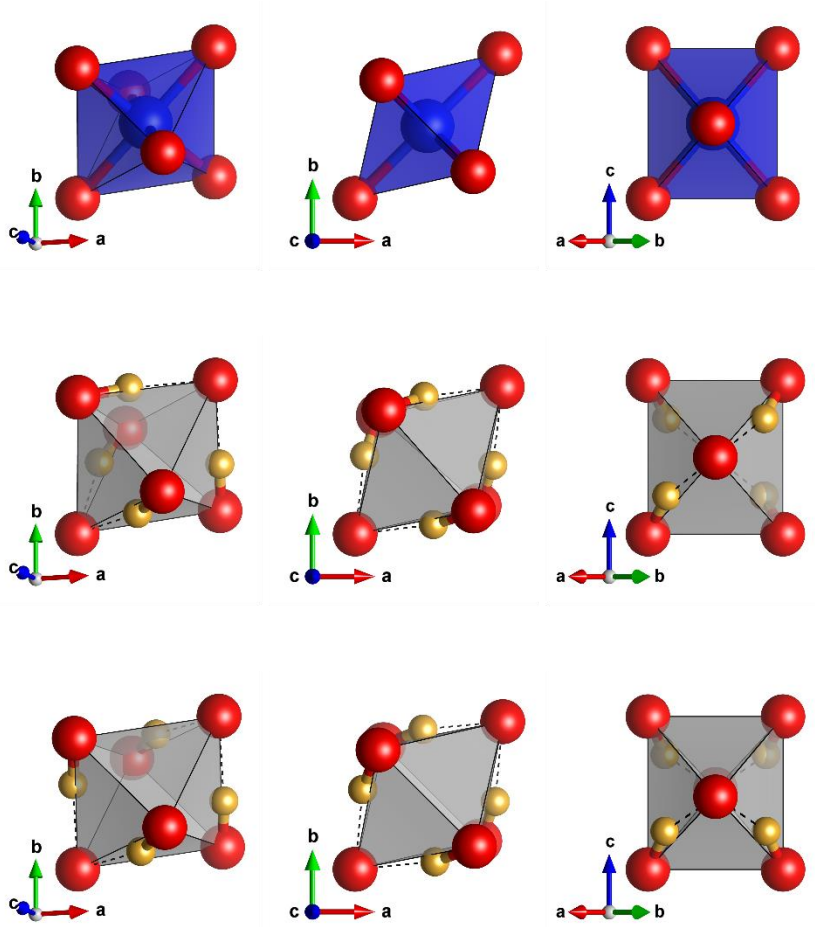

Figure 2.1 *Different views of the ideal Si site in stishovite (top row), the tetrahedral case (middle row) and the square planar case (bottom row). In the tetrahedral case, OH on opposing corners hydrogen bond to the same axial atom, while in the square planar case, OH that are c-perpendicular hydrogen bond to the same axial atom.*

The lowest energy configuration consists of OH groups populating only the four basal O atoms of the octahedral Si site. All OH bonds are oriented such that they are slightly skew to the edges of the V_{Si} octahedron, forming hydrogen bonds with one of the two axial O atoms having no H. The OH orientations alternate, with OH on opposing corners of the octahedral base pointing to the same axial O atom. This results in the H atoms forming a nearly tetrahedral shape around V_{Si}, similar to the defect suggested by Spektor et al. (2011). All four d(O-H···O) are ~2.55 Å, while H atoms hydrogen bonded to the same axial O atoms are separated by 2.22 Å. The slight skew of the OH groups off of the octahedral

edges gives the entire defect (including all six oxygens) C_2 symmetry. When the hydrogen positions are considered independent of the oxygen atoms, the resulting configuration has tetrahedral symmetry. Thus, we refer to this defect as the tetrahedral case.

The second lowest energy configuration also consists of four OH groups on the basal O atoms surrounding V_{Si}, with hydrogen bonding to axial O atoms. However, in contrast to the tetrahedral case, the OH groups form *c*-perpendicular pairs, each pointing to the same axial O atom. This results in the H atoms forming a square planar configuration. All four d(O-H⋯O) are ~2.52 Å, while H atoms hydrogen bonded to the same axial O atoms are separated by only 1.82 Å, significantly closer than in the tetrahedral case and likely responsible for the higher energy. An alternate square planar configuration with c-parallel OH pairs, rather than c-perpendicular pairs, leads to an energy 0.67 eV higher. This is likely due to decreased H-H distances (1.57 Å) resulting in increased H-H repulsion. The square planar defect site (including oxygen atoms) has C_{2h} symmetry. It is 0.14 eV higher energy than the tetrahedral case.

2.3.2 Vibrational modes calculated using DFPT

DFPT calculations predict that both the tetrahedral and square planar cases should produce multiple infrared-active OH stretching and bending modes. The predicted stretching modes are positioned from 2704 to 2871 cm^{-1} for the tetrahedral case and 2683 to 2887 cm^{-1} for square planar, all within range of the modes observed by Spektor et al. (2011, 2016). The two SiOH bending modes for the tetrahedral case are at 1420 and 1362 cm^{-1} while they are at 1520 and 1390 cm^{-1} for the square planar case. For both cases, one of these bending modes is predicted to have a far higher infrared activity than the other. Given the predicted abundances of the tetrahedral and square planar defects, the tetrahedral case provides an explanation for the 1420 cm^{-1} mode observed experimentally (see Figure 2.2 and Table 2.1). The SiOH bending modes are calculated to have a significantly lower infrared activity compared to the OH stretching modes.

These trends hold true for the calculated deuterium modes. Experimental data show that the 1420 cm^{-1} mode shifts to 1079 cm^{-1}. Our predicted SiOD bending mode for the

tetrahedral defect matches the position of this feature well; the calculated mode is positioned at 1069 cm^{-1}. However, the tetrahedral defect does not provide a complete explanation for this region of the spectrum. Upon deuteration, there appears to be some residuum of the 1420 cm^{-1} mode at 1383 cm^{-1}. None of our calculated modes account for this, which we discuss further below.

Three OH stretching modes are predicted to be infrared active for the tetrahedral defect:

- 2871 cm^{-1} corresponds to symmetric stretching of OH on opposing corners, maintaining the overall C_2 symmetry of the defect site.
- 2750 cm^{-1} corresponds to the symmetric combination of OH stretches of the c-perpendicular pairs
- 2704 cm^{-1} corresponds to the symmetric combination of OH stretches of c-parallel pairs.

The latter two modes break the C_2 symmetry of the site while maintaining all H-H distances. The square planar defect is predicted to have two infrared-active modes:

- 2887 cm^{-1} corresponds to symmetric stretching of the c-perpendicular OH pairs
- 2683 cm^{-1} corresponds to symmetric stretching of the c-parallel pairs.

For both the tetrahedral and square planar defects, OH bonds are oriented skew to both *c* and *a* such that OH stretching modes should be of roughly equivalent intensity regardless of polarization direction. The same holds true for the bending modes of the tetrahedral case, but not the square planar case, where bending modes are polarized strongly perpendicular to the c-axis.

Tetrahedral:

Motion	OH (cm^{-1})	OD (cm^{-1})
OX stretch	2871	2099
	2750	2012
	2704	1983
Si-OX bend	1420	1069
	1362	1030

Square Planar:

Motion	OH (cm^{-1})	OD (cm^{-1})
OX stretch	2887	2109
	2683	1968
Si-OX bend	1520	1118
	1390	1055

Table 2.1 *Summary of the infrared active OH and OD stretching and bending modes for the tetrahedral case (left) and the square planar case (right). Note that additional OH/OD modes are, strictly speaking, infrared-active, but their predicted intensities are several orders of magnitude lower and unlikely to be observed experimentally.*

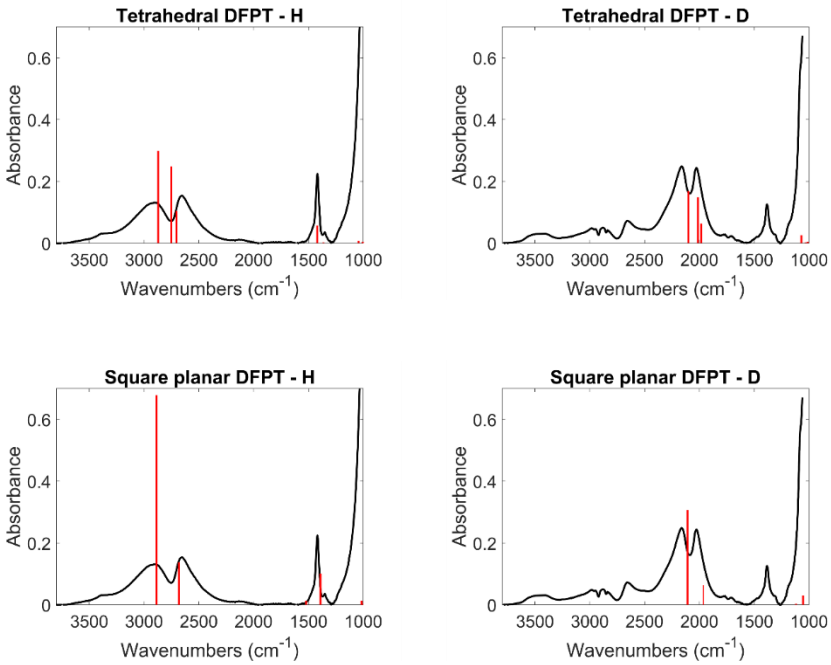

Figure 2.2 *Comparisons between the experimental data of Spektor et al., 2016 (black) and DFPT calculated modes, weighted by calculated intensities (red vertical lines). DFPT modes in the upper two plots were calculated from the tetrahedral case, while the lower two plots were calculated from the square planar case. Both hydrogen (left) and deuterium (right) are presented.*

2.3.3 QM molecular dynamics and phonon DoS

For static (0 K) calculations, the tetrahedral case is energetically preferable to the square planar case by 0.140 eV. For our molecular dynamics calculations we calculated the Boltzmann factor at each temperature. We find that the proportion of tetrahedral to square planar defects should be 111:1 at 25 ˚C but it becomes 50:46 at 500 ˚C (see Table 2.2). Because we performed NVT dynamics, the external pressure is not constrained, resulting in different pressure values for each temperature. We include the resulting total pressure values (combined external and kinetic pressure terms) in Table 2.2, along with the total energy (summed potential and kinetic energies) and temperature, which varies slightly between simulations.

Tetrahedral case:			Square planar case:		
Run	**Energy (eV)**	**Pressure (kB)**	**Energy (eV)**	**Pressure (kB)**	**Boltzmann Factor**
0 K	-571.192	76.3	-571.052	77.7	N/A
25 ˚C	-564.061	93.7	-563.942	97.6	0.009
262 ˚C	-559.532	108.4	-559.426	113.3	0.097
450 ˚C	-555.895	118.3	-555.827	125.8	0.329
500 ˚C	-554.879	121.9	-554.873	127.5	0.923

Table 2.2 *Average total energy and pressure values for each QM MD simulation. The Boltzmann factor for the square planar case at each simulated condition (based on average temperatures between the simulations) is also presented. The 0 K values from the minimized structure are also presented in the top row.*

The phonon densities of states for each dynamics run are presented in Figure 2.3. For the tetrahedral case, predicted modes in the SiOH bending region consist of three distinct peaks at 25 ˚C, but with increasing temperatures and pressures, they broaden and become less distinct. These SiOH bending modes are predicted at the same position as the mysterious 1420 cm^{-1} peak observed by Spektor et al. (2011, 2016).

The square planar phonon densities predict OH stretches to have a close distribution of modes at room temperature, broadening less than the OH modes of the tetrahedral case with increased pressure and temperature, while also producing modes at significantly lower and higher frequencies. This might be due to increased hydrogen bonding with oxygen (lower d(O-H···O)) and increased H-H repulsion, as proposed by Nisr et al. (2017). Notably, the square planar structure results in no features in the ~1420 cm^{-1} region, in contrast with experimental data.

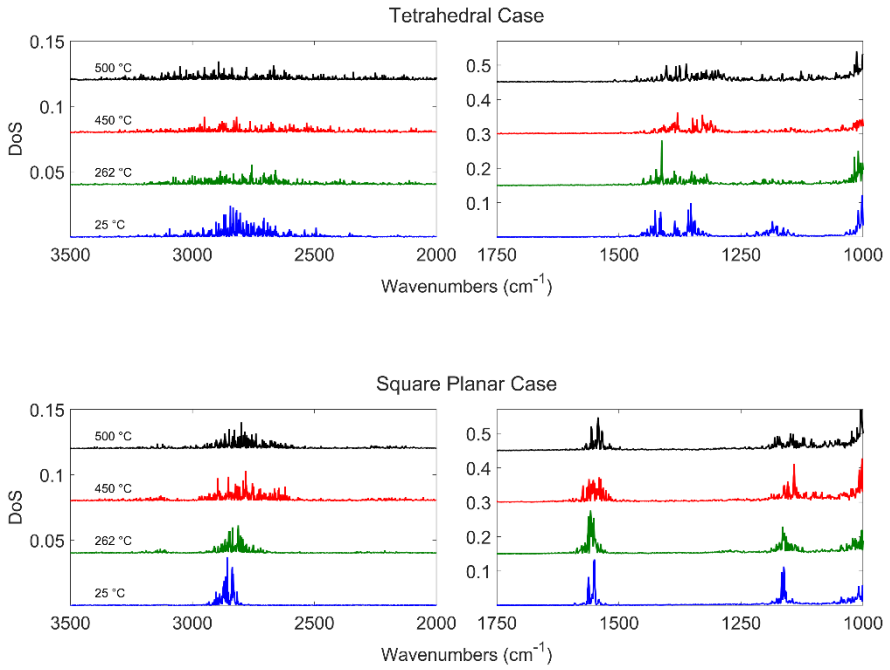

Figure 2.3 *The phonon density of states for the tetrahedral case (top) and square planar case (bottom) at each simulated temperature (25 ˚C, 262 ˚C, 450 ˚C and 500 ˚C). Enlarged plots of the OH stretching and bending regions are presented for each case. For both defect configurations, increasing the pressure and temperature significantly broadens the OH stretching and SiOH bending modes. Notably, the tetrahedral case produces a wide distribution of OH stretches even at 25 ˚C. Thus, the single tetrahedral case can explain the multiple bands observed experimentally. Most important is that the tetrahedral case finds the SiOH bending modes at ~1420 cm^{-1} whereas the square planar case puts this above 1500 cm^{-1}.*

2.4 Discussion

Our structural minimization and QM MD calculations at 298K predict that the important configuration for the hydrogarnet-type defect in stishovite at 25 ˚C is the tetrahedral case. Notably, this defect configuration is different from the defects proposed by Balachandran et al. (2003) and Bjørheim et al. (2013) for the for rutile-type polymorphs of MnO_2 and TiO_2, respectively. Although these two defects both involve H atoms in a tetrahedral configuration, they include protonation of different oxyen atoms. Additionally, when defects equivalent to Balachandran et al. (2003) and Bjørheim et al. (2013) were relaxed in the stsihovite structure, alternate configurations resulted. We propose that this is likely due to the density of the stishovite structure compared to pyrolusite and rutile; oxygen atoms in stishovite are closer together, which likely translates to different

restrictions on combinations of OH groups. A more detailed comparison between the stishovite, rutile and pyrolusite defects can be found in the SI.

Our tetrahedral model is similar to the one proposed by Spektor et al. (2011), differing only in subtle changes to the OH bond orientations (in our structures, the OH bonds are slightly skewed relative to the octahedral edges). However, in contrast to hypotheses by prior authors, our calculations predict that only the tetrahedral defect configuration is important at 25 ˚C. The tetrahedral defect structure explains the several OH stretching modes observed experimentaly, in contrast to the multiple defect states suggested to explain the broad distribution of vibrational modes proposed previously. We find the square planar configuration has a population of 1% at 25 ˚C, but a population of 45% at 450 ˚C. Thus, the square planar configuration is relevant only at the pressure and temperatures of synthesis (450 ˚C and 10 GPa) and higher. Additionally, our results suggest that it is possible for this defect type to become dominant at higher pressures and temperatures.

Overall, our QM calculated OH modes match the infrared data of Spektor et al. (2011, 2016), with only a few minor incongruences. The broad OH modes centered at 2904 and 2656 cm^{-1} present in low-temperature-synthesized stishovite can be compared to predicted modes at 2704, 2750, and 2871 cm^{-1} for the tetrahedral defect and 2683 and 2887 cm^{-1} for the square planar defect. These two defect structures are consistent with the experimental data, since the short hydrogen bonding distances in these defects correspond to low cm^{-1} OH modes, as detailed in Libowitzky et al. (1999).

Calculated stretching modes for deuterium similarly match the experimental OD modes. Our tetrahedral hydrogarnet-type defect also explains the “mysterious” modes observed by Spektor et al. (2011, 2016) centered near 1420 cm^{-1}. Our results indicate that the tetrahedral planar defects produce SiOH bending modes near 1420 cm^{-1}, whereas square planar defect leads to modes at 1390 cm^{-1} and above 1500 cm^{-1}. Upon deuteration, our calculations predict that the bending mode shifts to 1069 cm^{-1}, within 10 cm^{-1} of a mode observed in the infrared data of Spektor et al. (2016). However, it is important to note that although some deuterium modes shift by the magnitude expected for the SiOH bend, a significant population shifts by only about 40 cm^{-1} down to 1383 cm^{-1}. This suggests that,

although the 1420 cm^{-1} mode is associated with hydrogen, some of the modes in the 1420 cm^{-1} region may not be due to SiOH bending.

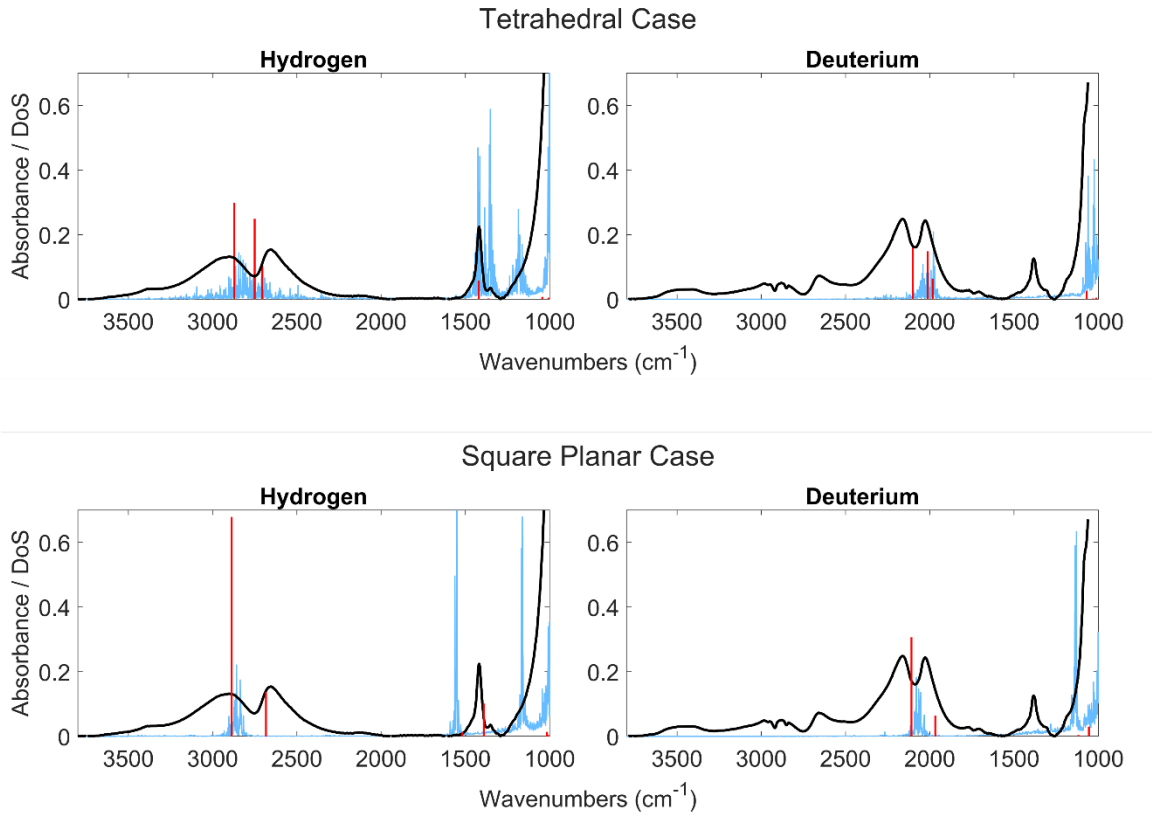

Figure 2.4 *Comparison of the predicted DFPT modes at 0K (red) and the vibrational density of states (DoS) at 298 K (blue) from QMMD for the tetrahedral defect (top row) and square planar defect (bottom row) with the experimental spectrum (black) from Spektor et al. (2016). Spectra for both hydrogen (left) and deuterium (right) are presented. There is general consistency between the predicted DoS spectrum and experiment for OH/OD stretches and SiOH/SiOD bends for the tetrahedral case, including the 1079 cm^{-1} mode in the deuterated spectrum. The square planar case provides a poor match for the bending modes located near 1400 cm^{-1}. Notably, no vibrational mode is predicted near the 1383 cm^{-1} mode for deuterated spectra, suggesting it is not due to SiOD bending.*

Our predicted vibrational DoS provides additional insight into the behavior of the hydrogarnet-type defect in stishovite. The 298 K spectra of the tetrahedral case shows behavior largely consistent with the infrared data presented by Spektor et al. (2011, 2016); the OH modes are broad and located in the range of 2500 – 3000 cm^{-1}, with a possible separation between two groups of modes. In contrast, the square planar case forms a narrower cluster of OH modes at higher energy. Most importantly, the ~1420 cm^{-1} bending

mode is present in the tetrahedral case spectra, but this feature is at ~ 1550 cm^{-1} in the square planar spectrum. This indicates that the tetrahedral structure is truly dominant in quenched hydrous stishovite. Although we predict the square planar case exists in negligible quantities in quenched samples, this defect should have comparable abundances to the tetrahedral defect at the synthesis temperature of 450 ˚C and 10 GPa. Thus, we expect these higher wavenumber OH bending modes to emerge when measurements are taken in situ.

Previous authors have attributed the broadness of the OH bending modes in hydrous stishovite to the coexistence of multiple tetrahedral configurations. Instead, our calculations show that the breadth of predicted OH modes for just the single tetrahedral case is comparable to the experimental data (Figure 2.4). The inclusion of proton dynamics, resulting in a high variability of d(O-H···O), and H-H repulsion induced by molecular dynamics simulations produces significant peak broadening, even at room temperature. Thus, we find that our single tetrahedral defect is sufficient to explain the observed OH character in hydrous stishovite at room temperature.

Nonetheless, it is possible that additional defect configurations may be present. For example, clusters of hydrogarnet-type defects could exist between adjacent V_{Si} sites, such as has been suggested by Nisr et al. (2017), leading to a wider range of hydrogen bonding distances and lower local symmetries. Such clusters almost certainly exist in extremely hydrous (~4.3% +), high pressure dense silica, as was synthesized by Nisr et al. (2020). At these concentrations, the $(OH)_4$ defect density would be such that directly adjacent defects would be inevitable.

Other native defects could also couple to hydrogen in stishovite. These types of defects are well-documented in the rutile system and could result in OH modes more consistent with some experimental data. Specifically, Litasov et al. (2007) and others report OH modes from 3312 to 3189 cm^{-1} polarized perpendicular to the c-axis in systems for which Al concentrations are too low to account for all hydrogen incorporated. In such defects, OH would orient in in a manner similar to the “channel centered” orientation described for oxygen-deficient rutile and δ-AlOOH. Such an orientation in stishovite would lead to more space between hydrogen and the neighboring oxygen atom, leading to weaker

hydrogen bonding and higher wavenumber vibrations. Additionally, the tetrahedral hydrogarnet defect may not fully account the sharp modes located at 1420 cm^{-1}. Only a portion of the population shifts to 1069 cm^{-1} as expected for the SiOH bend, but the remainder shifts only to 1383 cm^{-1}. Although our DFPT calculated SiOD modes match the 1069 cm^{-1} mode well, they provide no explanation for the 1383 cm^{-1} mode. Furthermore, the phonon DoS for the tetrahedral case at 25 ˚C (as shown in Figure 2.4) show that the tetrahedral case does not produce a mode near 1383 cm^{-1} when deuterated. This strongly suggests that alternate defects contribute to modes in the 1420 cm^{-1} / 1383 cm^{-1} region. Scenarios involving either V_{Si} clusters, V_O, interstitial species, or other defects remain uninvestigated and could be the subject of future studies.

Our calculations target only a limited slice of the overall behavior observed in hydrous dense silica phases. Hydrous rutile-type SiO_2, although stable in the pressure and temperature ranges we simulated here, transitions to $CaCl_2$- and then niccolite-type SiO_2 structures at much lower pressures than its anhydrous counterpart, with increased capability to sequester hydrogen at each phase transition (Nisr et al., 2020). Whether additional tetrahedral arrangements become more stable in these higher-pressure phases, or square planar or other defect configurations become dominant remains to be seen. Calculations undertaken by Nisr et al. (2020) demonstrated that the volume increases observed in the $CaCl_2$ structure with increasing H_2O content are consistent with the experimental work of Spektor et al. (2016) and Nisr et al. (2017) when a tetrahedral configuration is selected. Additional work could reveal more nuanced behavior of Reutschi-like hydrogarnet defects in these more hydrous, higher-pressure phases, where an increased population of V_{Si} could result in complex defect clusters.

2.5 Conclusions

Our QM calculations show that only one hydrogarnet-type defect state is important in stishovite at room temperature. This defect contains four OH groups arranged such that the hydrogen atoms have a tetrahedral geometry. The tetrahedral defect results in OH stretching modes that can fully account for the broad features observed via infrared spectroscopy, in contrast to earlier speculation of multiple, coexisting defect states. In

addition to this, we find that a second defect state with square planar geometry becomes prominent at higher pressures and temperatures, coexisting with the tetrahedral defect in nearly equal proportion. These studies set the stage for future simulations of hydrogarnet-type defects in higher pressure polymorphs of dense silica that are stable in lower mantle and large planetary interior conditions.

Acknowledgments

The authors thank Charles Musgrave for helpful discussions.

W.A.G. was supported by the Liquid Sunlight Alliance, which is supported by the U.S. Department of Energy, Office of Science, Office of Basic Energy Sciences, Fuels from Sunlight Hub, under Grant DE-SC0021266. G.R.R. is thankful for National Science Foundation Grant EAR-2149559.

References

Balachandran, D., Morgan, D., Ceder, G., van de Walle, A. (2003). First-Principles Study of the Structure of Stoichiometric and Mn-Deficient MnO_2. *Journal of Solid State Chemistry*, *173*(2), 462–475. https://doi.org/10.1016/S0022-4596(03)00023-9.

Bjørheim, T. S., Kuwabara, A., & Norby, T. (2013). Defect Chemistry of Rutile TiO_2 from First Principles Calculations. *The Journal of Physical Chemistry C*, *117*(11), 5919–5930. https://doi.org/10.1021/jp304146e

Bjørheim, T. S.; Stølen, S.; Norby, T. (2010). Ab Initio Studies of Hydrogen and Acceptor Defects in Rutile TiO_2. *Phys. Chem. Chem. Phys*, *12*(25), 6817–6825. https://doi.org/10.1039/b925823j.

Blöchl, P. E. (1994). Projector augmented-wave method. *Physical Review B*, *50*(24), 17953–17979. https://doi.org/10.1103/PhysRevB.50.17953

Blöchl, P. E., Jepsen, O., & Andersen, O. K. (1994). Improved tetrahedron method for Brillouin-zone integrations. *Physical Review B*, *49*(23), 16223–16233. https://doi.org/10.1103/PhysRevB.49.16223

Bromiley, G. D., & Hilairet, N. (2005). Hydrogen and minor element incorporation in synthetic rutile. *Mineralogical Magazine*, *69*(3), 345–358. https://doi.org/10.1180/0026461056930256

Grimme, S., Antony, J., Ehrlich, S., & Krieg, H. (2010). A consistent and accurate *ab initio* parametrization of density functional dispersion correction (DFT-D) for the 94 elements H-Pu. *The Journal of Chemical Physics*, *132*(15), 154104. https://doi.org/10.1063/1.3382344

Grimme, S., Ehrlich, S., & Goerigk, L. (2011). Effect of the damping function in dispersion corrected density functional theory. *Journal of Computational Chemistry*, *32*(7), 1456–1465. https://doi.org/10.1002/jcc.21759

Koudriachova, M. V., de Leeuw, S. W., & Harrison, N. M. (2004). First-principles study of H intercalation in rutile TiO_2. *Physical Review B*, *70*(16), 165421. https://doi.org/10.1103/PhysRevB.70.165421

Kresse, G., & Furthmüller, J. (1996a). Efficiency of ab-initio total energy calculations for metals and semiconductors using a plane-wave basis set. *Computational Materials Science*, *6*(1), 15–50. https://doi.org/10.1016/0927-0256(96)00008-0

Kresse, G., & Furthmüller, J. (1996b). Efficient iterative schemes for *ab initio* total-energy calculations using a plane-wave basis set. *Physical Review B*, *54*(16), 11169–11186. https://doi.org/10.1103/PhysRevB.54.11169

Kresse, G., & Hafner, J. (1993). *Ab initio* molecular dynamics for liquid metals. *Physical Review B*, *47*(1), 558–561. https://doi.org/10.1103/PhysRevB.47.558

Kresse, G., & Hafner, J. (1994). *Ab initio* molecular-dynamics simulation of the liquid-metal–amorphous-semiconductor transition in germanium. *Physical Review B*, *49*(20), 14251–14269. https://doi.org/10.1103/PhysRevB.49.14251

Kresse, G., & Joubert, D. (1999). From ultrasoft pseudopotentials to the projector augmented-wave method. *Physical Review B*, *59*(3), 1758–1775. https://doi.org/10.1103/PhysRevB.59.1758

Libowitzky, E. (1999). Correlation of O-H Stretching Frequencies and O-H···O Hydrogen Bond Lengths in Minerals. *Chemical Monthly*, *130*, 1047–1059.

Lin, S.-T., Blanco, M., & Goddard, W. A. (2003). The two-phase model for calculating thermodynamic properties of liquids from molecular dynamics: Validation for the phase diagram of Lennard-Jones fluids. *The Journal of Chemical Physics*, *119*(22), 11792–11805. https://doi.org/10.1063/1.1624057

Lin, S.-T., Maiti, P. K., & Goddard, W. A. (2010). Two-Phase Thermodynamic Model for Efficient and Accurate Absolute Entropy of Water from Molecular Dynamics

Simulations. *The Journal of Physical Chemistry B*, *114*(24), 8191–8198. https://doi.org/10.1021/jp103120q

Lin, Y., Hu, Q., Meng, Y., Walter, M., & Mao, H.-K. (2020). Evidence for the stability of ultrahydrous stishovite in Earth's lower mantle. *Proceedings of the National Academy of Sciences*, *117*(1), 184–189. https://doi.org/10.1073/pnas.1914295117

Litasov, K. D., Kagi, H., Shatskiy, A., Ohtani, E., Lakshtanov, D. L., Bass, J. D., & Ito, E. (2007). High hydrogen solubility in Al-rich stishovite and water transport in the lower mantle. *Earth and Planetary Science Letters*, *262*(3–4), 620–634. https://doi.org/10.1016/j.epsl.2007.08.015

Nisr, C., Chen, H., Leinenweber, K., Chizmeshya, A., Prakapenka, V. B., Prescher, C., Tkachev, S. N., Meng, Y., Liu, Z., & Shim, S.-H. (2020). Large H_2O solubility in dense silica and its implications for the interiors of water-rich planets. *Proceedings of the National Academy of Sciences*, *117*(18), 9747–9754. https://doi.org/10.1073/pnas.1917448117

Nisr, C., Leinenweber, K., Prakapenka, V., Prescher, C., Tkachev, S., & Shim, S. -H. D. (2017). Phase transition and equation of state of dense hydrous silica up to 63 GPa. *Journal of Geophysical Research: Solid Earth*, *122*(9), 6972–6983. https://doi.org/10.1002/2017JB014055

Nisr, C., Shim, S.-H., Leinenweber, K., & Chizmeshya, A. (2017). Raman spectroscopy of water-rich stishovite and dense high-pressure silica up to 55 GPa. *American Mineralogist*, *102*(11), 2180–2189. https://doi.org/10.2138/am-2017-5944

Pascal, T. A., Lin, S.-T., & Goddard III, W. A. (2011). Thermodynamics of liquids: Standard molar entropies and heat capacities of common solvents from 2PT molecular dynamics. *Phys. Chem. Chem. Phys.*, *13*(1), 169–181. https://doi.org/10.1039/C0CP01549K

Pawley, A. R., McMillan, P. F., & Holloway, J. R. (1993). Hydrogen in Stishovite, with Implications for Mantle Water Content. *Science*, *261*(5124), 1024–1026. https://doi.org/10.1126/science.261.5124.1024

Perdew, J. P., Burke, K., & Ernzerhof, M. (1996). Generalized Gradient Approximation Made Simple. *Physical Review Letters*, *77*(18), 3865–3868. https://doi.org/10.1103/PhysRevLett.77.3865

Perdew, J. P., Burke, K., & Ernzerhof, M. (1997). Generalized Gradient Approximation Made Simple [Phys. Rev. Lett. 77, 3865 (1996)]. *Physical Review Letters*, *78*(7), 1396–1396. https://doi.org/10.1103/PhysRevLett.78.1396

Ruetschi, P.; Giovanoli, R. (1988). Cation Vacancies in MnO_2 and Their Influence on Electrochemical Reactivity. *Journal of the Electrochemical Society*, *135* (11), 2663–2669. https://doi.org/10.1149/1.2095406.

Shim, S.-H., Chizmeshya, A., & Leinenweber, K. (2022). Water in the crystal structure of $CaSiO_3$ perovskite. *American Mineralogist*, *107*(4), 631–641. https://doi.org/10.2138/am-2022-8009

Spektor, K., Nylen, J., Mathew, R., Edén, M., Stoyanov, E., Navrotsky, A., Leinenweber, K., & Häussermann, U. (2016). Formation of hydrous stishovite from coesite in high-pressure hydrothermal environments. *American Mineralogist*, *101*(11), 2514–2524. https://doi.org/10.2138/am-2016-5609

Spektor, K., Nylen, J., Stoyanov, E., Navrotsky, A., Hervig, R. L., Leinenweber, K., Holland, G. P., & Haussermann, U. (2011). Ultrahydrous stishovite from high-pressure hydrothermal treatment of SiO_2. *Proceedings of the National Academy of Sciences*, *108*(52), 20918–20922. https://doi.org/10.1073/pnas.1117152108

Wilson, A.; Stixrude, L. (2021). Entropy, Dynamics, and Freezing of $CaSiO_3$ Liquid. *Geochimica et Cosmochimica Acta*, *302*, 1–17. https://doi.org/10.1016/j.gca.2021.03.015.

Chapter 3

STRUCTURE, ENERGETICS, AND SPECTRA FOR THE OXYGEN VACANCY IN RUTILE: PROMINENCE OF THE Ti−H_O−Ti BOND

The contents of this chapter are published as an article titled "Structure, Energetics and Spectra for the Oxygen Vacancy in Rutile: Prominence of the Ti-H_O-Ti Bond" by W.R. Palfey, G.R. Rossman, and W.A. Goddard III in the Journal of Physical Chemistry Letters. In this work, W.R. Palfey led the DFT calculations, supervised by both W.A. Goddard III and G.R. Rossman. All authors were involved in designing the study and preparation of the manuscript.

3.1 Introduction

The rutile phase of TiO_2 is among the most technologically important and extensively studied oxides. Prior work has revealed many key properties of rutile, including its catalytic activity and tendency for n-type conductivity, which are influenced by its defect chemistry.[1,2] Although most attention has been paid to the role of oxygen and titanium vacancies in this context, interstitial hydrogen (typically forming OH bonds and often denoted as H_i) has been proposed to significantly affect the material properties of rutile.[3,4] The incorporation of hydrogen is strongly linked to the presence of oxygen vacancies and is considered ubiquitous in rutile produced under reducing conditions.[5] As a naturally occurring mineral, rutile is among the most hydrogen-rich of the so-called nominally anhydrous minerals (NAMs). Mantle derived rutile crystals are demonstrated to incorporate hydrogen at concentrations approaching 10000 μg/g of H_2O.[6–8] Additionally, stishovite (rutile-type SiO_2), a known major component of Earth's mantle, can incorporate similar amounts of hydrogen.[9] As a result, the rutile structure has been widely studied in efforts to understand hydrogen sequestration in NAMs.

Despite the importance of hydrogen to the defect chemistry and material properties of rutile, much remains unknown about the specifics surrounding the incorporation of hydrogen into rutile. Syntheses of rutile under reducing conditions reveal that hydrogen

couples to oxygen vacancies, forming OH.[5,10] Numerous infrared studies have demonstrated consistent OH bond polarization,[11–13] but a comprehensive description of the interaction between oxygen vacancies and hydrogen has not been reported. Ambiguity still surrounds the orientation of the OH bond with respect to crystal axes. Infrared data show that the OH bonds are perpendicular to rutile's *c*-axis but do not specify a particular direction. Prior quantum mechanics (QM) calculations (confirmed here) find the OH bond is perpendicular to the *c*-axis in a "channel-centered" (CC) direction. In contrast, a single neutron scattering study of mantle-derived rutile found an alternate, "basal octahedral edge" (BOE) direction,[8] in agreement with Raman analyses of Al-doped rutile.[14] In addition to this discrepancy, the preferred positions of H_i relative to oxygen vacancies remain unknown.

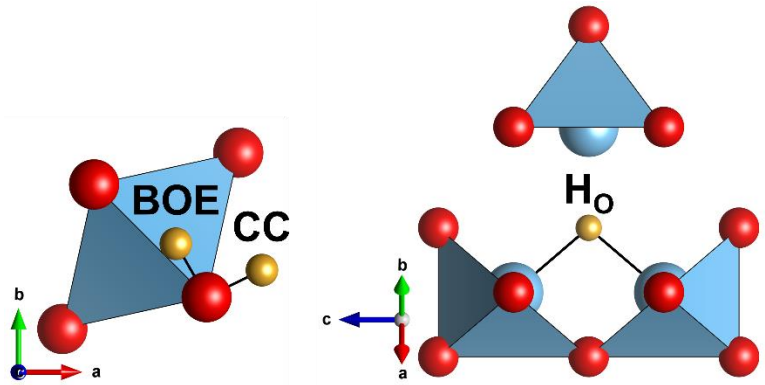

Figure 3.1 *Overview of proposed and observed H locations in rutile. H atoms are represented by bronze spheres, Ti atoms by light blue polyhedra and spheres, and O atoms by red spheres.* ***Left:*** *c-parallel view of a TiO_6 octahedron site in rutile with both possible OH orientations. Our DFT calculations find the channel-centered (CC) position to be strongly preferred. Interpretation of Neutron scattering concluded that the Basal Octahedral Edge (BOE) position is preferred.* ***Right:*** *H in the O vacancy site (H_O), which we find to be preferred over the OH site.*

Previous density functional theory (DFT) studies on rutile have reported some specifics about hydrogen coupling to O vacancies and trivalent dopants such as Al and Fe[4,15–20]. In addition to forming OH, several authors have suggested that hydrogen could occupy the oxygen vacancy site (designated H_O), forming H-Ti bonds[15,17,18]. Calculated OH stretching modes for NAMs[21–24] (including rutile) are commonly presented in DFT studies, providing a means to compare predicted defect structures directly to experimental data. However, we find no such reported data for H_O in rutile, despite its mention in theory literature.

Here, we present the results of a detailed QM investigation of a variety of hydrogen-coupled oxygen vacancy defects in rutile. We place special emphasis on the specifics surrounding defect geometry, hydrogen site preferences, and hydrogen-associated vibrational modes. Additionally, we explore the interaction between interstitial, OH-forming hydrogen (H_i), and hydrogen at the oxygen vacancy site (H_O).

3.2 Main text

The unit cell parameters for rutile were fixed at the experimental values observed by Swope et al. (1995) at 300 K (a = b = 4.592 Å, c = 2.957 Å). We evaluated three defect scenarios:

(i) A single O vacancy, which leads to two electrons in fairly localized orbitals on nearby Ti atoms.

(ii) A single O vacancy coupled to one H, leading to:

(a) a Ti-H_O-Ti bonding environment and an antibonding electron in the d orbitals on these two Ti or

(b) an OH bond with an unpaired spin distributed over Ti atoms near the vacancy.

(iii) A single O vacancy coupled to two H, either Ti-H_O-Ti or OH, with no unpaired spins.

We used a 2×2×2 supercell of rutile containing 16 Ti sites and 32 O sites. This results in H concentrations of ~0.08 wt% to ~0.16 wt%. In a defect-free crystal, the oxygen sites in rutile are symmetrically equivalent, making all possible CC- or BOE-oriented H_i positions degenerate. With an oxygen vacancy and one or two added H atoms, the oxygen sites are no longer equivalent. Therefore, we tested multiple configurations of H_i. In a 2×2×2 cell with an oxygen vacancy, the oxygen atoms can be classified into 14 non-degenerate oxygen sites for protonation. We denote these oxygen sites as A through N. Hydrogen was initially placed in interstitial positions consistent with the neutron scattering results of Swope et al., 1995 (in the BOE OH orientation). This starting orientation was chosen to give the greatest possibility of finding defect structures consistent with existing neutron scattering data. Multiple OH bond orientations were tested in cases

where alternate orientations produced symmetrically distinct configurations, resulting in 21 total unique H_i placements. We distinguish the 21 starting positions for H with a subscript: first the letter designation of the associated O succeeded by a number designation to indicate differing orientation (i.e., H_{D3} and H_{D4} both bond to a D-type oxygen atom but differ in OH bond orientation). All 21 H_i configurations were relaxed for the single hydrogen defects. For defects involving two hydrogen atoms, 21 combinations of H_i sites were selected for relaxation, with an emphasis placed on combinations likely to result in H_O.

Removing one O from TiO_2 exposes the three Ti atoms originally bonded to the O, each of which has five Ti-O bonds. This releases two electrons, leading to two Ti^{3+} centers localized on two of the Ti atoms. We solved for the spin triplet state because it is well described by DFT (singlet pairing of low-overlap orbitals is poorly described with DFT). Based on the projected spin densities, we find that the two unpaired spins are mostly in d_{xy} orbitals on the two Ti atoms closest to the vacancy site and directly adjacent to each other in the *c*-direction. The total spin population is 1.747, with 34% on each of the two neighboring Ti. Most of the remaining spin is delocalized across other Ti pairs aligned with the *c*-axis.

Referencing to the energy of the perfect crystal plus H_2 we find that the energy of TiO_2 with a vacancy structure plus H_2O leads to a formation energy of 2.78 eV. We have compared the energy to H_2 and H_2O because PBE does not describe triplet O_2 well. Since the heat of formation of O in H_2O is -2.5063 eV[25] , the total energy of formation of the O vacancy is 5.29 eV.

Adding H to the O vacancy structure, we expected H to bond to one of the 12 O atoms bonded to the three vacancy-adjacent Ti atoms. These are the sites closest to the O vacancy defect. The final OH bond orientation should be approximately perpendicular to both the c axis and the Ti-O bond, in the CC orientation. Of the two electrons resulting from the removal of O, we expected that one would form a single Ti^{3+} center. Thus, we solved for the doublet state. Figure 3.2 summarizes the final relaxed positions for the nine lowest energy H_i positions and H_O.

We find that there is little energetic preference between protonating O atoms closer to V_O or O atoms further away from V_O. Protonating the H_{K2} site, one of the sites furthest from V_O, produces the lowest energy OH configuration. However, protonating the vacancy adjacent H_{D3} site results in a total energy only 0.02 eV greater than H_{K2}, a relatively minor energetic penalty. Although the systematics determining which OH sites are best is unclear, the total energy differences still show strong preferences in the OH site overall. For instance, the H_{N2} site has a total energy 0.46 eV higher than H_{K2}, making it a highly unlikely H_i site. Additionally, the orientations of OH bonds can affect the total energy significantly. For example, placing hydrogen at H_{D4} (pointing away from V_O) rather than H_{D3} (pointing toward V_O) yields a total energy that is 0.25 eV higher. For the lowest energy OH defects, the hydrogen bonding distances, d(OH···O), range from 2.83 Å to 2.95 Å while the O-H···O angles range from 172.0° to 174.3°.

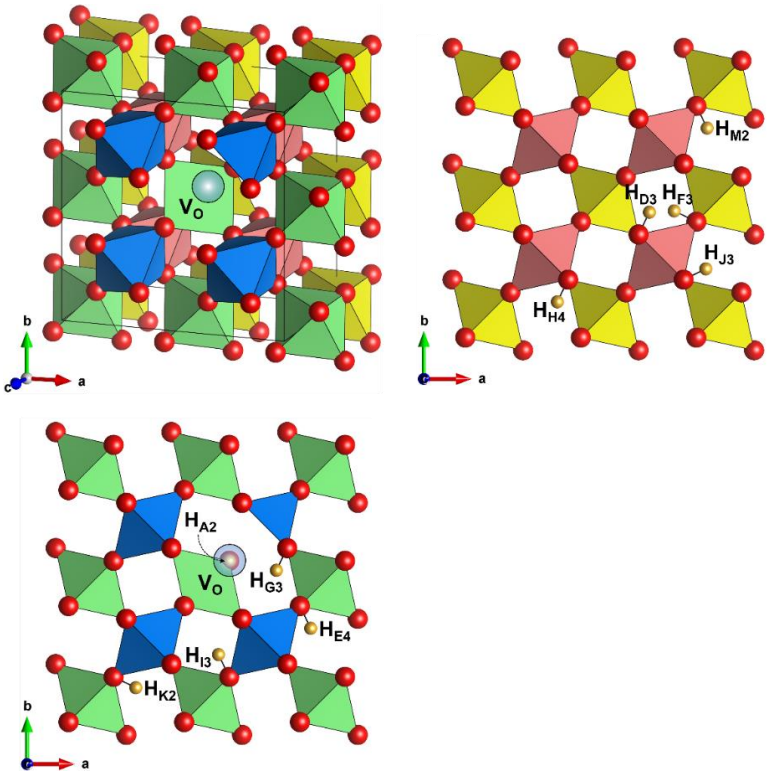

Figure 3.2 *Summary of the O vacancy structure and H positions from fully relaxed structures with one O vacancy and one added H. Octahedral Ti sites are color coded by layer in the c-direction. O atoms are represented by red spheres, H atoms by bronze spheres, and the O vacancy (V_O) by a transparent blue sphere. All OH-bonds are in a channel-centered orientation. Upon structural relaxation, H starting in the A2 position moves to the O vacancy, rather than forming an OH bond. We show only the energetically favorable H positions. There are four layers ordered in the c direction: gold, red, green, and blue in sequence. The O vacancy is in the blue layer.*

Defect site	Final H position	Total energy (eV)	d(OH···O) (Å)
H_{A2}	H_O	-432.066	N/A
H_{K2}	H_i (CC)	-430.647	2.95
H_{D3}	H_i (CC)	-430.629	2.83
H_{M2}	H_i (CC)	-430.623	2.95
H_{E4}	H_i (CC)	-430.577	2.91
H_{G3}	H_i (CC)	-430.550	2.83

Table 3.1 *The energies and hydrogen bonding distances for select defects of the single hydrogen case. "Defect site" refers to the starting position of hydrogen. Ending positions of "H_i" are all CC oriented*

Nonetheless, we find that the most favorable overall location for H does *not* form an OH bond. Rather, H occupies V_O to form H_O, with a total energy 1.42 eV lower than the lowest energy OH-producing configuration. This H_O forms two bonds to two Ti (2.01 Å away), with a third Ti-H distance of 2.10 Å. With H at V_O, the closest oxygen atom to the H is 2.49 Å away.

Before binding the H, the two Ti atoms at 2.01 Å each had an unpaired spin. Bonding them to the H leads to a three-center, two-electron bond combining the H1s orbital with the two d_{xy} orbitals into a symmetric bond pair, denoted $a_1(Ti_{dxy}\text{-}H_s\text{-}Ti_{dxy})$ using the irreducible representation for the C_{2v} symmetry of this bond pair. This leaves a single spin in an antisymmetric antibonding orbital delocalized over the same two Ti, denoted as $b_2(Ti_{dxy}\text{-}Ti_{dxy})$. The electronic transition from $(Ti_{dxy}\text{-}H_s\text{-}Ti_{dxy})$ to $(Ti_{dxy}\text{-}Ti_{dxy})$ should have high intensity. We estimate this to be centered at ~2.07 eV, in the orange region of the visible spectrum. Bader charge analysis predicts a charge of 1.567 on H_O compared to 0.365 for the H_i bonded to O, and an estimated ionic volume of 8.07 $Å^3$ for H_O versus 1.33 $Å^3$ for H_i. The significantly larger volume for H_O is consistent with the measured radius of H^- observed in oxide materials, 1.34±0.02 Å, indicating anionic character for the $a_1(Ti_{dxy}\text{-}Hs\text{-}Ti_{dxy})$ bond[26].

Comparing the perfect crystal plus H_2 versus the H_O defect structure plus H_2O gives a formation energy of 1.70 eV which, when corrected for the H_2O heat of formation of -2.506 eV, leads to a 4.20 eV formation energy. This is 1.09 eV more stable than the O vacancy alone. This indicates that under H_2-rich, reducing conditions, oxygen vacancies are likely to be populated by H_O, rather than remaining empty. Adding a second H to the

O vacancy system leads to an OH bond, with no unpaired spin remaining. Thus, we solved for singlet states. The results of the structural relaxations can be categorized into three groups based on the optimized positions of the two H atoms. From lowest to highest energy, these are: one H_O and one H_i, two H_i, and one H_i and one H_{alt} (H_{alt} is an interstitial position between three Ti atoms that doesn't form OH). We present only the configurations containing H_O and H_i, as the total energies of the other cases are 1.12 to 2.83 eV greater.

Within the group of 16 structures containing both H_O and H_i, the total energies span 0.296 eV from the most to least favorable configurations, but the nine lowest energy configurations differ in energy by 0.076 eV or less. This indicates that while some combinations of H_O and H_i are clearly unfavorable, multiple protonation sites are likely to be simultaneously populated. Among the lower energy configurations, H_i sites further from the O vacancy (H_{M2} and H_{K2}) result in slightly lower total energies than H_i sites close to the vacancy (H_{G3} and H_{D3}), suggesting only minor energetic preferences across a variety of H_i positions. The d(OH···O) values for the OH groups in these nine configurations vary from 2.96 Å to 2.81 Å, while the O-H···O angles show little variation, ranging from 172.8˚ to 174.9˚. Across all combinations of H_O and H_i, Bader charge analyses attribute an average charge of 1.57 to H_O with average Bader volumes of 8.07 $Å^3$, in agreement with the H_O for the single hydrogen case. Referencing to H_2 + TiO_2, the best final state with one H_O and one OH bond plus H_2O is 2.05 eV. Correcting for the heat of formation of H_2O (-2.51 eV) leads to the lowest formation energy for this group of defects, 4.56 eV.

Defect sites	Final H positions	Total energy (eV)	d(OH···O) (Å)	Avg. Ti-H (Å)
H_{A2}, H_{M2}	H_O, H_i	-435.093	2.94	2.04
H_{A2}, H_{E4}	H_O, H_i	-435.085	2.91	2.03
H_{A2}, H_{K2}	H_O, H_i	-435.084	2.96	2.03
H_{A2}, H_{G3}	H_O, H_i	-435.074	2.83	2.04
H_{A2}, H_{D3}	H_O, H_i	-435.070	2.81	2.04

Table 3.2 *The energies and bonding distances for select defects of the two-hydrogen case. "Defect site" refers to the starting position of the hydrogen atoms. Ending positions of "H_i" are all CC oriented. A full summary is included in the supplementary material.*

The frequencies of calculated vibrational modes for defect-free and oxygen-deficient rutile without H do not exceed 820 cm^{-1}. Once H is added, new, higher frequency vibrational modes emerge. For defects containing H_i, the frequencies of these modes are consistent with O-H stretches observed in oxide materials, ranging from 3118 cm^{-1} to 3455 cm^{-1}. Defects containing H_O produce modes with frequencies ranging from 1196 cm^{-1} to 1243 cm^{-1}. These modes arise from Ti-H_O-Ti bonds. Additionally, lower frequency modes associated with both H_O and H_i emerge between 1020 and 1120 cm^{-1} for every H atom added. We attribute these modes to Ti-O vibrations that have been perturbed by hydrogen bonding. A full summary of the H-associated modes in all defects is included in supplementary material and select OH modes are plotted against experimentally observed OH modes in Figure 3.3.

Due to the differences in vibrational modes for Ti-H_O-Ti at ~1200 cm^{-1} and O-H at ~3300 cm^{-1}, zero-point energy effects should be included when discussing the relative energetic preferences of H_O and H_i site occupation. However, after correcting for zero-point energy effects, we find that H_O becomes less stable relative to the most favorable H_i configuration by only ~0.12 eV, a fraction of the overall energy difference of ~1.42 eV between the two cases. Similar zero-point energy corrections also apply between the H_O+H_i and H_i+H_i configurations. Because this correction to the total energy is small relative to the difference in energy between H_O and H_i, we have chosen to ignore zero-point energy corrections.

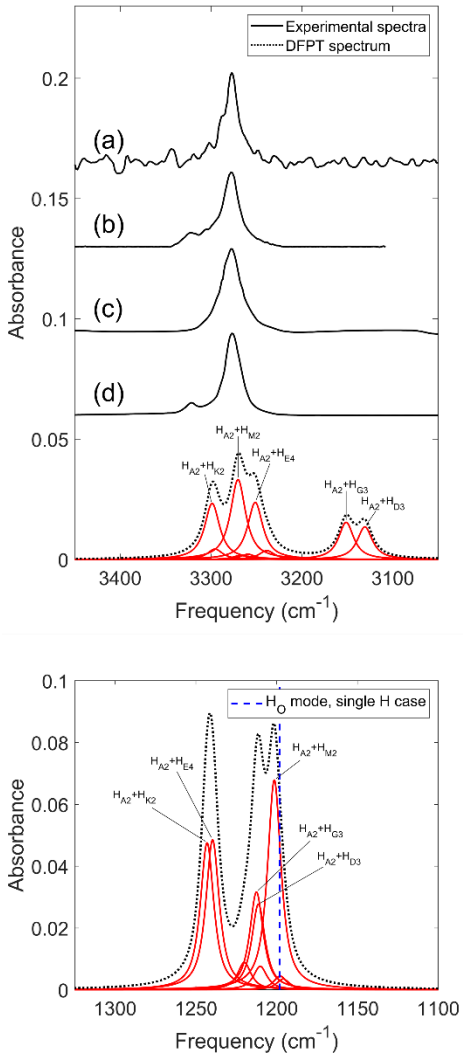

Figure 3.3 *DFT Vibrational modes calculated for OH stretch (top) and Ti-H (bottom) for systems with one O vacancy and two added H atoms. Individual calculated modes (in red) have been assigned arbitrary widths and weighted by the Boltzmann factor calculated at 25 C. Above: DFT-calculated OH modes are compared against OH modes observed in "pure" rutile across a variety of studies*[5,12,27,28]*: (a) Vlassopoulos et al., 1993; (b) Bromiley et al., 2005; (c) Colasanti et al., 2011; (d) Guo, 2017. These experimental spectra demonstrate multiple coexisting OH modes, much like in our calculations. The prominent cluster of DFT modes centered at ~3270 cm*$^{-1}$ *is in good agreement with the experimental data. Below: The modes of the Ti-H*$_O$*-Ti state show two clusters, one at 1240 cm*$^{-1}$ *and one at 1205 cm*$^{-1}$ *depending on which O forms the OH bond. For the case of only one H, the Ti-H*$_O$*-Ti mode is at 1198 cm*$^{-1}$*, which is marked by a vertical dashed blue line. Adding the 2nd H to form an OH bond increases the frequency of the Ti-H*$_O$*-Ti mode. This is because the antibonding unpaired spin delocalized over the same three atoms leads to antibonding character that is removed upon adding a 2nd H to form an OH bond.*

The Ti-H$_O$-Ti bond state - We find that H strongly favors occupying the O vacancy site, leading to a three-center two-electron Ti-H-Ti bond with a vibrational mode near 1200 cm^{-1}. We have searched in vain for studies reporting absorption bands in the 1200 cm^{-1} range. Thus, we recommend testing these predictions experimentally. Currently, experiments measuring the amount of H in rutile assume that it is all in the form of OH groups as measured by intensities near 3300 cm^{-1}. Since this accounts for only half of the H of the 2H case and none of the H for the 1H case, we claim that individual estimates of H present in rutile could be off by a factor of more than two. This may partially account for the wide range in absorbance coefficients reported for rutile[13], and could have implications for assessment of the amount of H dissolved in mantle-derived rutile. Moreover, similar metal-H bonds may form in other oxide phases, especially those with the rutile structure.

Orientation of the OH bonds - Our finding that all OH bonds are channel-center oriented agrees with previous theoretical studies[17,18,20] and some experiments[14]. It is important to note that this bond orientation is not consistent with the interpretation of the neutron scattering results of Swope et al., (1995). They conclude that all OH favor a basal octahedral edge (BOE) orientation, as presented in Figure 3.1. A rationalization of this inconsistency was put forward by Koudriachova et al. (2004), who found that heavy lattice distortion due to the presence of interstitial trivalent species (Al^{3+}) could stabilize alternate OH orientations. Such interstitial defects are demonstrated to become prominent in rutile with high dopant concentrations[29], such as Earth's mantle-derived specimen of Swope et al. (1995). We conclude that the oxygen vacancy complexes from our QM studies do not cause sufficient deformation to produce the BOE orientation.

Energetics of H$_O$ vs Hi - Although our VASP calculations show that H_O has an energy 1.42 eV more stable than H_i, previous thermodynamic calculations following the methods of Zhang and Northup[30] led to the conclusion that H_i has a lower formation energy under virtually all conditions. However, the reported difference in formation energies (0.35 eV) was sufficiently low that H_O and H_i were considered likely to coexist in rutile subjected to reducing conditions[31–33]. Thus, structures containing both H_i and H_O should be considered realistic, even when H_i is considered favorable. The presence of H_O has a pronounced effect

on the incorporation of H_i, as indicated by the broad differences in total energy between the different protonation sites in the single and double hydrogen cases. H_O has been reported to mitigate some of the structural distortion resulting from the oxygen vacancy[15]. Once H_O is present, we find that many other H_i sites may be occupied with little energetic penalty, likely due to the alleviation of distortion by H_O. By contrast, configurations resulting in OH groups, but no H_O, vary more widely in total energy, suggesting more stringent preferences for OH placement. The reduced preference for OH sites when H_O is present results in multiple, comparably probable OH site geometries, with implications for the vibrational spectra.

Correlation of vibrational frequencies with defect structures - Prior experimental work on crystalline oxide solids demonstrates a strong correlation between hydrogen bonding distances and OH stretching frequencies[34]. Our results indicate that different defect structures with only minor differences in total energies can have different hydrogen bonding distances, which should result in numerous OH stretching modes over a range of several hundred wavenumbers. This is especially apparent in the defects containing both H_i and H_O, and is consistent with our calculated stretching modes. Weighting these modes with respect to the total energy of their corresponding structures (in Figure 3.3, we did this by calculating the Boltzmann factor at 25 °C for 2H cases) and combined into a composite spectrum, we find that the most prominent modes tend to form closely spaced clusters. This corresponds well to the experimental spectra, as shown in Fig. 3.3. Comparing our calculated modes directly to experimental spectra, the positions of several prominent modes are in close agreement with the data, while other modes are offset by as much as 150 cm^{-1}.

Observation of the 1200 cm^{-1} mode for the Ti-H_O-Ti state - The Ti-H_O-Ti bond is predicted to have vibrational modes close to ~1200 cm^{-1}, but we find no reports of these modes. Most infrared data reported for H-containing rutile focused on the OH-stretching region, very rarely including spectral components below 2000 cm^{-1}. One of the few exceptions to this is the work of Mo et al. (2015), where the infrared spectra of hydrogen-containing, reduced rutile samples were reported down to 300 cm^{-1}. Although OH stretching modes were clearly absent from the spectra, the expected Ti-H stretching region

contained only ambiguous features. We recommend more extensive experimental study of the 1200 cm^{-1} region. Similar defects and associated infrared-active modes involving H_O-type defects have been predicted in other oxide phases, including ZnO, MgO, SnO_2, and perovskite-type $SrTiO_3$, suggesting a potential abundance of such hydrogen defects in a variety of materials subjected to reduced conditions[31–33].

Observation of the Ti-H_O-Ti vibration in rutile could have broad implications. Prior work addressing hydrogen in NAMs has focused almost exclusively on OH and structurally bound H_2O, with all attention paid to infrared active stretching modes occurring in the vicinity of 3500 cm^{-1} to 3100 cm^{-1} [5,12,27,28]. Thus, H_O is almost universally ignored as a potential hydrogen defect in oxides, especially in the study of geologic materials. This could be a significant oversight, considering that the reducing conditions of earth's interior could provide the optimal environment for incorporation of H_O in a variety of phases. Given the stability of the H_O state, we expect undoped rutile to have at least comparable amounts of H in H_O and OH sites, assuming no single H cases. But including single H cases, the amount of H in undoped rutile could be underestimated by more than a factor of two. The unusually high hydrogen storage capacity of rutile among mantle minerals makes it of particular interest in this regard. The high-pressure SiO_2 polymorph stishovite, being isostructural to rutile, may also contain H_O, with consequences for H sequestration and transport in Earth's mantle. Additionally, special attention should be paid to predictions of H_O in other oxides like MgO and perovskite-type $SrTiO_3$, as these phases are structurally analogous to the most abundant phases of the mantle: periclase and bridgmanite.

METHODS

We used the Vienna Ab initio Simulation Package (VASP, version 5.4.4.18Apr17) for both the structure minimization and phonon calculations. The exchange correlation was described using the Perdew–Burke-Ernzerhof (PBE)[35,36] flavor of the generalized gradient approximation[37–42]. We also included empirical van der Waals corrections using the Becke-Johnson parameters in the Grimme D3 formalism[43,44]. The maximum energy cutoff for the planewave basis set was 500 eV, and all calculations were performed with spin polarization enabled to allow unpaired spin states.

For all calculations, smearing was handled through the tetrahedron method with Blöchl corrections, the recommended technique for wide band gap semiconductors[45]. k-points were sampled using an automatically generated gamma-centered 5x5x8 Monkhorst-Pack mesh for structural minimizations, which was found to be sufficient for our cell size.

The frequencies of the OH and Ti-H stretching modes were calculated via the VASP implementation of density functional perturbation theory (DFPT). Cases selected for DFPT analysis include both the lowest energy defect configurations, and configurations that include notable geometric variations (i.e. unusually long/short hydrogen bonds, atypical H placements, etc.). For these calculations, the k-point density was found to have little effect on predicted band positions, and a lower density 2x2x3 mesh was used. Local charges were assessed using Bader charge analysis[46–49] with VASP and also with SeqQUEST which uses Gaussian basis sets, rather than plane waves.

References

(1) Linsebigler, A. L.; Lu, G.; Yates, J. T. Photocatalysis on TiO_2 Surfaces: Principles, Mechanisms, and Selected Results. *Chem. Rev.* **1995**, *95* (3), 735–758. https://doi.org/10.1021/cr00035a013.

(2) Bak, T.; Nowotny, J.; Rekas, M.; Sorrell, C. C. Defect Chemistry and Semiconducting Properties of Titanium Dioxide: I. Intrinsic Electronic Equilibrium☆. *J. Phys. Chem. Solids* **2003**, *64* (7), 1043–1056. https://doi.org/10.1016/S0022-3697(02)00479-1.

(3) Panayotov, D. A.; Yates, J. T. N-Type Doping of TiO_2 with Atomic Hydrogen-Observation of the Production of Conduction Band Electrons by Infrared Spectroscopy. *Chem. Phys. Lett.* **2007**, *436* (1–3), 204–208. https://doi.org/10.1016/j.cplett.2007.01.039.

(4) Erdal, S.; Kongshaug, C.; Bjørheim, T. S.; Jalarvo, N.; Haugsrud, R.; Norby, T. Hydration of Rutile TiO_2 : Thermodynamics and Effects on *n* - and *p* -Type Electronic Conduction. *J. Phys. Chem. C* **2010**, *114* (19), 9139–9145. https://doi.org/10.1021/jp101886a.

(5) Colasanti, C. V.; Johnson, E. A.; Manning, C. E. An Experimental Study of OH Solubility in Rutile at 500-900 C, 0.5-2 GPa, and a Range of Oxygen Fugacities. *Am. Mineral.* **2011**, *96* (8–9), 1291–1299. https://doi.org/10.2138/am.2011.3708.

(6) Rossman, G. R.; Smyth, J. R. Hydroxyl Contents of Accessory Minerals in Mantle Eclogites and Related Rocks. *American Mineralogist* 75, 765-780.

(7) Bell, D. R.; Rossman, G. R. Water in Earth's Mantle: The Role of Nominally Anhydrous Minerals. *Science* **1992**, *255* (5050), 1391–1397. https://doi.org/10.1126/science.255.5050.1391.
(8) Swope, R. J.; Smyth, J. R.; Larson, A. C. H in Rutile-Type Compounds: I. Single-Crystal Neutron and X-Ray Diffraction Study of H in Rutile. *Am. Mineral.* **1995**, *80* (5–6), 448–453. https://doi.org/10.2138/am-1995-5-604.
(9) Litasov, K. D.; Kagi, H.; Shatskiy, A.; Ohtani, E.; Lakshtanov, D. L.; Bass, J. D.; Ito, E. High Hydrogen Solubility in Al-Rich Stishovite and Water Transport in the Lower Mantle. *Earth Planet. Sci. Lett.* **2007**, *262* (3–4), 620–634. https://doi.org/10.1016/j.epsl.2007.08.015.
(10) Bromiley, G. Solubility of Hydrogen and Ferric Iron in Rutile and TiO_2 (II): Implications for Phase Assemblages during Ultrahigh-Pressure Metamorphism and for the Stability of Silica Polymorphs in the Lower Mantle. *Geophys. Res. Lett.* **2004**, *31* (4), L04610. https://doi.org/10.1029/2004GL019430.
(11) Soffer, B. H. Studies of the Optical and Infrared Absorption Spectra of Rutile Single Crystals. *J. Chem. Phys.* **1961**, *35* (3), 940–945. https://doi.org/10.1063/1.1701242.
(12) Vlassopoulos, D.; Rossman, G. R.; Haggerty, S. Coupled Substitution of H and Minor Elements in Rutile and the Implications of High OH Contents in Nb- and Cr-Rich Rutile from the Upper Mantle. *Am. Mineral.* **1993**, *78* (11–12), 1181–1191.
(13) Maldener, J.; Rauch, F.; Gavranic, M.; Beran, A. OH Absorption Coefficients of Rutile and Cassiterite Deduced from Nuclear Reaction Analysis and FTIR Spectroscopy. *Mineralogy and Petrology* 71(1):21-29
(14) Klauer, S.; Wöhlecke, M. The Incorporation of Hydrogen in TiO_2 Deduced from Polarized Raman Scattering. *Europhys. Lett. EPL* **1992**, *20* (5), 439–443. https://doi.org/10.1209/0295-5075/20/5/010.
(15) Mo, L.-B.; Wang, Y.; Bai, Y.; Xiang, Q.-Y.; Li, Q.; Yao, W.-Q.; Wang, J.-O.; Ibrahim, K.; Wang, H.-H.; Wan, C.-H.; Cao, J.-L. Hydrogen Impurity Defects in Rutile TiO_2. *Sci. Rep.* **2015**, *5* (1), 17634. https://doi.org/10.1038/srep17634.
(16) Koudriachova, M. V.; de Leeuw, S. W.; Harrison, N. M. First-Principles Study of H Intercalation in Rutile TiO_2. *Phys. Rev. B* **2004**, *70* (16), 165421. https://doi.org/10.1103/PhysRevB.70.165421.
(17) Filippone, F.; Mattioli, G.; Alippi, P.; Amore Bonapasta, A. Properties of Hydrogen and Hydrogen–Vacancy Complexes in the Rutile Phase of Titanium Dioxide. *Phys. Rev. B* **2009**, *80* (24), 245203. https://doi.org/10.1103/PhysRevB.80.245203.
(18) Bjørheim, T. S.; Stølen, S.; Norby, T. Ab Initio Studies of Hydrogen and Acceptor Defects in Rutile TiO_2. *Phys. Chem. Chem. Phys.* **2010**, *12* (25), 6817. https://doi.org/10.1039/b925823j.
(19) Bjørheim, T. S.; Kuwabara, A.; Norby, T. Defect Chemistry of Rutile TiO_2 from First Principles Calculations. *J. Phys. Chem. C* **2013**, *117* (11), 5919–5930. https://doi.org/10.1021/jp304146e.
(20) Amore Bonapasta, A.; Filippone, F.; Mattioli, G.; Alippi, P. Oxygen Vacancies and OH Species in Rutile and Anatase TiO_2 Polymorphs. *Catal. Today* **2009**, *144* (1–2), 177–182. https://doi.org/10.1016/j.cattod.2009.01.047.
(21) Bjørheim, T. S.; Kuwabara, A.; Norby, T. Defect Chemistry of Rutile TiO_2 from First Principles Calculations. *J. Phys. Chem. C* **2013**, *117* (11), 5919–5930. https://doi.org/10.1021/jp304146e.

(22) Balan, E.; Yi, H.; Blanchard, M. First-Principles Study of OH Defects in Zircon. *Phys. Chem. Miner.* **2013**, *40* (7), 547–554. https://doi.org/10.1007/s00269-013-0591-7.
(23) Balan, E.; Blanchard, M.; Yi, H.; Ingrin, J. Theoretical Study of OH-Defects in Pure Enstatite. *Phys. Chem. Miner.* **2013**, *40* (1), 41–50. https://doi.org/10.1007/s00269-012-0544-6.
(24) Blanchard, M.; Balan, E.; Wright, K. Incorporation of Water in Iron-Free Ringwoodite: A First-Principles Study. *Am. Mineral.* **2009**, *94* (1), 83–89. https://doi.org/10.2138/am.2009.3020.
(25) M.W., Chase Jr. NIST-JANAF Thermochemical Tables, Fourth Edition. *J Phys Chem Ref Data Monogr. 9* **1998**, 1–1951.
(26) Hayashi, K.; Sushko, P. V.; Hashimoto, Y.; Shluger, A. L.; Hosono, H. Hydride Ions in Oxide Hosts Hidden by Hydroxide Ions. *Nat. Commun.* **2014**, *5* (1), 3515. https://doi.org/10.1038/ncomms4515.
(27) Bromiley, G. D.; Hilairet, N. Hydrogen and Minor Element Incorporation in Synthetic Rutile. *Mineral. Mag.* **2005**, *69* (3), 345–358. https://doi.org/10.1180/0026461056930256.
(28) Guo, H. In-Situ Infrared Spectra of OH in Rutile up to 1000 °C. *Phys. Chem. Miner.* **2017**, *44* (8), 547–552. https://doi.org/10.1007/s00269-017-0881-6.
(29) Stebbins, J. F. Aluminum Substitution in Rutile Titanium Dioxide: New Constraints from High-Resolution ^{27}Al NMR. *Chem. Mater.* **2007**, *19* (7), 1862–1869. https://doi.org/10.1021/cm0629053.
(30) Zhang, S.; Northrup, J. Chemical Potential Dependence of Defect Formation Energies in GaAs: Application to Ga Self-Diffusion. *Phys. Rev. Lett.* **1991**, *67* (17), 2339–2342. https://doi.org/10.1103/PhysRevLett.67.2339.
(31) Janotti, A.; Van de Walle, C. G. Hydrogen Multicentre Bonds. *Nat. Mater.* **2007**, *6* (1), 44–47. https://doi.org/10.1038/nmat1795.
(32) Singh, A. K.; Janotti, A.; Scheffler, M.; Van de Walle, C. G. Sources of Electrical Conductivity in SnO_2. *Phys. Rev. Lett.* **2008**, *101* (5), 055502. https://doi.org/10.1103/PhysRevLett.101.055502.
(33) Varley, J. B.; Janotti, A.; Van de Walle, C. G. Hydrogenated Vacancies and Hidden Hydrogen in $SrTiO_3$. *Phys. Rev. B* **2014**, *89* (7), 075202. https://doi.org/10.1103/PhysRevB.89.075202.
(34) Libowitzky, E. Correlation of O-H Stretching Frequencies and O-H· · ·O Hydrogen Bond Lengths in Minerals. *Monatshefte für Chemie / Chemical Monthly* **1999,** 130, 1047–1059
(35) Perdew, J. P.; Burke, K.; Ernzerhof, M. Generalized Gradient Approximation Made Simple. *Phys. Rev. Lett.* **1996**, *77* (18), 3865–3868. https://doi.org/10.1103/PhysRevLett.77.3865.
(36) Perdew, J. P.; Burke, K.; Ernzerhof, M. Generalized Gradient Approximation Made Simple [Phys. Rev. Lett. 77, 3865 (1996)]. *Phys. Rev. Lett.* **1997**, *78* (7), 1396–1396. https://doi.org/10.1103/PhysRevLett.78.1396.
(37) Kresse, G.; Hafner, J. *Ab Initio* Molecular Dynamics for Liquid Metals. *Phys. Rev. B* **1993**, *47* (1), 558–561. https://doi.org/10.1103/PhysRevB.47.558.
(38) Kresse, G.; Hafner, J. *Ab Initio* Molecular-Dynamics Simulation of the Liquid-Metal–Amorphous-Semiconductor Transition in Germanium. *Phys. Rev. B* **1994**, *49* (20), 14251–14269. https://doi.org/10.1103/PhysRevB.49.14251.

(39) Kresse, G.; Furthmüller, J. Efficiency of Ab-Initio Total Energy Calculations for Metals and Semiconductors Using a Plane-Wave Basis Set. *Comput. Mater. Sci.* **1996**, *6* (1), 15–50. https://doi.org/10.1016/0927-0256(96)00008-0.
(40) Kresse, G.; Furthmüller, J. Efficient Iterative Schemes for *Ab Initio* Total-Energy Calculations Using a Plane-Wave Basis Set. *Phys. Rev. B* **1996**, *54* (16), 11169–11186. https://doi.org/10.1103/PhysRevB.54.11169.
(41) Kresse, G.; Joubert, D. From Ultrasoft Pseudopotentials to the Projector Augmented-Wave Method. *Phys. Rev. B* **1999**, *59* (3), 1758–1775. https://doi.org/10.1103/PhysRevB.59.1758.
(42) Blöchl, P. E. Projector Augmented-Wave Method. *Phys. Rev. B* **1994**, *50* (24), 17953–17979. https://doi.org/10.1103/PhysRevB.50.17953.
(43) Grimme, S.; Antony, J.; Ehrlich, S.; Krieg, H. A Consistent and Accurate *Ab Initio* Parametrization of Density Functional Dispersion Correction (DFT-D) for the 94 Elements H-Pu. *J. Chem. Phys.* **2010**, *132* (15), 154104. https://doi.org/10.1063/1.3382344.
(44) Grimme, S.; Ehrlich, S.; Goerigk, L. Effect of the Damping Function in Dispersion Corrected Density Functional Theory. *J. Comput. Chem.* **2011**, *32* (7), 1456–1465. https://doi.org/10.1002/jcc.21759.
(45) Blöchl, P. E.; Jepsen, O.; Andersen, O. K. Improved Tetrahedron Method for Brillouin-Zone Integrations. *Phys. Rev. B* **1994**, *49* (23), 16223–16233. https://doi.org/10.1103/PhysRevB.49.16223.
(46) Henkelman, G.; Arnaldsson, A.; Jónsson, H. A Fast and Robust Algorithm for Bader Decomposition of Charge Density. *Comput. Mater. Sci.* **2006**, *36* (3), 354–360. https://doi.org/10.1016/j.commatsci.2005.04.010.
(47) Sanville, E.; Kenny, S. D.; Smith, R.; Henkelman, G. Improved Grid-Based Algorithm for Bader Charge Allocation. *J. Comput. Chem.* **2007**, *28* (5), 899–908. https://doi.org/10.1002/jcc.20575.
(48) Tang, W.; Sanville, E.; Henkelman, G. A Grid-Based Bader Analysis Algorithm without Lattice Bias. *J. Phys. Condens. Matter* **2009**, *21* (8), 084204. https://doi.org/10.1088/0953-8984/21/8/084204.
(49) Yu, M.; Trinkle, D. R. Accurate and Efficient Algorithm for Bader Charge Integration. *J. Chem. Phys.* **2011**, *134* (6), 064111. https://doi.org/10.1063/1.3553716.

Chapter 4

THE SEARCH FOR HYDRIDE IN REDUCED RUTILE

The contents of this chapter are part of a manuscript in preparation with the working title "Defect chemistry of H_2-reduced rutile crystals: insights from infrared and ^{1}H NMR spectroscopy" by W.R. Palfey, S.J. Hwang, P.H. Oyala, and G.R. Rossman. In this work, W.R. Palfey carried out the H_2 treatments, prepared samples for FTIR, carried out FTIR meaurements, and performed EPR under the supervision of P.H. Oyala. S.J. Hwang carried out the ^{1}H NMR measurements. W.R. Palfey and G.R. Rossman were involved in designing the study, and all authors were involved in preparing the manuscript.

4.1 Introduction

This chapter documents our efforts to experimentally detect the H_O (hydride) state in rutile that was predicted by DFT in the prior chapter. To review, those calculations predicted an overwhelming preference for hydrogen to occupy the oxygen vacancy (v_O) site. The implication is that under synthesis conditions that are reduced enough, where oxygen is sufficiently mobile to form vacancy states, and where reduced (i.e., not H^+) hydrogen is available, H_O should form. As a first instinct, the easiest way to meet these requirements would be to treat crystals of rutile in a furnace with a hydrogen (H_2) atmosphere. Indeed, as was mentioned in Chapter 3, prior authors have carried out such experiments with the explicit purpose of inducing the H_O state[1]. However, while it is true that Mo et al., (2015) did record conductivities consistent with hydride incorporation, they did not make a direct and unambiguous observation of H_O through a method like neutron scattering, ^{1}H nuclear magnetic resonance (NMR), or Fourier transform infrared spectroscopy (FTIR), which would be desired. Additionally, these measurements (especially FTIR) lend themselves better to geologic materials than measurements of conductivity. Additional work to measure the H_O state by these methods in TiO_2 treated under controlled conditions will serve as a reference for future studies on natural, geologically derived samples.

The work presented here makes a concerted effort to directly record the H_O state in reduced synthetic rutile (if it is truly present). Key to this work is high-quality FTIR measurements combined with the complimentary methods of ^{1}H NMR and electron paramagnetic resonance (EPR) that can probe rutile's defect chemistry. While we ultimately did not detect H_O, we have been able to characterize reduced rutile's other competing defect states with high certainty.

4.2 Methods

We sourced single crystal samples from a Verneuil (flame fusion) grown boule of synthetic rutile, loaned from the Gemological Institute of America (GIA). Slices from the boule were aligned optically, and wafers were sliced with a *c*-parallel orientation using a diamond wafering blade. This orientation allows for spectroscopy to be performed with the wave vector in both principal directions: parallel and perpendicular to the optic axis. These wafers were variable in thickness, on the order of 0.5 to 1.0 mm thick, 7 to 10 mm long, and about 3 mm wide.

Sample treatments were carried out in a Lindbergh Sola Basic tube furnace under pure flowing H_2 gas. The gas itself was flowed through a 1.2 m long, 4 mm ID fused silica tube (the smaller diameter of this tube reduces the volume of H_2 gas actually in the furnace at a given time) and purged into a fume hood. A flow rate of about 0.5 cm^3/s was used. Ar gas was also put on the line to purge air from the treatment tube before H_2 annealing, and to purge H_2 from the treatment tube after annealing had completed. Through testing, we found that the results of our treatments could be significantly influenced by apparent contamination of the H_2 or Ar gas flows by water vapor. Ultimately, this was accounted for by adding a Cu tubing condensing coil filled with Al pellets into the gas line. Before each synthesis run, this coil was purged with Ar and heated to drive off water. During the sample treatment, the coil was immersed in a large dewar of dry ice to freeze out any water contamination. We took additional steps to avoid water and hydroxyl contamination from the samples and the inner furnace tube surfaces as well. The day before a sample treatment,

the gas line was continuously purged with Ar while the sample was left inserted in the center of the furnace at 900 °C overnight (typically about 15 hours). This was done to not only remove adsorbed water on the tube and sample surfaces, but also to remove the majority of structural hydroxyl contained in the untreated rutile crystals. The internal tube was made much longer than the furnace's outer tube to allow for quick sample insertion and quenching. Samples were placed in the internal tube such that pushing the tube into the furnace would place the sample in the furnace's center, while pulling the tube would remove the sample from the furnace completely, allowing it to cool to room temperature either after treatment, or preceding treatment while the furnace was adjusted to its final temperature. The H_2 anneals were carried out for 6 hours at temperatures of 500, 550, 600, 650, 700, 750, 800, and 900 °C.

After treatment, samples were sliced into two pieces using a wire saw. One slice was ground into course granules for measurement via ^{1}H NMR and EPR, while the other slice was doubly polished for measurement by FTIR. To achieve transmission below 1500 cm^{-1}, samples had to be thinned to 145 to 50 μm, depending upon the treatment conditions (more reduced samples become more absorbing in the infrared). Final surfaces were achieved using 1 and 0.25 μm diamond abrasive-charged felt pads. This preparation was possible for all samples with the exception of the 900 °C annealed sample, which was too brittle, fractured, and absorbing to make into a thin wafer. In light of the possibility for diffusion gradients in the crystals, one of the polished sides was prepared by removing as little material as possible. This preparation was unavoidable for most samples, as high temperature treatments produce a film of opaque reaction products on the crystal surfaces. Nevertheless, we acknowledge that this is a potential source of error for the transmission FTIR measurements.

^{1}H MAS NMR spectra were collected using a Bruker DSX-500 spectrometer and a Bruker 4 mm MAS probe. Samples were packed into 4 mm zirconia rotor and spun at 12000 Hz. A 4 microsecond (μs) 90 degree rf pulse at an operating frequency of 500.21 MHz was applied to record free induction decay with a recycle delay time of 10 second. Note that longer delay time (50 s) was tested for ruling out the presence of any slowly relaxing ^{1}H signal. Signal averaging was done for 64 scans unless otherwise noted. The ^{1}H

background signal was recorded the same way, and the subtracted signal is reported. The ^{1}H chemical shift was externally calibrated to tetramethylsilane (TMS) while Tetrakis-(trimethylsilyl)silane (TKTMS) was used as the second reference.

X-band Continuous-wave (CW) EPR spectra were obtained using a Bruker EMX spectrometer equipped with an ER4119 High-Q resonator, using Xenon acquisition software. Cryogenic temperatures at 77 K were achieved using a quartz finger dewar filled with liquid nitrogen. Samples were contained in 1.6 mm O.D. quartz capillaries, which were inserted into standard 4.0 mm O.D. quartz EPR tubes. Spectra were collected at a microwave (MW) frequency of 9.39-9.43 GHz, using MW power of 2.2 mW, field modulation amplitude of 1 Gauss, and conversion time of 5 ms.

Transmission FTIR spectra were collected using a Thermo-Nicolet iS50 FTIR spectrometer equipped with a KBr beamsplitter and MCTA liquid nitrogen cooled detector. Due to high absorptivity in the infrared region caused by electronic features resulting from rutile's reduction (discussed more in our results), spectra were collected at liquid nitrogen temperature (77 K). At lower temperatures, the electronic features either shift or become narrower, reducing absorbance in the IR region. These 77 K spectra were collected through the use of a custom made, continuously evacuating sample dewar with KBr windows. A gold nanowire polarizer was used to collect spectra with both *c*-perpendicular and *c*-parallel polarizations.

4.3 Results and Discussion

4.3.1 General effects of the H_2 treatment

Consistent with prior studies on reduced rutile[2–4] , reduction of our samples by H_2 gas changed their color from the nearly colorless/pale yellow of untreated rutile to blue (Figure 4.1). This was true for every treatment condition that we tested. For samples annealed at lower temperatures, samples were much paler, while samples annealed at higher temperatures became virtually or (in the case of the 900 °C sample) entirely opaque. This change in color is easily explained as intervalence charge transfer (IVCT) between adjacent Ti^{4+} and Ti^{3+} states. Ti^{3+} is formed either through the formation of v_O, OH^-, or H_O

defects, which all require reduced Ti ions for charge balance. Ti-Ti IVCT results in a blue color in other oxide materials[5], just like we observe in rutile.

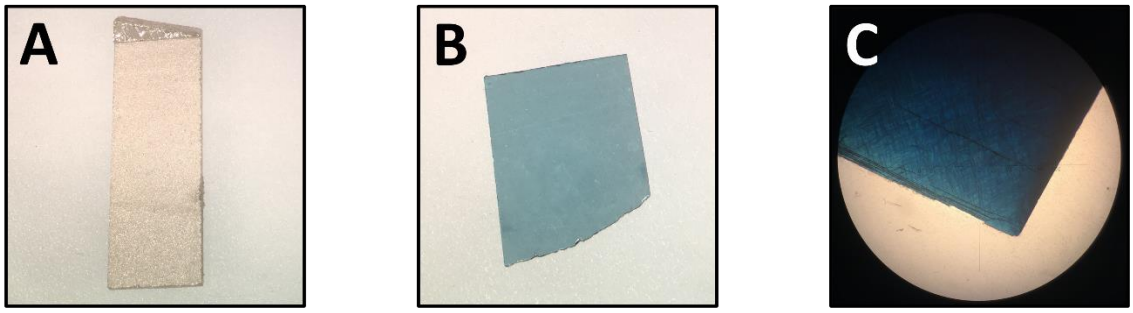

Figure 4.1 *Images of rutile samples. (A) Untreated wafer sliced from the boule. (B) Thinned and polished rutile wafer after H_2 treatment. (C) Rutile wafer treated with H_2 at 800 °C, as viewed under the microscope. Note the cross-hatched pattern and crack formation.*

The textures of the samples treated between 500 and 750 °C did not vary from untreated rutile, but the 800 and 900 °C annealed samples showed significant changes. At 800 °C, we found that rutile develops a cross-hatched texture of darker and lighter blue regions. Cracks were also commonly formed approximately perpendicular to the *c*-direction. Importantly, an untreated crystal of rutile can be brought to the same temperature as this sample (800 °C) and quenched to room temperature without similar cracks forming, demonstrating that rapid quenching does not inherently cause samples to partially or completely shatter. This regular cross-hatching suggests that the observed features are regularly aligning themselves relative to the crystal lattice. We interpret these as the formation of regions with differing oxygen deficiency, where the darker blue regions are more deficient in oxygen than their lighter blue counterparts. This difference in color, along with the formation of the cracks, and the regular orientations of both, strongly suggests the partial conversion of rutile into Magnéli phases (Ti oxides with sub stoichiometry of O)[6]. The formation of Magnéli phases tends to cause shearing due to a lattice mismatch, which could explain the observed cracks[7]. If this is the case, then the 800 °C treated material should be dominated by v_O defects, accounting for high oxygen loss. The 900 °C treated sample represents the advancement of this process, as the sample material is fully shattered and completely opaque from the prevalence of IVCT.

4.3.2 ^{1}H NMR

Our ^{1}H NMR results show the presence of only a single structural hydrogen state for all samples, as indicated by the presence of a single resolvable feature. The shifts are all in the range of 7.25 to 7.55 ppm, which is typical for structural OH^-. Referring to previously defined relations between δ and d(O···O), these NMR shifts should correspond to a d(O···O) of ~2.8 Å[8,9]. The steady change in peak positions across the temperature range of 500 to 750 °C would seem to imply a systematic change of this bond length, but the calculated difference across the 0.3 ppm range only amounts to about 0.015 Å. Nonetheless, this still does seem to imply a progressive structural change, which could possibly be related to distortion from accumulations of defects like v_O.

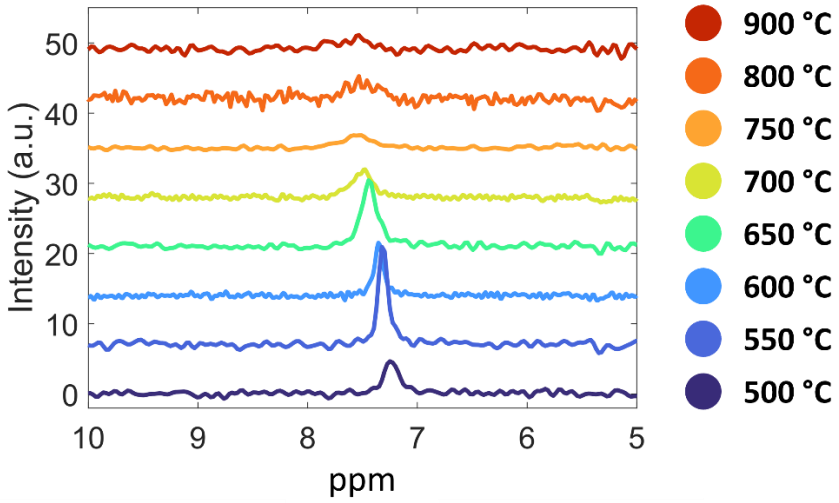

Figure 4.2 *^{1}H NMR spectra of the full sample suite, normalized to sample mass. At 500 °C, a single peak is located at 7.25 ppm. With progressive treatment to 750 °C, this peak migrates to higher ppm shifts while first becoming sharper, then eventually becoming low and broad, centering around 7.55 ppm. Above 750 °C, the peaks are very broad and don't systematically shift anymore. No other hydrogen-related signals can be detected.*

Although positive shifts could also theoretically correspond to H^- in some types of materials[10–12], this has not been demonstrated for H^- ions bonded to transition metals like Ti. More likely, H_O would produce a broad, negatively shifted feature, as has been observed for hydride incorporation in the (Ca,Sr,Ba)TiO_3 perovskite family[13]. The nature of these

negative shifts (which are discussed in more detail in later chapters) are thought to come about from the electrons involved in the Ti-H bond also contributing to the conduction band[14,15]. The increases in delocalized electrons typically associated with reduced rutile[2], suggests strongly that the ^{1}H NMR signal of H_O could be similar. Nevertheless, because the exact nature of the Ti-H bond in rutile has not been documented, it cannot be known for certain whether or not H_O would have an associated negatively or positively shifted ^{1}H NMR signal. Additionally, even if the 7.25 – 7.55 ppm features are OH^- rather than hydride, it is still possible that an undetectable (to ^{1}H NMR) amount of hydride could still be in the samples (NMR tends to be less sensitive than FTIR to hydrogen). Thus, analysis of the samples via FTIR will serve as necessary compliment to these data.

4.3.3 Transmission FTIR

As was detailed in Chapter 3, all of the detectable hydrogen related infrared modes in rutile should be polarized primarily perpendicular to the *c*-axis. This includes the O-H stretch, which has been extremely well-documented in the past[16,3,4,17], the Ti-O-H bending mode, which has not yet been experimentally observed, and the Ti-H-Ti stretching mode, the primary signature for hydride. Our 77 K spectra are presented in Figure 4.3. For both polarization directions, there is an extremely broad and intense feature centered off-spectrum in the near infrared region that is superimposed over all other features. This feature is more strongly polarized in the c-parallel direction. Given its width, this feature must be an electronic absorption, likely resulting from the presence of reduced titanium. Khomenko et al. (1998) had previously identified this absorption with identical polarization behavior in crystals of reduced rutile[2].

Sharp O-H stretching modes centered at 3286.5 cm^{-1} are immediately apparent in the c-perpendicular polarized spectra, clearly indicating the presence of OH^-. There is some variation in the mode positions across the samples, but this is within a range of about 1-2 cm^{-1} and is not systematic with treatment temperature. At 500 and 550 °C, there is a secondary stretching mode located at about 3330 cm^{-1} that is completely absent from the other spectra. The O-H stretching mode is most intense in samples treated between 550 and 650 °C, which is generally consistent with the strength of their corresponding ^{1}H NMR

signals. At 800 °C, the O-H stretch is weakened significantly, and the mode becomes much less sharp, also consistent with the ^{1}H NMR data.

Although both the spectra c-parallel and c-perpendicular polarized spectra contain numerous features between 1000 and 1300 cm^{-1}, we attribute none of these to hydride. The infrared spectrum for rutile is poorly characterized in this region, so there are no assignments for these modes. Through our own measurements, we were able to determine that these numerous low wavenumber vibrational modes are all present in untreated rutile, meaning that these are likely overtones and combinations of much more intense bands related to native Ti-O vibrations. However, there is one feature that is related to hydrogen in this region. In spectra with c-perpendicular polarization, a relatively weak mode emerges at 1065 cm^{-1} that appears to scale with the O-H stretching mode. We attribute this to the Ti-O-H bending mode. The observed position of this band is in good agreement with its DFT-predicted position from Chapter 3.

The clear presence of OH^{-} in the form of both a prominent O-H stretching mode and a predictably less intense Ti-O-H bending mode, combined with the singular positively shifted ^{1}H NMR feature leads us to make the judgement that no hydride is detectable in our sample material. Instead, we believe that the major defects present are limited to OH^{-} and v_O. Changes in the low wavenumber modes of the 800 °C may be indicative of structural changes taking place in the sample as a result of oxygen loss. The 1265 cm^{-1} c-parallel polarized mode and the 1180 and 1120 cm^{-1} c-perpendicular polarized modes become noticeably weaker in the 800 °C spectrum when compared to the other treatment temperatures. This could correspond to the acceleration of oxygen loss to form Magnéli phases, as was mentioned previously. EPR, which is sensitive to the density of Ti^{3+}, can be used to further investigate the aspects of defect chemistry that are independent of hydrogen.

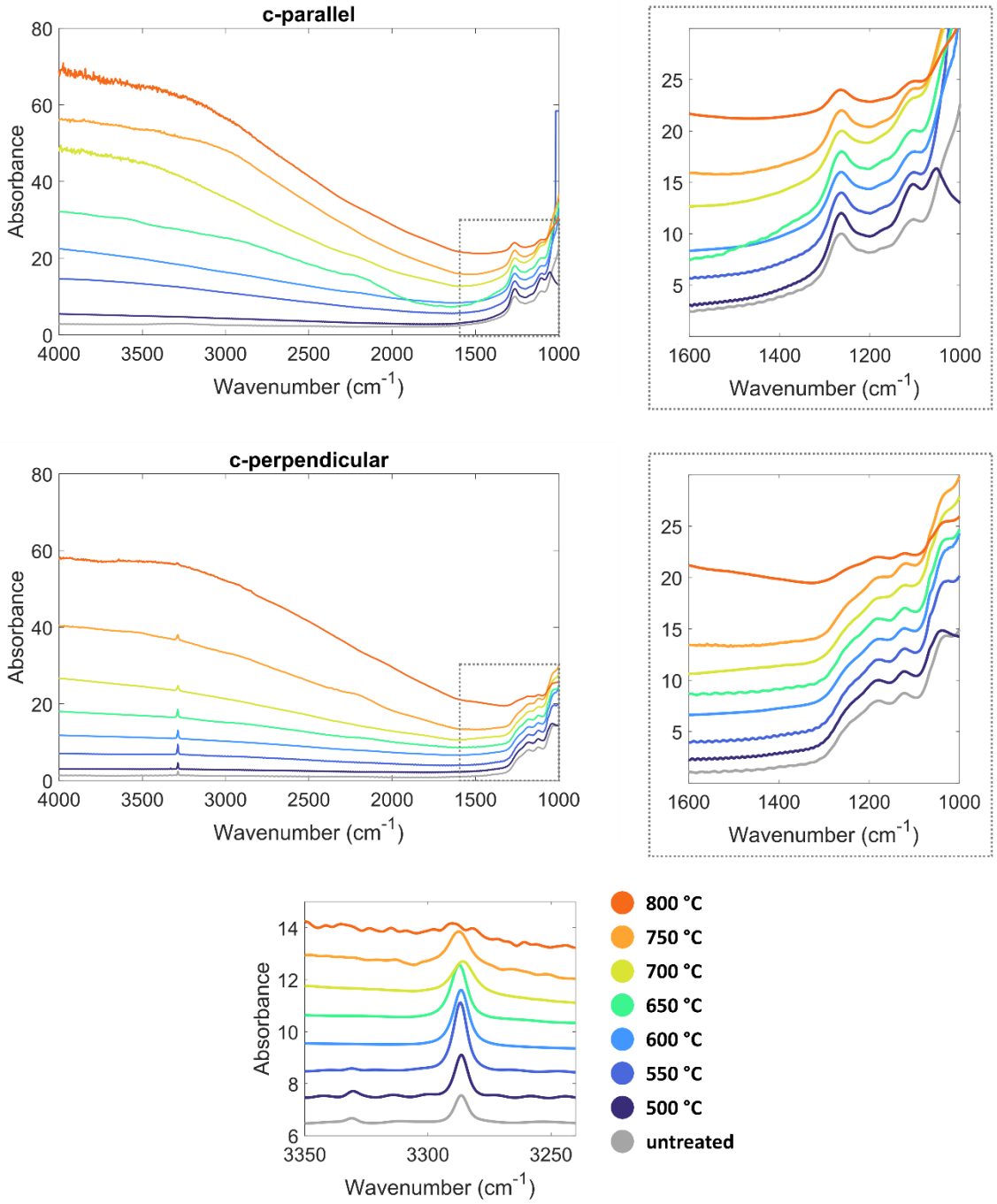

Figure 4.3 *The transmission FTIR data, normalized to pathlength in mm. Note that for all plots presented, spectra have been vertically offset for clarity. Spectra for the full continuum from 500 to 800 °C are presented. For the c-parallel polarization direction For both the c-parallel (top) and c-perpendicular (middle) polarizations, the high absorbance electronic feature is artificially truncated beyond about 3500 cm^{-1} in the samples subjected to the most intense treatments. In the zoomed-in plot of the low wavenumber region of the c-perpendicular polarization, the Ti-O-H bending mode is present at 1065 cm^{-1}. The O-H stretch (bottom) is oriented virtually perpendicular to c, with no component in the c-parallel spectrum.*

4.3.4 EPR

Across all samples, the EPR spectra have a line shape consistent with a spin ½ species (Ti^{3+}), as expected (Figure 4.4). The intensities of the signals scale with the temperatures of the treatments, indicating that Ti^{3+} centers, which could be coupled to either OH^- or v_O, become more abundant at higher temperatures. This is consistent with the increased intensity of the IR-observed electronic absorption and the deepening of the blue color across the treatment regime. At two stages along the temperature series, there are apparent points of divergence in EPR behavior. This occurs most dramatically between the 750 °C and 800 °C treated samples. The 800 °C signal has an intensity about an order of magnitude greater than 750 °C, and the 900 °C signal is still another order of magnitude greater than 800 °C. Similarly, but perhaps less dramatically, there appears to be a similar divide between the 550 °C and 600 °C treatments.

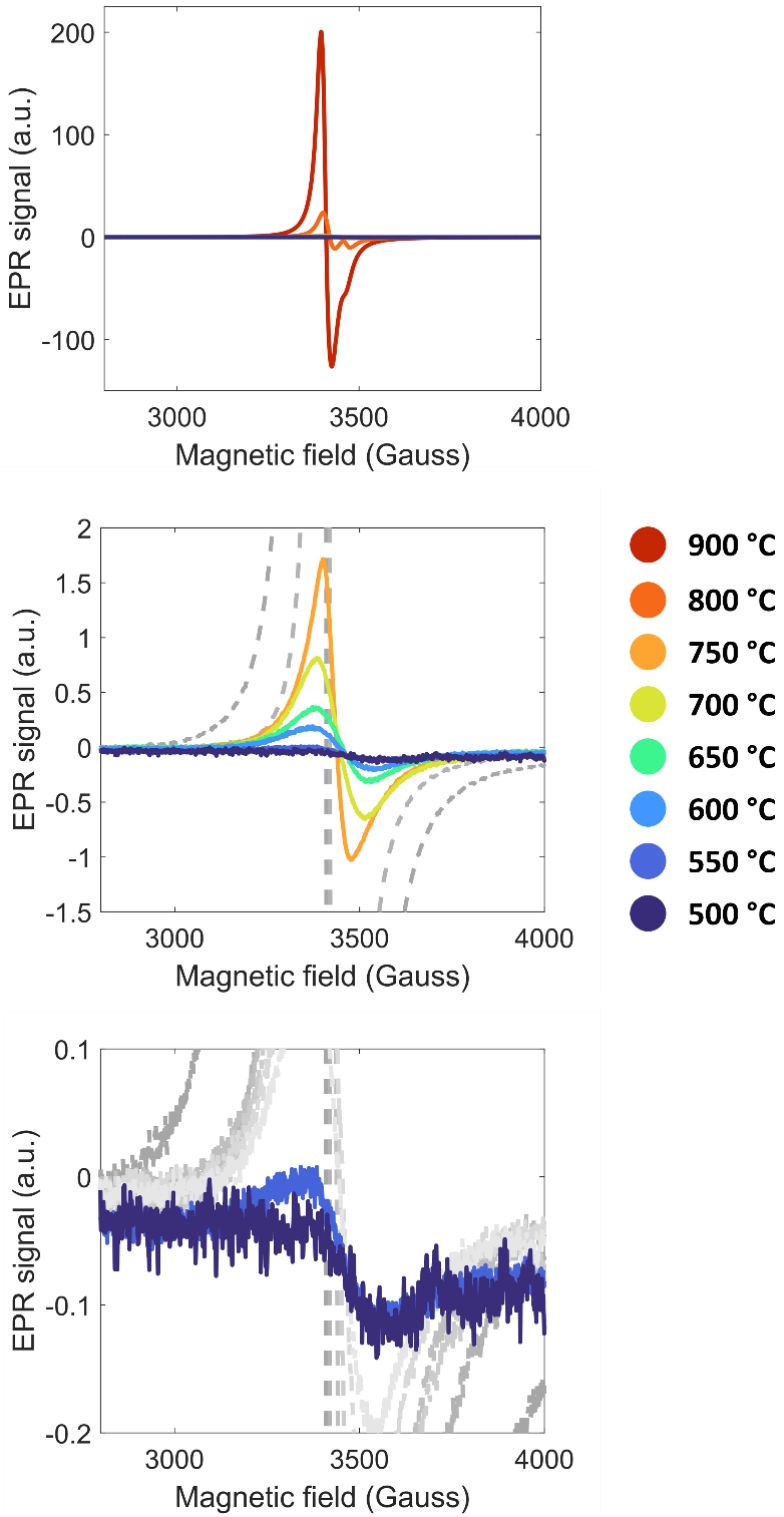

Figure 4.4 *EPR spectra of the entire sample series, shown at three different scales. Across all samples, the shape of the signal is consistent with a spin ½ species. For the 900 and 800 °C samples (top), a second feature emerges in the higher field, suggesting the emergence of a unique* Ti^{3+} *site.*

With the added context of prior observations, ^{1}H NMR, and FTIR, the reasons for these divisions in the EPR data become clear. The NMR data indicate that, although the concentrations of OH^- do differ across the entire sample suite, these differences do not constitute order of magnitude changes in signal. This means that OH^- alone cannot explain jumps in Ti^{3+}concentration. Examination of the OH^- modes observed via FTIR led to the same conclusion. Thus, these differences must be due to oxygen loss.

We interpret the initial jump in signal intensity between 550 and 600 °C as a transition between OH^- and v_O as preferred defect states. At 550 °C, OH^- formation is favorable; this temperature condition produces strong NMR and FTIR signals. Transmission through the sample is also quite high, indicating lower amounts of IVCT. The EPR signal for this sample is also relatively weak. Therefore, it is probably safe to assume that a large portion (perhaps even a majority) of Ti^{3+} centers couple to OH^- and OH^- is a dominant defect state. At 600 °C, the OH^- signal intensities from ^{1}H NMR and FTIR are still comparable to 550°C. Despite this, the EPR signal intensity increases by a factor of 4. Thus, this divergence indicates the emergence of v_O as a dominant defect state. At higher temperatures, the disparity between v_O and OH^- grows, as recorded by the increasing EPR intensity and decreasing hydroxyl-related features.

Between 750 °C and 800 °C, a much more dramatic change occurs. Based on the disparity between the ^{1}H NMR and EPR spectra, it is clear that there is a marked increase in oxygen loss from the sample. However, the emergence of an additional peak also indicates the development of high quantities of structurally unique Ti^{3+} sites. At 900 °C, both features are still present, illustrative of a continuing structural transition facilitated by the loss of oxygen. We interpret these two high temperature stages as recording the phase transition between rutile and Magnéli phases. The extreme increase in EPR signal represents a change from defect-level concentrations of Ti^{3+} in rutile, to fully stoichiometric concentrations of Ti^{3+} found in Magnéli phases. At 800 °C, there is still a coexistence of rutile and Magnéli phases (hence the still-present but weakened FTIR signals for rutile). At 900 °C, it is likely that the sample has been fully converted to either one or a mixture of mixed valence Ti oxides.

4.3.5 Commentary on treatment conditions

Our results would seem to contradict the DFT-made predictions from the prior chapter. Nevertheless, it is important to keep in mind that the results of these experiments only suggest that the H_O defect cannot be induced in rutile under these specific conditions. Our results vary even from those of Mo et al. (2015), whose experiments appear quite similar to ours on the surface [1]. However, there were key differences. Chief among these is that our H_2 treatments operated under a continuous gas flow, while Mo et al. used a static H_2 atmosphere. This means that the reaction products of our treatments (H_2O in the case of v_O and H_O defects) are constantly purged, whereas these products could accumulate and attain equilibrium in a closed reaction vessel. Additionally, the experiments of Mo et al. began with a sealed ampule containing 0.95 atm of H_2, meaning that the pressure of H_2 was higher than in our experiments. These differences are decidedly capable of making a difference in the resulting defect chemistry of the samples; our materials all incorporated hydroxyl, while FTIR of the static atmosphere experiment materials showed no evidence for hydroxyl [1]. More detailed studies of static H_2 treated samples are a logical next step for hydride analysis in rutile.

There are still other possible pathways that could be attempted for hydride incorporation in rutile. Numerous types of hydride salts and metal hydrides, including CaH_2, LiH, and TiH_2 have been used to induce hydride defect states in a variety of oxide phases[11,13,18]. However, for all the successes these hydride treatments have had in producing oxyhydrides, reactions between hydrides and oxides can just as often result in oxygen vacancies without hydride incorporation[19]. Virtually every oxyhydride phase contains a highly electropositive cation like the group I and II elements. While the ability for Ti in TiO_2 to reduce from Ti^{4+} to Ti^{3+} provides a pathway for charge compensation and TiO_2's ability to form v_O could accommodate H_O, the lack of another ion that "holds on" tighter to O may result in TiO_2 decomposing from O^{2-} loss before H_O is incorporated. Indeed, the most commonly employed hydride salt for making oxyhydrides, CaH_2, is industrially used to reduce TiO_2 to Ti metal. It may be possible to tune experimental parameters to avoid this, but hydride incorporation in TiO_2 clearly presents more of a challenge than some other phases. Overall, it appears that while theory predicts an

extremely high stability for the H_O defect, the experimental pathway to inducing H_O could be difficult to find.

4.4 Summary

We treated single crystals of synthetic rutile under H_2 gas across a wide temperature range to assess whether hydride (H_O) is incorporated. Through a thorough analysis using ^{1}H NMR, FTIR, and EPR, we find no evidence that hydride is incorporated under these treatment conditions. Rather, we observed OH^- groups as the only hydrogen defect. Through our detailed measurements, we were able to estimate regimes of OH^- versus v_O stability, observe the transition from rutile to sub-oxide Magnéli phases, and record the Ti-O-H bending mode in rutile for the first time. Although these results do not rule out the possibility for hydride incorporation in rutile, they do emphasize the need for experiments to clarify computational results. The overwhelming stability of H_O predicted via DFT in the prior chapter could be interpreted as evidence that the H_O state should be straightforward to induce experimentally, but this was not found to be the case. Infrared measurements of hydride in oxides, which could be a crucial consideration for the deep earth hydrogen cycle, will likely progress in other materials and minerals before results are achieved in TiO_2.

References

(1) Mo, L.-B.; Wang, Y.; Bai, Y.; Xiang, Q.-Y.; Li, Q.; Yao, W.-Q.; Wang, J.-O.; Ibrahim, K.; Wang, H.-H.; Wan, C.-H.; Cao, J.-L. Hydrogen Impurity Defects in Rutile TiO2. *Sci Rep* **2015**, *5* (1), 17634. https://doi.org/10.1038/srep17634.

(2) Khomenko, V. M.; Langer, K.; Rager, H.; Fett, A. Electronic Absorption by Ti 3+ Ions and Electron Delocalization in Synthetic Blue Rutile. *Physics and Chemistry of Minerals* **1998**, *25* (5), 338–346. https://doi.org/10.1007/s002690050124.

(3) Bromiley, G. D.; Hilairet, N. Hydrogen and Minor Element Incorporation in Synthetic Rutile. *Mineral. mag.* **2005**, *69* (3), 345–358. https://doi.org/10.1180/0026461056930256.

(4) Colasanti, C. V.; Johnson, E. A.; Manning, C. E. An Experimental Study of OH Solubility in Rutile at 500-900 C, 0.5-2 GPa, and a Range of Oxygen Fugacities.

American Mineralogist **2011**, *96* (8–9), 1291–1299. https://doi.org/10.2138/am.2011.3708.

(5) Doyle, P. M.; Schofield, P. F.; Berry, A. J.; Walker, A. M.; Knight, K. S. Substitution of Ti^{3+} and Ti^{4+} in Hibonite (CaAl12O19). *American Mineralogist* **2014**, *99* (7), 1369–1382. https://doi.org/10.2138/am.2014.4532.

(6) Andersson, S.; Collén, B.; Kuylenstierna, U.; Magnéli, A.; Magnéli, A.; Pestmalis, H.; Åsbrink, S. Phase Analysis Studies on the Titanium-Oxygen System. *Acta Chem. Scand.* **1957**, *11*, 1641–1652. https://doi.org/10.3891/acta.chem.scand.11-1641.

(7) Zhang, Q.; Liu, W.; Zhou, Y.; Li, J.; Sun, T.; Liu, Q.; Ma, Y.; Wang, J.; Li, J.; Zhao, R.; Sui, Y.; Matsumoto, T.; Muroyama, N.; Yamano, A.; Harris, K. D. M.; Shen, Z. J.; Terasaki, O. Andersson-Magnéli Phases Ti_nO_{2n-1} : Recent Progress Inspired by Swedish Scientists. *Zeitschrift anorg allge chemie* **2021**, *647* (2–3), 126–133. https://doi.org/10.1002/zaac.202000408.

(8) Berglund, B.; Vaughan, R. W. Correlations between Proton Chemical Shift Tensors, Deuterium Quadrupole Couplings, and Bond Distances for Hydrogen Bonds in Solids. *The Journal of Chemical Physics* **1980**, *73* (5), 2037–2043. https://doi.org/10.1063/1.440423.

(9) Eckert, H.; Yesinowski, J. P.; Silver, L. A.; Stolper, E. M. Water in Silicate Glasses: Quantitation and Structural Studies by Proton Solid Echo and Magic Angle Spinning NMR Methods. *J. Phys. Chem.* **1988**, *92* (7), 2055–2064. https://doi.org/10.1021/j100318a070.

(10) Hayashi, K.; Sushko, P. V.; Hashimoto, Y.; Shluger, A. L.; Hosono, H. Hydride Ions in Oxide Hosts Hidden by Hydroxide Ions. *Nat Commun* **2014**, *5* (1), 3515. https://doi.org/10.1038/ncomms4515.

(11) Hayashi, K.; Hosono, H. Green Apatites: Hydride Ions, Electrons and Their Interconversion in the Crystallographic Channel. *Phys. Chem. Chem. Phys.* **2016**, *18* (11), 8186–8195. https://doi.org/10.1039/C6CP00515B.

(12) Alexander Mutschke; Thomas Wylezich; Clemens Ritter; Antti J. Karttunen; Nathalie Kunkel. An Unprecedented Fully H- -Substituted Phosphate Hydride $Sr_5(PO_4)_3H$ Expanding the Apatite Family. *European Journal of Inorganic Chemistry* **2019**, *48*, 5073–5076. https://doi.org/10.1002/ejic.201901151.

(13) Kobayashi, Y.; Hernandez, O. J.; Sakaguchi, T.; Yajima, T.; Roisnel, T.; Tsujimoto, Y.; Morita, M.; Noda, Y.; Mogami, Y.; Kitada, A.; Ohkura, M.; Hosokawa, S.; Li, Z.; Hayashi, K.; Kusano, Y.; Kim, J. eun; Tsuji, N.; Fujiwara, A.; Matsushita, Y.; Yoshimura, K.; Takegoshi, K.; Inoue, M.; Takano, M.; Kageyama, H. An Oxyhydride of $BaTiO_3$ Exhibiting Hydride Exchange and Electronic Conductivity. *Nature Mater* **2012**, *11* (6), 507–511. https://doi.org/10.1038/nmat3302.

(14) Misaki, T.; Oikawa, I.; Takamura, H. Negative Knight Shift in Ba-Ti Oxyhydride: An Indication of the Multiple Hydrogen Occupation. *Chem. Mater.* **2019**, *31* (18), 7178–7185. https://doi.org/10.1021/acs.chemmater.9b01434.

(15) Aleksis, R.; Nedumkandathil, R.; Papawassiliou, W.; Carvalho, J. P.; Jaworski, A.; Häussermann, U.; Pell, A. J. Probing the Electronic Structure and Hydride Occupancy in Barium Titanium Oxyhydride through DFT-Assisted Solid-State NMR. *Phys. Chem. Chem. Phys.* **2022**, *24* (46), 28164–28173. https://doi.org/10.1039/D2CP04675J.

(16) Vlassopoulos, D.; Rossman, G. R.; Haggerty, S. Coupled Substitution of H and Minor Elements in Rutile and the Implications of High OH Contents in Nb- and Cr-Rich Rutile from the Upper Mantle. *American Mineralogist* **1993**, *78* (11–12), 1181–1191.
(17) Guo, H. In-Situ Infrared Spectra of OH in Rutile up to 1000 °C. *Phys Chem Minerals* **2017**, *44* (8), 547–552. https://doi.org/10.1007/s00269-017-0881-6.
(18) Guo, H.; Jaworski, A.; Ma, Z.; Slabon, A.; Bacsik, Z.; Nedumkandathil, R.; Häussermann, U. Trapping of Different Stages of $BaTiO_3$ Reduction with LiH. *RSC Adv.* **2020**, *10* (58), 35356–35365. https://doi.org/10.1039/D0RA07276A.
(19) Yamamoto, T.; Kageyama, H. Hydride Reductions of Transition Metal Oxides. *Chemistry Letters* **2013**, *42* (9), 946–953. https://doi.org/10.1246/cl.130581.

Chapter 5

THE SPECTROSCOPY OF HYDRIDE IN SINGLE CRYSTALS OF $SrTiO_3$

The contents of this chapter are part of a manuscript in preparation titled "The spectroscopy of hydride in single crystals of $SrTiO_3$" by W.R. Palfey, S.J. Hwang, W.A. Goddard III, and G.R. Rossman. In this work, W.R. Palfey carried out sample treatments and preparations, and made infrared, visible light, and Raman spectroscopic measurements. Calculations were also carried out by W.R. Palfey under the supervision of W.A. Goddard III. S.J. Hwang performed the ^1H NMR measurements. W.R. Palfey and G.R. Rossman were involved in designing the work and all authors helped prepare the manuscript.

5.1 Introduction

The defect chemistry of oxygen deficient $SrTiO_3$ perovskite is complex and incompletely understood. In particular, the behavior of hydride ions (H^-), which are known to occupy oxygen vacancies (V_O) in $SrTiO_3$ and other Ti perovskites, has been an active topic of discussion[1–6]. The hydride ion and associated V_O defects are shown to induce interesting material properties, including color changes, transitions to metallic conductivity, and switchable persistent photoconductivity[2,6]. Titanate perovskites in the $(Ca,Sr,Ba)TiO_3$ family have demonstrated an exceptional ability to incorporate high concentrations of hydride, reaching stochiometric "oxyhydride" compositions[1]. These oxyhydride materials not only have their own unique properties, but can also serve as precursors to produce novel mixed anionic materials, like oxynitrides[7]. High hydride compositions are commonly achieved in titanate perovskites through reactions with hydride salts (usually CaH_2, but also MgH_2, $NaAlH_4$, $NaBH_4$ and LiH)[8,9] . For example, the reaction between $SrTiO_3$ and CaH_2 can be expressed as:

$$4SrTiO_3 + 3CaH_2 \rightarrow 4SrTiO_2H + Ca(OH)_2 + 2CaO \qquad \textbf{(1)}$$

Through this reaction, O^{2-} is replaced directly by H^- and charge balance is achieved through Ti reduction:

$$Ti_{Ti}^{\times} + O_O^{\times} \rightarrow Ti_{Ti}^{/} + H_O^{\cdot} \qquad \textbf{(2)}$$

This reaction is now well-documented in $CaTiO_3$, $SrTiO_3$ and $BaTiO_3$, with the most extensive characterization carried out via ^1H NMR[2–4,6,8]. Through this Ti^{4+} reduction mechanism, up to 20% of all O^{2-} ions may be replaced by H^- [2]. Although the O^{2-}-H^- exchange has been firmly established for the titanate family of perovskites, many uncertainties remain surrounding the precise nature of hydride's bonding environment, occupation of the V_O site (either one or two H^- ions could be stable at V_O), and the interplay between coexisting V_O and H^- defects. Furthermore, a limited number of techniques have been utilized to directly characterize H^- in titanate perovskites outside of ^1H NMR and neutron scattering. Complimentary analytical techniques, especially those capable of providing insight into hydrogen speciation, may be necessary for further elucidating hydride's behavior in $SrTiO_3$ and other oxyhydrides.

In studies of crystalline, oxide materials, Fourier transform infrared (FTIR) spectroscopy has demonstrated exceptional utility for observing and characterizing structural hydrogen. For many scenarios, such as in-situ high-pressure experiments, cases of small or limited sample material, low H concentrations, or samples with NMR-incompatible compositions (e.g, high Fe content), infrared represents one of the few viable methods for describing hydrogen speciation. However, with very few exceptions, these measurements tend to focus on the oxidized forms of hydrogen, namely OH^- groups. OH^- is typically easy to observe, with strongly infrared-active stretching modes typically occurring in the range of 3600 – 3000 cm^{-1} where few other features reside. In contrast to this, using FTIR to observe hydride is much less straightforward. While hydride has been observed via infrared spectroscopy in a handful of instances[10,11], much remains unknown about the infrared behavior of H^-. In oxides, H^- modes are most likely to occur in a much lower energy region (below 1500 cm^{-1}) where many other high-intensity modes are typically present. The precise locations of these H^- modes are not intuitively known, mainly due to the many possible coordination geometries of H^- and bonded species. Thus, careful predictions about hydride's IR behavior, likely via *ab-initio* methods, are key for making FTIR viable for H^- detection.

In addition to relevance to novel materials development, the large capacity for hydride incorporation in perovskites could be of interest to the earth science community. Perovskite-structured minerals represent the most abundant materials found in Earth's mantle and the chemistry and related properties of these materials has direct consequences for planetary-scale processes. Despite the high solubility of H^- in the perovskite structure, hydride has yet to be evaluated in considerations of mantle dynamics and the overall planetary hydrogen budget. Some studies show that certain perovskite oxyhydrides can be stabilized by elevated pressures[12], possibly pointing to favorable H^- incorporation in planetary interiors, but these effects have not been studied extensively. Additionally, the stability of FeH_x phases at lower mantle conditions[13] could provide a potential source of reduced hydrogen for hydride to react with silicate perovskites. Thus, studies of hydride in perovskite phases, including titanate analogues to earth-abundant minerals, could represent important steps toward contextualizing hydride's importance in deep planetary interiors.

Here, we present our characterization of hydride-doped single crystals of $SrTiO_3$, a material that serves as a good test case for characterizing hydride in oxides. We detail our method to dope single crystals of $SrTiO_3$ with H^-. We find that not only can single crystals of $SrTiO_3$ be easily doped with H^-, but the range of temperatures over which this reaction can be carried out is larger than previously reported for reactions with powdered materials. We also present FTIR and UV-vis spectroscopy of hydride-bearing $SrTiO_3$ samples, documenting the effect hydride has on $SrTiO_3$ color and potentially documenting H^- in a perovskite via FTIR for the first time. We then compare these results to density functional theory (DFT) calculations to assess the accuracy of theory for predicting the behavior of H^-. These results could have implications in studies of the deep earth, as vibrational spectroscopy may be the only viable method for measuring hydride in perovskite phases.

5.2 Methods

5.2.1 Experimental - Synthesis

Two different methods were used to prepare $SrTiO_3$ samples for hydride doping via reaction with CaH_2. For the first round of synthesis, $SrTiO_3$ crystals were pressed into

pellets of CaH_2 powder to ensure close surface contact and facilitate ion exchange. Singly polished, 0.5 x 10 x 10 mm crystal substrates of $SrTiO_3$ from MSE Supplies® (>99.9% purity, (100) orientation) were sliced into roughly 2.5 x 2.5 mm squares using a wire saw. These crystal slices were dried overnight in a 150° C desiccator oven to ensure no H_2O surface contamination. All subsequent sample preparation then took place in an Ar glovebox to further avoid contamination. A granular CaH_2 powder purchased from Thermo Scientific Chemicals (98% metal basis purity) was ground in an alumina mortar and pestle for 15 minutes in preparation for pressing into pellets. Crystal slices were immersed in the finely ground CaH_2 powder in a 7 mm pellet die and pressed to 1.5 tons using a Specac hydraulic press. A molar excess of CaH_2 (~165 mg) was used for each pellet. Two pellets each were placed into 9 mm fused silica tubes, which were then evacuated to 0.01 Pa and sealed using a gas-oxygen torch at a total tube length of ~30 cm.

Sample tubes were placed directly into a tube furnace heated to the final reaction temperature (600, 700, or 800 °C). All tubes being treated at the same temperature were placed into the furnace at the same time, and two tubes were designated for each treatment time in the sample series (four pellets per temperature-time condition). At the end of a synthesis run, sample tubes were removed from the furnace and plunged directly into liquid nitrogen. The crystals were recovered by dissolving the CaH_2 pellets in a mixture of isopropyl alcohol and deionized water (~3:1 ratio). The recovered crystals were sonicated in deionized water to remove unwanted reaction products from their surfaces.

Because these pelletized samples were deformed, cracked or shattered either upon recovery or during preparation, a second round of syntheses was carried out to produce samples suitable for transmission spectroscopy (i.e., FTIR and UV-vis). In this round of synthesis, the $SrTiO_3$ substrates were sliced into ~3.3 x 10 mm slices using a wire saw. A secondary 4 mm ID fused silica tube ~5 cm long was packed with CaH_2 powder, and the $SrTiO_3$ crystal slices were immersed in the powder. These secondary tubes were then placed into the bottoms of longer 9 mm tubes and sealed in the same manner as the pelletized samples. The procedure for treatment in the furnace was identical to the pelletized samples, except the tubes were allowed to cool to room temperature in air, rather

than plunged in liquid nitrogen. One sample (SC-70048h) was treated in this manner through two separate 24-hour steps.

Samples from the second round of synthesis were thinned and polished in preparation for transmission spectroscopic methods. Due to the high absorptivity of the samples in the infrared range (which is discussed in more detail in our results), samples needed to be made very thin. For sample SC-6006h, which was less absorbing, this was accomplished through hand polishing using felt pads charged with diamond abrasives (final polish of 0.25 μm). For samples SC-70024h, SC-70036h, and SC-70048h, which needed to be thinned below 20 μm, a dimple grinder (Fischione brand, model M2000, usually used to prepare materials for transmission electron microscopy) was used. Samples were first thinned between 150 and 80 μm, before the dimple grinder was used to bring them to their final thicknesses. During this process, the factory polished side of the crystal was left intact. Final dimpled surfaces were achieved with a 3 μm diamond suspension.

Some of the samples treated in the above manner were also subjected to additional treatments for more advanced spectroscopic study. A portion of SC-70048h was vacuum annealed in stages and analyzed between each stage. These consisted of two 500 °C, 3.5 hour steps, and a final 600 °C, 3.5 hour step. A 2 mPa continuous vacuum was pulled on the samples during these treatments. Additionally, two portions of a sample prepared identically to SC-70024h were annealed under H_2 and D_2 flow, to investigate the H/D exchange. These treatments lasted for 6 hours and were carried out in a tube furnace heated to 400 °C, in a process modeled after prior treatments carried on $BaTiO_3$ powders[2]. Both the vacuum annealed and H_2/D_2 annealed samples were polished and dimpled in the manner outlined above.

Sample	Treatment Conditions
CaH_2 Series	
SC-6006h	Reacted with CaH_2 for 6 hours at 600 °C
SC-70024h	Reacted with CaH_2 for 24 hours at 700 °C
SC-70036h	Reacted with CaH_2 for 36 hours at 700 °C
SC-70048h	Reacted with CaH_2 in two stages for 24 hours at 700 °C
Vacuum Series	
Vac1	Same as SC-70024h, then vacuum annealed 3.5 hours at 500 °C
Vac2	Vac1 vacuum annealed additional 3.5 hours at 500 °C
Vac3	Vac2 vacuum annealed additional 3.5 hours at 600 °C
H_2 / D_2 Series	
H2-70024h	SC-70048h annealed under flowing H_2 at 400 °C for 6 hours
D2-70024h	SC-70048h annealed under flowing D_2 at 400 °C for 6 hours

Table 5.1 *– Overview of the treatment conditions for samples that were measured via transmission spectroscopy.*

5.2.2 Experimental - Analytical

Raman spectroscopy was carried out using a Renishaw inVia Raman microscope equipped with a 514 nm green laser. Static scans were carried out centered at 1100 cm^{-1}, for a spectral range of 100 to 2000 cm^{-1}. Laser powers ranging from 0.5% to 5% were used to assess the effect on the sample spectra. Spectra were taken on the manufacturer-polished sides of the samples.

^1H magic angle spinning (MAS) NMR spectra were collected using a Bruker DSX-500 spectrometer and a Bruker 4 mm MAS probe. Samples were diluted with fused quartz powder using a mortar and a pestle and packed into 4 mm zirconia rotor and spun at 12000 Hz. The dilution was performed inside of an Ar-filled glovebox of which water level is maintained to be less than a few ppm. This was found to be necessary for samples containing higher concentrations of hydride. A 4 microsecond (μs) 90 degree radiofrequency (rf) pulse at an operating frequency of 500.21 MHz was applied to record free induction decay with a recycle delay time of 10 second. Note that longer delay time (50 s) was tested for ruling out the presence of any slowly relaxing ^1H signal. Signal

averaging was done for 64 scans unless otherwise noted. The ^{1}H background signal was recorded the same way, and the subtracted signal is reported. The ^{1}H chemical shift was externally calibrated to tetramethylsilane (TMS) while Tetrakis-(trimethylsilyl)silane (TKTMS) was used as the second reference.

Infrared spectroscopy was carried out using a Thermo-Nicolet iS50 FTIR spectrometer equipped with a KBr beamsplitter and MCTA liquid nitrogen cooled detector. Attenuated total reflectance (ATR) was found to be insufficient for these materials (either due to high sample absorptivity, high refractive indices, low H concentrations or a combination of the three), so transmission spectroscopy was used instead. Both white and IR light sources were used to probe an extended range (7500 to 2500 cm^{-1} and 5500 to 650 cm^{-1} for each source, respectively). For highly absorbing samples, the maximum number of accumulations allowed by the instrument per measurement was reached (60000 scans). Liquid nitrogen temperature spectra (which would normally be preferable for resolving peaks) could not be collected, as the windows of our low-temperature apparatus increased reflection loss, frequently truncating features in the critically important high-absorbance, low frequency spectral range.

Optical absorbance spectra covering the visible and near infrared range were collected on a custom made 1024 element silicon diode array spectrometer with a tungsten-halogen light source. By using switching between two different detectors, spectra over the range of 380 to 1700 nm (about 26300 to 5900 cm^{-1}) could be collected. These results were combined with the FTIR spectra, to produce continuous spectra with an extremely extended range.

5.2.3 Theory

DFT calculations were used to predict the likely structural states of hydrogen in $SrTiO_3$ and predict these states' corresponding infrared behavior. All calculations were all carried out using the Vienna Ab Initio Simulation Package (VASP, ver 6.2.1 16May21). The Perdew-Burke-Ernerhof (PBE) generalized gradient approximation functional was utilized for approximating the exchange correlation, in conjunction with the D3 corrections

of Grimme et al[14–19]. For total energies, smearing near the Fermi level was done through the tetrahedron method with Blöchl corrections[20] and the cutoff energy for the planewave basis set was fixed to 500 eV. Structural minimizations were converged to an interatomic force of 0.1 eV/Å. Due to the likelihood of unpaired valence electrons resulting from Ti^{3+} states, we conducted spin polarized calculations for all methods described below. The unit cell parameters for all calculations were fixed to a commonly observed experimental value of a=3.905 Å, and supercell sizes of 2×2×2, 3×2×2, 3×3×2 and 3×3×3 were tested. k-points were generated using an automatically generated Γ-centered grid and optimal k-point densities were converged for each supercell size.

For all supercell sizes, only a single O site was considered for H^- occupation. Given the supercell sizes tested, the effective compositions tested were $Sr_8Ti_8O_{23}H_1$, $Sr_{12}Ti_{12}O_{35}H_1$, $Sr_{18}Ti_{18}O_{53}H_1$, and $Sr_{27}Ti_{27}O_{80}H_1$, effectively spanning a range of hydride concentrations. Multiple positions and configurations of H^- were considered due to the possibility of off-site occupation (a possibility raised by Misaki et al. (2019) in the $BaTiO_3$ perovskite system[3]). We considered instances where H^- resides directly at the O^{2-} lattice site, and adjacent positions biased in the direction of two Sr atoms, biased toward one Ti site along the Ti-H-Ti bonds, and biased toward two Sr atoms and one Ti atom (Figure 5.1).

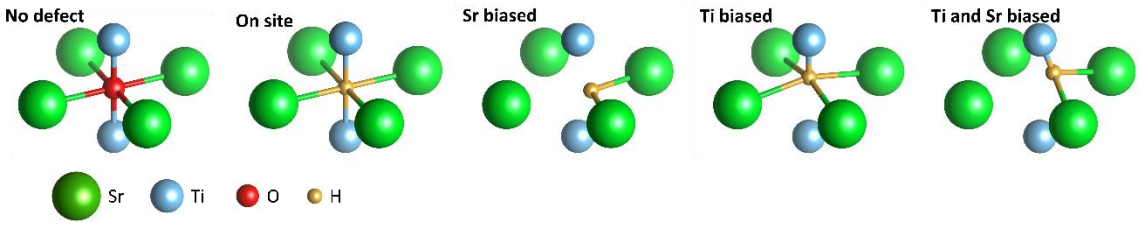

Figure 5.1 *– The possible occupations of hydride tested via DFT. Of these four, only the direct on-site occupation was found to be stable in all supercell sizes. The Sr-biased, off-site occupation was found to be stable only in the 2x2x2 supercell, where it was favored by 25 meV.*

The infrared behavior of hydride was predicted through two methods: density functional perturbation theory (DFPT, a 0 K method) and analysis of trajectories from

quantum mechanics molecular dynamics (QM-MD) simulations. DFPT calculations were carried out so that the Born effective charges were simultaneously calculated, which in conjunction with the Hessian produced from DFPT, allows for the calculation of predicted infrared activities (a code developed by David Karhanek was used to accomplish this in post-processing[21]). Due to practical limitations of computational cost, the largest supercell this was carried out on was 3×2×2. The QM-MD simulation was carried out using a canonical (NVT) ensemble with a temperature fixed to 300 K (approximately equivalent to measurement conditions) and a Nose-Hoover thermostat. The total simulation time was 20 ps, with 1 fs timesteps (20,000 frames). Due to limitations of computational cost, QM-MD simulations were carried out on a 2×2×2 supercell and a single Γ-centered k-point. We found it necessary to fix the smearing width at 0.1 eV to allow for reasonably fast electronic convergence at each simulation step. A vibrational density of states was produced from the trajectories by taking the Fourier transform of the velocity autocorrelation function (VACF), as implemented in the 2PT code[22–24].

5.3 Results and Discussion

5.3.1 DFT Calculations

Our calculations revealed that the bonding geometry of the hydride ion is likely simple, with few structural possibilities. Tests of different occupations of the oxygen vacancy site by hydride predicted that multiple hydride bonding environments are only stable in the smallest supercell (2×2×2). Of the four cases tested, only two were stable in the 2×2×2 cell: the direct occupation of the O lattice site by hydride, and an offsite occupation favoring biased bonding toward two adjacent Sr atoms (approximately equivalent to the "Sr-biased" structure in Figure 5. 1). The latter is favorable by 25 meV in the smallest cell, implying it is likely the dominant defect state. For all supercells 3×2×2 or larger, only the on-site occupation by H^- was found to be stable. These results suggest that the bonding environment of H could differ depending on its concentration. Nevertheless, as we discuss in more detail below, the concentration regime for H^- in our samples is not likely to reach the threshold necessary for this multisite occupation. Thus, we mainly consider the defect case stable across all supercell sizes, the on-site occupation.

The 0 K phonon calculations (which include both DFPT and finite differences) predict three vibrational modes for the H^- ion: a Ti-H-Ti stretching mode centered approximately at 1300 cm^{-1}, and two degenerate bending modes located close to 820 cm^{-1}. From our DFPT results, the stretching mode is predicted to be strongly infrared active, while the bending modes should only be modestly infrared active. The vibrational density of states produced from the molecular dynamics simulation carried out at 300 K shows a distribution of modes largely consistent with the DFPT mode positions. Isolation of the H-dominant vibrational density shows a distribution of modes between 1200 and 1400 cm^{-1}, with the highest density peak centered at ~1282 cm^{-1}. This high-density portion of the distribution implies a prominent line shape for the Ti-H-Ti stretching mode, which should make detection possible.

These DFT results imply that detection of H^- via FTIR may prove difficult. First, the predicted position of the Ti-H-Ti stretch overlaps very closely with a native feature of the $SrTiO_3$ spectrum centered at 1326 cm^{-1}. Depending on the true position of the stretching mode, hydride's presence may only be apparent upon performing spectral subtractions to remove the 1326 cm^{-1} mode. An additional and more challenging obstacle to overcome is the high infrared absorbance of reduced $SrTiO_3$. As prior authors have noted, spectra of O-deficient $SrTiO_3$ crystals tend to contain a broad, intense feature centered in the infrared (~2200 cm^{-1})[25,26]. The shape of this feature implies an origin from electronic absorption. Because of the extreme breadth of this electronic feature, regions below 2200 cm^{-1}, including the region likely to contain the Ti-H-Ti stretch, may be inaccessible for measurement. Earlier studies have remarked on this analytical challenge as a barrier to H^- detection via FTIR[5]. These factors also make detection of the bending hydride modes even less likely, as they are in a region of still higher absorbance and have lower predicted infrared activities.

Calculation	Ti-H-Ti stretch position (cm^{-1})
Finite differences, 2×2×2 cell	1307.7
Finite differences, 3×2×2 cell	1301.0
Finite differences, 3×3×2 cell	1304.7
Finite differences, 3×3×3 cell	1342.1
Perturbation theory, 3×3×2 cell	1327.5

Table 5.2 *– Summary of mode positions predicted by 0 K methods.*

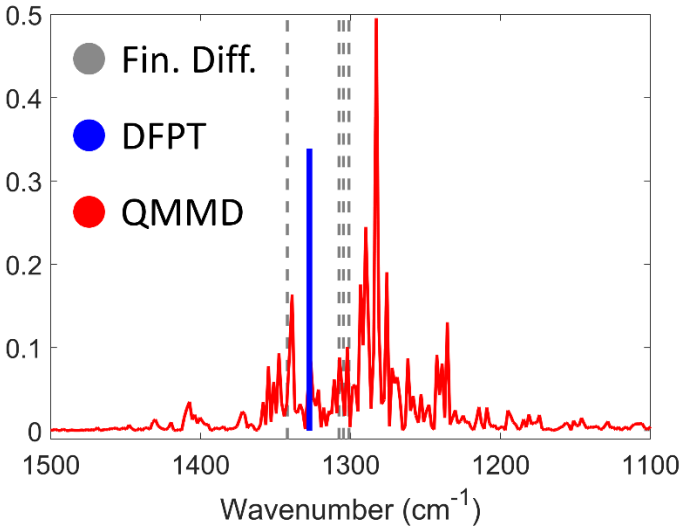

Figure 5.2 *– Summary of the predicted vibrational modes associated with H^- in hydride via finite differences, DFPT and QM-MD, across a range of supercell sizes. For 0 K methods, the plotted positions are from Table 5.2. In all cases, the Ti-H-Ti stretching mode is the feature most likely to be detected. It should be positioned approximately in the vicinity of 1300 cm^{-1}.*

5.3.2 Experimental – the pellet samples

The samples prepared via the pressed pellet method served as the baseline for assessing the ^{1}H NMR behavior of hydride in single crystal $SrTiO_3$. For all treatment conditions, the resulting crystals were extremely dark blue, becoming more intensely colored with increased temperatures and reaction times. These types of color changes are commonly associated with H^- incorporation in $BaTiO_3$ [2] and have been described for reduced $SrTiO_3$ [27]. Our ^{1}H NMR results across the 600 °C, 700 °C and 800 °C series are

presented in Figure 5.3. For all treatment times in the 600 °C and 700 °C series, we find that ^{1}H NMR does not convincingly detect any features that can be attributed to structural incorporation of H^-. Rather, we attribute the signals that are present to either surface OH^- contamination (the sharp features around 1 ppm) or artifacts of background subtraction. The latter of these effects is especially present in initial attempted measurements that were not diluted with quartz glass powder, for which background subtraction proved challenging. Despite this, we did observe the clear presence of structural H^- in the samples heated at 800 °C for all three treatment times. The positions and shapes of these features, which are broad and negatively shifted, are consistent with H^- signals reported for other titanate perovskites[2–4,9]. Additionally, these features shift to increasingly negative positions with increased treatment time, which is consistent with increased H^- (and possibly v_O) content[3,4].

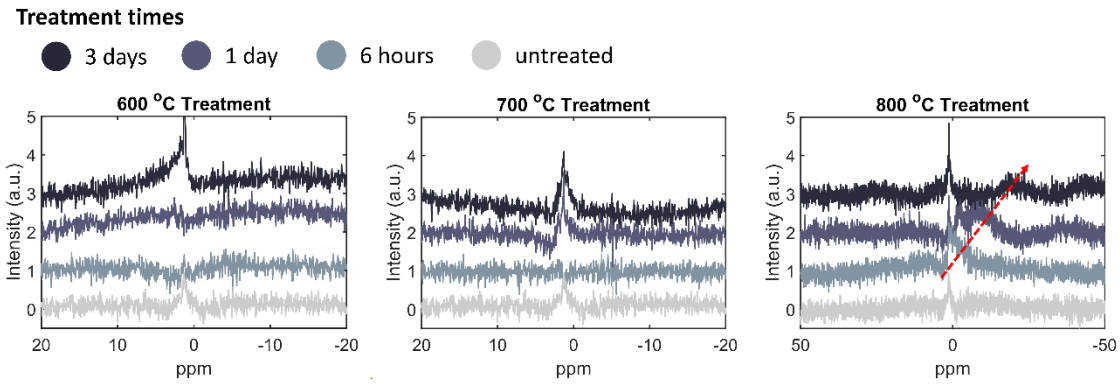

Figure 5.3 *– ^{1}H MAS NMR spectra from the initial run of pellet-prepared samples, plotted against the spectrum from untreated $SrTiO_3$. All samples were mixed with fused quartz powder. For syntheses carried out at 600 and 700 °C, there is no discernable signal associated with structural H^-, but rather sharp features located near 1 ppm that are likely due to adsorbed water. The samples treated at 800 °C also contain these features, but also have the broad, negative shifted peaks associated with hydride (note the extended data range compared to the other two plots). Progressive treatment increases the magnitude of the negative shift, as indicated by the red arrow. For the samples treated for 1 day, multiple features might be present, possibly due to the fact that these samples consist of 4 separate crystals that may vary slightly in hydride content.*

At first glance, these results would seem to suggest that treatment conditions of 600 °C to 700 °C are incapable of introducing H^- into $SrTiO_3$. This could perhaps represent a limitation to treatment temperatures as was observed by Guo et al. (2020) with LiH treatments of $BaTiO_3$ [9]. However, we do not believe this to be the case. First, the clear presence of H^- in our 800 °C treated samples makes a temperature limit to H^- incorporation unlikely. Preliminary work we conducted on $SrTiO_3$ powders mixed with CaH_2 demonstrated that H^- can clearly be incorporated in $SrTiO_3$ at high concentrations at both 600 °C and 700 °C. Therefore, we interpret the apparent lack of H^- features as a manifestation of the significantly slower H-O exchange kinetics in single crystals as compared to powder samples. This still leaves open the possibility for H^- in our 600 °C and 700 °C treated samples, albeit at concentrations too low to detect via ^1H NMR.

5.3.3 Experimental – the capsule samples

Samples prepared via the capsule method were first analyzed via Raman spectroscopy. The Raman spectra show that while all samples are still $SrTiO_3$, there are some departures from the spectra of untreated $SrTiO_3$ crystals. We find that CaH_2 treatment results in the emergence of modes located at 128 cm^{-1}, 480 cm^{-1}, 693 cm^{-1}, and 803 cm^{-1}, with the 693 cm^{-1} being the most prominent. Additionally, the broad mode centered at ~300 cm^{-1} progressively decreases with more intense treatment. We attribute these modes to distortions of the $SrTiO_3$ structure resulting from H^- incorporation. Local distortions could cause subtle changes in cation site geometry and thus new Raman active modes. The extremely high symmetry of the pristine $SrTiO_3$ structure (single cubic perovskite) could make it especially susceptible to such affects. Despite the abundant new Raman-active modes, we find that there is no emergent polarization behavior, suggesting that the $SrTiO_3$ crystals are still isotropic and H^- incorporation has not pushed them into tetragonal or orthorhombic phase space, akin to the $BaTiO_3$ or $CaTiO_3$ structures.

Interestingly, when higher laser powers are used and exposure time to the laser is increased, the intensities of these features subside. Upon reduced exposure to the laser, these spectra then slowly return to their original states. There could be several reasons for this behavior. One possibility we propose is that the laser heats the samples, perhaps

temporarily relaxing some of the local site distortion, reverting back to a higher symmetry state. It is important to note that none of the emergent features we observe appear to be equivalent to any of the predicted H-associated normal modes. Although there may be some Raman activity associated with certain hydride modes, our samples likely do not contain high enough concentrations of H^- to produce features detectable via Raman spectroscopy. Notably, these emergent Raman features are absent from other published Raman spectra of $SrTiO_3$ crystals, including those annealed under H_2 [25].

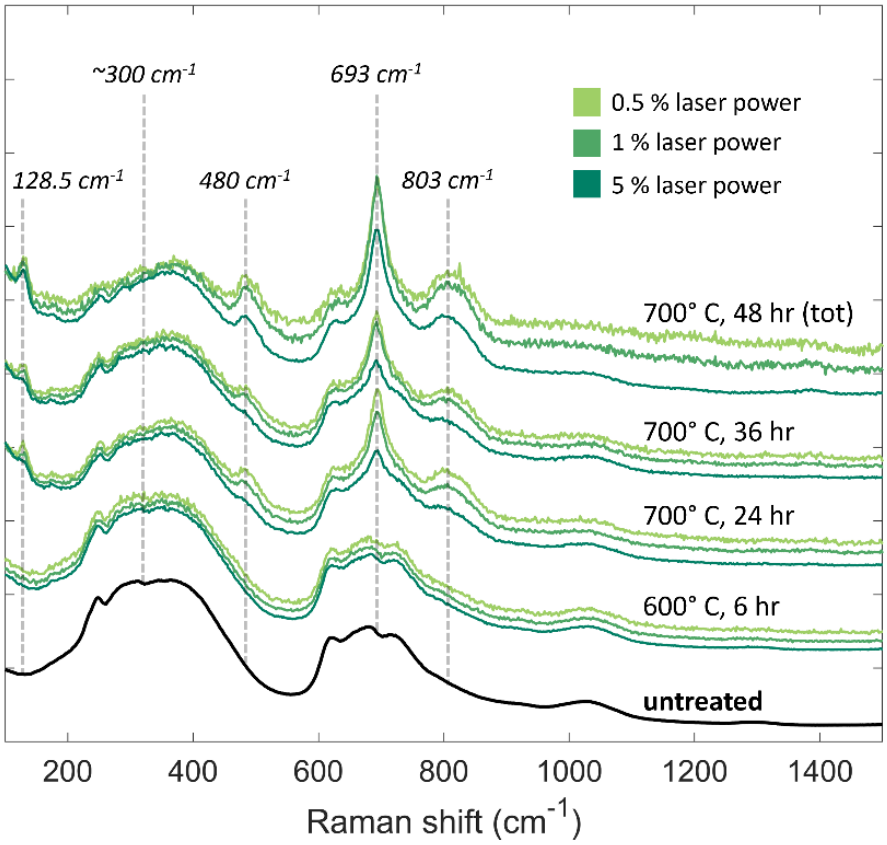

Figure 5.4 *–Raman spectra of the capsule-treated samples. Increased treatment conditions result in an increase in feature intensities at 128.5 cm^{-1}, 480 cm^{-1}, 693 cm^{-1}, and 803 cm^{-1}. Increasing the Raman laser power resulted in a decrease in the intensities of these features. A broad mode located at approximately 300 cm^{-1} decreases in intensity with increasing hydride content.*

Just like the pressed pellet samples, the capsule-prepared samples did not show detectable structural H via ^{1}H NMR (see Figure 5.5). Also like the pressed pellet samples, the capsule samples turned a deep blue color, appearing completely opaque in the case of the most intensely treated samples (Figure 5.6). Because the CaH_2 treated samples were so strongly absorbing, they had to be made extremely thin to observe the predicted Ti-H-Ti modes near 1300 cm^{-1}. In the most extreme case, we were able to achieve acceptable transmission through sample SC-70048h after grinding it to a thickness of ~2.5 μm. A series of combined IR and visible light transmission spectra from 650 to 26500 cm^{-1} for the suite of capsule samples are presented in Figure 5.7. Consistent with prior studies, reduction of $SrTiO_3$ produces an extremely broad band centered in the infrared region, at approximately 2170 cm^{-1} [28]. This feature has been previously documented when $SrTiO_3$ is reduced under a variety of conditions and is likely related to the reduction of Ti^{4+} to Ti^{3+} and production of oxygen vacancies[25,28]. Its full width half maximum in our samples is ~3000 cm^{-1} (However, note that this feature's location makes it difficult to isolate to accurately measure this value). In this case, IVCT likely occurs between adjacent O-bonded Ti sites, where delocalized excess charge is transferred between Ti, resulting in transitions between ephemeral Ti^{3+} and Ti^{4+} states. In our measurements, the intensity of this feature increases in conjunction with increased treatment times and temperatures, consistent with progressive oxygen loss. As expected, this electronic feature makes transmission in the further reaches of the infrared extremely difficult to achieve.

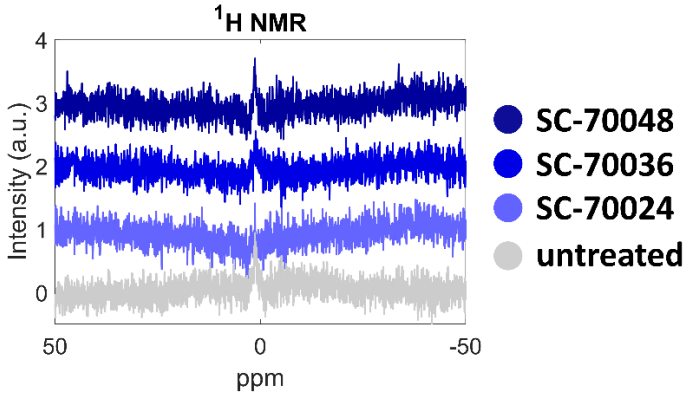

FIGURE 5.5 *– ^{1}H MAS NMR spectroscopy of the samples reacted with CaH_2 via the capsule method. Just like the 600 and 700 °C pellet samples, these spectra show no clear indication of hydride incorporation.*

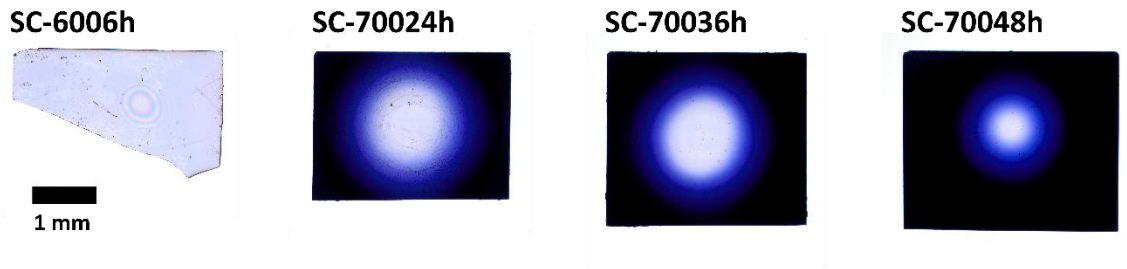

Figure 5.6 *– Images of the four CaH_2 treated samples that were measured via transmission spectroscopy. The samples become increasingly opaque with progressive treatment times. Except for SC-600h, all samples had to be thinned using a dimple grinder to achieve on-scale absorbance.*

In addition to the 2170 cm^{-1} band, an absorption centered at 513 nm emerges that is responsible for the deep blue color. The full width half maximum value of the absorption is approximately 3200 cm^{-1}, consistent with Ti^{4+}-Ti^{3+} IVCT seen in hibonite, for example[29]. In prior work done on $BaTiO_3$ powders, a transition to a blue color is closely associated with hydride incorporation[2], and we believe this to also be the case in our $SrTiO_3$ samples. Although there have been previous mentions of a dark violet-blue color in reduced $SrTiO_3$, these studies do not make specific claims about the possible role of hydrogen in contributing to these color changes[27]. Regardless, the causes of this 513 nm IVCT band are clearly distinct from the 2170 cm^{-1} band, as the latter can be induced through reduction under vacuum, in the complete absence of hydrogen[28].

Our FTIR spectra of $SrTiO_3$ subjected to the CaH_2 treatment contain a vibrational mode that is superimposed on 1326 cm^{-1} feature, ranging from 1308 cm^{-1} to 1305 cm^{-1} (Figure 5.7). For simplicity, we refer to this as the 1308 cm^{-1} feature. Longer sample treatment times cause the strength of this 1308 cm^{-1} feature to increase in intensity, eventually becoming dominant over the native mode at 1326 cm^{-1}. Given the 1308 cm^{-1} feature's correlation with CaH_2 treatment, and that its position is consistent with our finite difference, DFPT, and QMMD calculations, we assign this mode to the Ti-H-Ti vibrational mode. However, we note that the lack of corresponding ^1H NMR features that correlate directly with the 1308 cm^{-1} feature makes this assignment somewhat tenuous. Indeed, the intensity of the 1308 cm^{-1} band also seems to approximately correlate to the 2170 cm^{-1} IVCT band, meaning that it could possibly be the result of an oxygen vacancy related

structural distortion, rather than a hydride mode. Thus, we found that further testing in the form of vacuum annealing and H/D exchanges were necessary to assign the 1308 cm^{-1} mode to hydride.

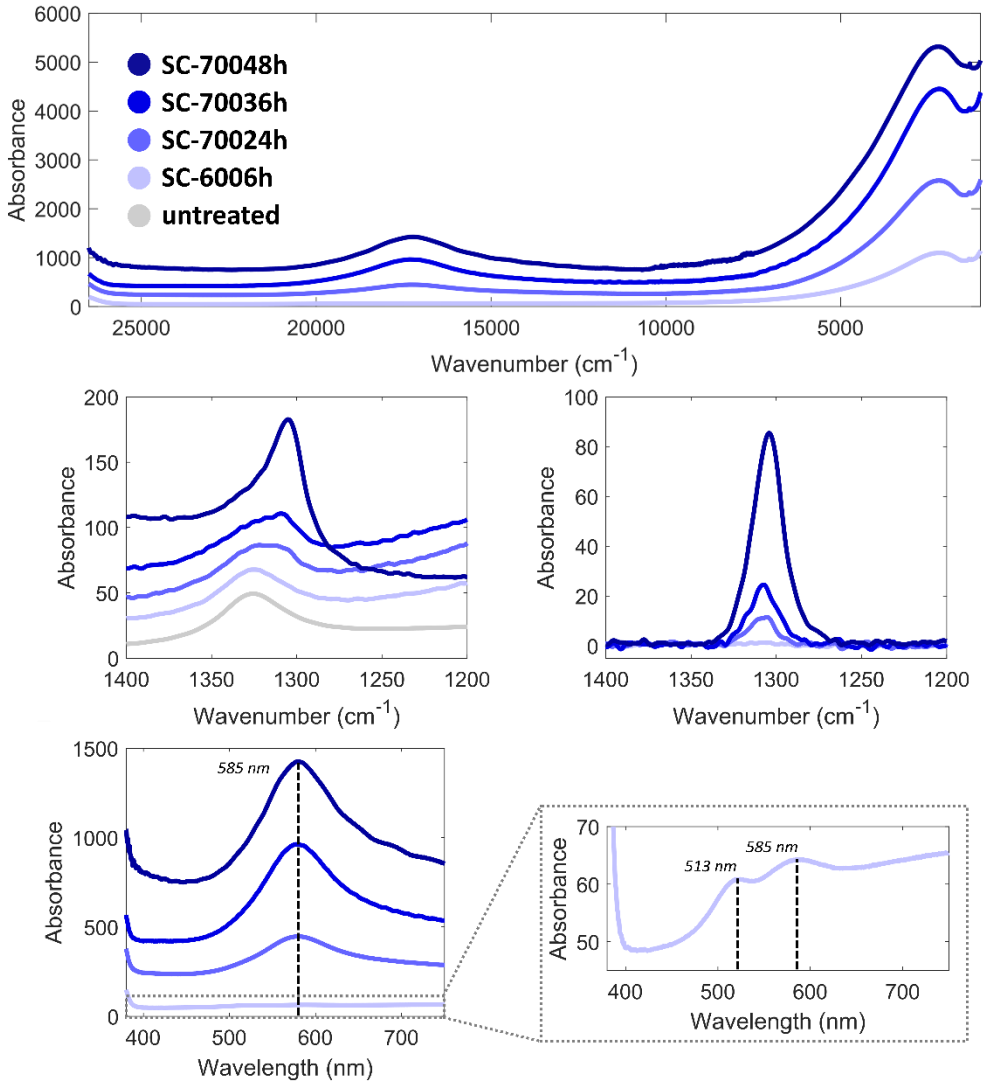

FIGURE 5.7 *– The transmission spectra collected from the CaH_2 capsule series of samples. All spectra have been normalized to a pathlength of 1 cm.* ***Top:*** *The extended range compilation of visible and infrared spectra showing the relative intensities of electronic and vibrational features.* ***Middle:*** *The 1300 cm^{-1} region, showing both the emergent 1308 cm^{-1} mode superimposed on the native 1326 cm^{-1} feature, and the isolated 1308 cm^{-1} feature.* ***Bottom:*** *The visible light region presented in units of wavelength. A zoomed-in view of the SC-6006h spectrum shows the coexistence of two absorptions, whereas all other spectra appear to only contain the 585 nm band.*

5.3.4 Vacuum Annealing

The progressive vacuum annealing of SC-70048h resulted in dramatic visual and spectroscopic changes. Like all of the CaH_2 treated crystals, SC-70048h was initially an extremely dark blue color, only achieving transparency when made extremely thin (Figure 5.5). However, after vacuum annealing, it became significantly more transparent and light purple in color (Figure 5.8). Subsequent vacuum annealing further reduced this purple color until the sample was completely colorless. Correspondingly, both the FTIR and visible light spectra of Vac1, Vac2, and Vac3 show these changes through the disappearance of the 585 nm IVCT band, the extreme reduction and eventual elimination of the 2170 cm^{-1} IVCT band, and the appearance of a new visible light absorption centered at 513 nm (Figure 5.9). After appearing in the initial vacuum annealed spectrum, this feature also was eliminated with additional vacuum heating. The full width half maximum of the 513 nm band is 1940 cm^{-1}, making its position and shape consistent with a *d-d* transition from an isolated Ti^{3+} site[30]. The intensity of this band is also consistent with a *d-d* transition, as it is significantly weaker than its 585 nm IVCT counterpart. For a Ti-based oxide, isolated Ti^{3+} centers associated with a localized excess charge are unusual, as the reduction of Ti^{4+} typically leads to IVCT.

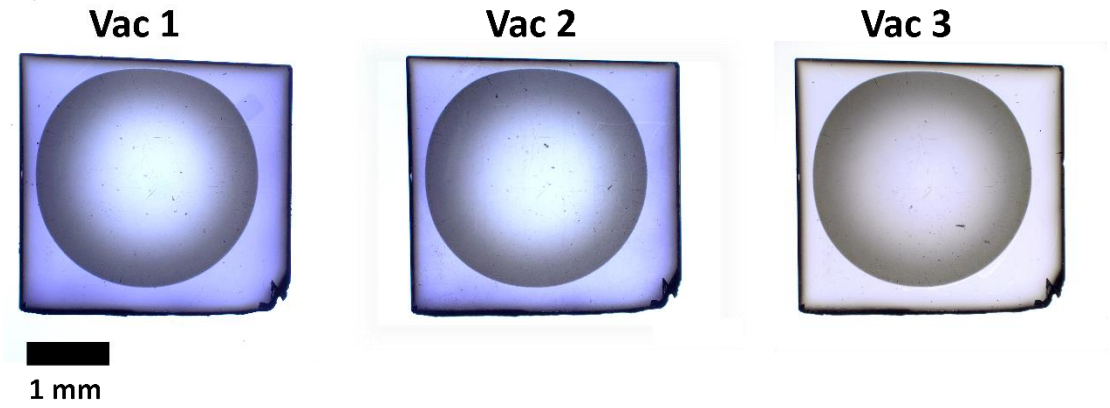

Figure 5.8 *– Images of the vacuum treated sample with a dimple ground into the center. This sample material was sliced from SC-70048h. Stage 1 was a 3.5 hr vacuum anneal at 500 °C, stage 2 was an additional 3.5 hr, 500 °C anneal, and stage 3 was a 3.5 hr vacuum anneal at 600 °C. Over the course of treatments, the crystal transitioned to a more transparent, purple state, lost color, and then became completely colorless.*

Vacuum annealing also led to the reduction and eventual elimination of the 1308 cm^{-1} feature (Figure 5.9). This corresponded to a shift in the feature to slightly higher wavenumbers. Interestingly, there is an apparent decoupling between the 1308 cm^{-1} and 585 nm bands, which seemed to be strongly correlated in the CaH_2 series of experiments. However, because both the 585 nm and 513 nm absorptions correspond to Ti^{3+}, just with different charge localization, there still seems to be a link between the 1308 cm^{-1} feature and Ti^{3+} generally. Unfortunately, because the reduction of the 1308 cm^{-1} feature also corresponded to the reduction of all other features associated with $SrTiO_3$ reduction, the vacuum heating analysis did not conclusively distinguish the cause of the 1308 cm^{-1} mode as resulting from either hydrogen incorporation or site distortion due to oxygen vacancies. As a consequence, deuteration experiments became a necessity for a confident assignment of the Ti-H-Ti mode.

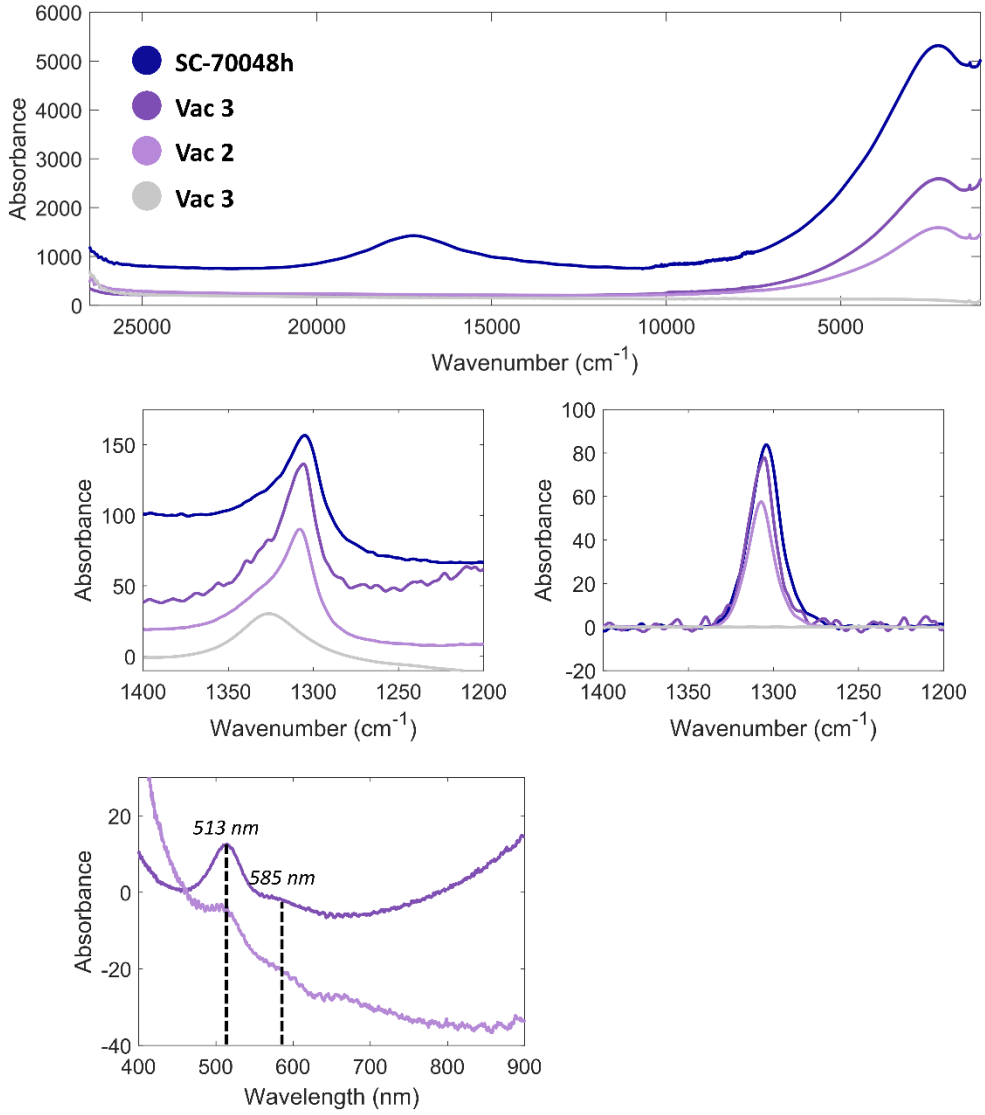

Figure 5.9 *– The transmission spectra collected from the vacuum annealed samples, presented in comparison to their parent material, SC-70048h. All spectra have been normalized to a pathlength of 1 cm.* ***Top:*** *Extended range compilation of visible and infrared spectra. The dramatic difference in intensity between the 513 nm and 585 nm features can be seen in this view and the progressive decrease in intensity of the 2170 cm^{-1} band is also apparent.* ***Middle:*** *The 1300 cm^{-1} region, showing both the emergent 1308 cm^{-1} mode superimposed on the native 1326 cm^{-1} feature, and the isolated 1308 cm^{-1} feature, which gradually diminishes before completely disappearing.* ***Bottom:*** *A zoomed-in view of the 513 nm bands in Vac1 and Vac2. A small portion of the 585 nm band remains in the Vac1 spectrum.*

5.3.5 H-D Exchanges

The starting material for the deuterium exchange was a crystal reacted with CaH_2 at 700 °C for 24 hours, equivalent to sample SC-70024h. A single sample was sliced for multiple treatments. Because prior experiments on $SrTiO_3$ have indicated that H_2 annealing may cause changes in color for reduced samples, indicating altered defect chemistry[26], we tested the effects of both H_2 and D_2 annealing. Much like with the vacuum annealed samples, both the H_2 and D_2 annealed samples underwent a dramatic color change, going from nearly opaque and dark blue to more transparent and a grayish purple color. This color change also corresponded to a virtual elimination of the 585 nm IVCT band and the emergence of the narrower 513 nm band (Figure 5.10), resulting in virtually identical visual absorptions for both samples. Additionally, the 2170 cm^{-1} IVCT band remained very similar in intensity between the two samples, albeit significantly diminished when compared to samples subjected only to the CaH_2 treatment.

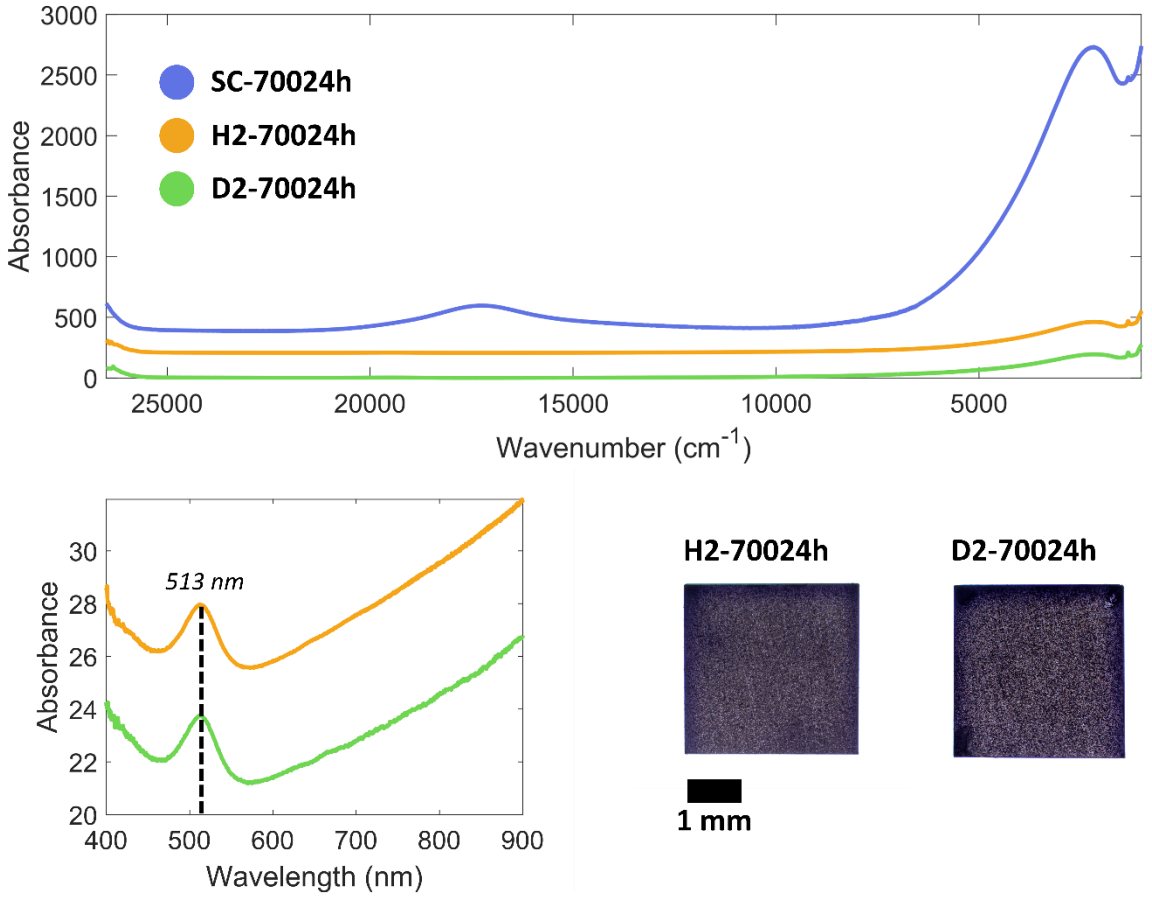

Figure 5.10 *– The transmission spectra collected from the hydrogen and deuterium annealed samples, presented in comparison to SC-70024h. All spectra have been normalized to a pathlength of 1 cm.* ***Top:*** *Extended range compilation of visible and infrared spectra. The decrease in the 2170 cm^{-1} band compared to SC-70024h is significant.* ***Bottom:*** *(left) Zoomed in view of the visible light region for H2-70024h and D2-70024h showing approximately equivalent intensity 513 nm bands. (right) Transmitted light view of the two samples at full 500 µm thickness. They have both turned a purple-gray color and are noticeably darker near their edges.*

The only spectral feature that differed between H2-70024h and D2-70024h was the 1308 cm^{-1} band, which somewhat diminished in the D_2 sample compared to the H_2 sample. Initially, the degree to which the 1308 cm^{-1} band was reduced in the D_2 annealed sample appeared to be rather marginal, with integrated intensities diminished by only about 20 – 30%. However, we were able to determine that the lowering of the 1308 cm^{-1} feature was more pronounced closer to the pristine, factory-polished surface that was directly exposed

to the D_2 gas flow. This analysis was accomplished by grinding a dimple into the center of each sample, effectively producing a concave wafer of variable thickness. By measuring spectra in sections with different thicknesses (i.e, different spots within the dimple), we found that the path length normalized intensity of the 1308 cm^{-1} feature in the D_2 annealed sample changed in response to sample thickness (Figure 5.11). More specifically, we found that analyses in thinner sections of the deuterated sample corresponded to a greater proportional reduction of the 1308 cm^{-1} band. This was not observed in the H_2 annealed sample, which had essentially unchanged normalized intensities regardless of path length. Ultimately, we determined that sample volumes closer to the surface of the crystal saw a 90% or greater reduction of the 1308 cm^{-1} feature's intensity when comparing D_2 to H_2 treatments. This implies a gradient for the integrated intensity of the 1308 cm^{-1} band relative to the sample surface in the D_2 annealed sample, strongly suggesting successful H/D exchange. Thus, we can confidently attribute the 1308 cm^{-1} feature to hydrogen. Furthermore, based on the consistency of this mode position with our DFT results, we assign this specific band to the Ti-H-Ti stretching mode.

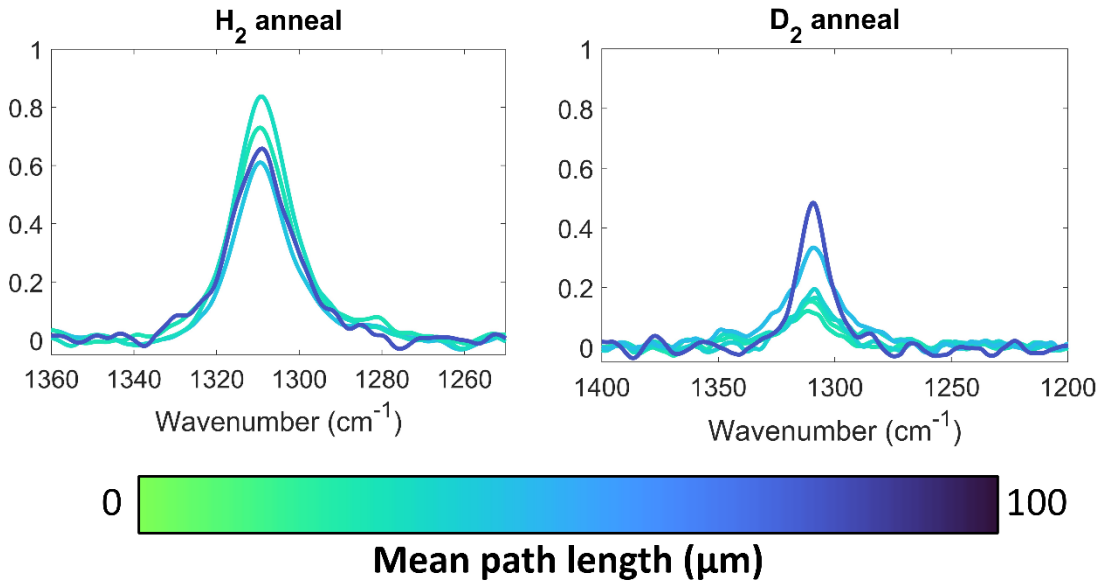

Figure 5.11 *– Isolated 1308 cm^{-1} bands from spectra taken in different sections of the dimpled H_2 and D_2 annealed samples. All spectra are normalized to their mean path length in cm and color weighted based on their path length. For the H_2 sample, there is a distribution in the 1308 cm-1 intensity, but no systematic variance with path length. For the D2 sample, the 1308 cm-1 is reduced relative to the H2 sample at all path*

lengths and systematically decreases with decreasing path length. This indicates a reduction in band intensity at sample volumes closer to the surface, consistent with H-D exchange.

This result also demonstrates that FTIR can have a higher sensitivity for H^- detection than ^1H NMR, despite NMR's current status as the dominant form of analysis for this application. Across all the samples we analyzed via FTIR, there were no clearly resolvable H^- peaks in any of the ^1H NMR spectra, even for those with the highest H^- concentrations. Therefore, FTIR could prove to be a valuable technique for future studies of detecting hydride in oxide materials.

5.3.6 The Structural State of Hydrogen

The current discussion on the structural state of hydrogen in reduced $SrTiO_3$ (and other titanates) reveals a complex landscape of possible defect states. Much of the conversation surrounding H_O occupations in titanate perovskites centers on interpreting ^1H NMR behavior. Broad, negative shifted features are unambiguously attributed to H^- and are thought to be a result of Knight shifts[3,4] but attributing a specific atomistic structural explanation to these shifts is still an area of active discussion. Misaki et al. (2019) initially proposed a model for $BaTiO_3$ in which negative shifted ^1H NMR features are the consequence of a doubly occupied V_O site, where the observed Knight shift is the result of H and Ti *3d* orbital hybridization[3]. DFT results from Iwazaki et al. (2014) supported a series of possible H^- configurations in $SrTiO_3$ that likely vary based on treatment conditions (i.e., hydrogen source), where both doubly and singly occupied V_O sites are possible[31]. These calculations concluded that a specific double-occupation configuration was most likely for $SrTiO_3$ subjected to a H_2 gas flow but did not comment on cases where hydride salts act as a reducing agent and hydrogen source. Demonstrations of the ability for H_2 anneals to partially or fully reverse coloration in $SrTiO_3$ despite a lack of available oxygen[25–27] point to the possibility of a doubly-occupied V_O site where reduced Ti^{3+} centers have been passivated and reverted to Ti^{4+}. Taken in combination with the explanation put forth by Misaki et al. (2019), where Knight shifts are best explained by double occupation of the V_O site, this would suggest that titanate perovskites with very negatively shifted ^1H NMR signals could sometimes be less intensely colored. However, this is not the case for

our sample materials, nor does this appear to hold true for other ^{1}H NMR studies[2]. Misaki et al. (2019) account for this by suggesting the coexistence of other Ti^{3+}-associated defect states, like oxygen vacancies and single-occupation hydride[3], which is a distinct possibility. However, Aleksis et al. (2022) conclude that Knight shifts in CaH_2-treated $BaTiO_3$ can be and are attributed to single occupancy hydride states[4]. Additionally, it was also concluded that the concentration of V_O could contribute to the Knight shift, meaning that the positions of negatively shifted ^{1}H NMR features may be more indicative of the overall oxygen-deficit of $BaTiO_3$ (and $SrTiO_3$) than strictly hydride content.

Considering our results in the context of the existing literature, we conclude that the dominant state of hydride in our samples is a single H^- at the V_O site. One factor in this assignment is the initial intense coloration of the samples, which would seem to rule out full passivation of Ti^{3+} to Ti^{4+}, via double occupation (although we acknowledge that this observation does not necessarily rule out the possibility of coexisting singly and doubly occupied V_O sites). Nevertheless, the presence of only a single IR-active vibrational mode in close vicinity to the DFT-predicted Ti-H-Ti stretching frequency also strongly implies that only one H^- structural state is present.

5.3.7 Explanation for the Vacuum and H_2 Annealing Behavior

Despite our confidence in assigning the 1308 cm^{-1} feature to hydride, there remain some spectroscopic behaviors from the vacuum and hydrogen annealed samples that are either unusual or counterintuitive. First of these is the replacement of the 585 nm IVCT band by the 513 nm *d-d* transition band. The former appears to be intrinsically tied to structural hydride, but it was virtually eliminated when samples were subjected to either H_2 or vacuum heating, even when significant hydride signal remained. We propose that this change in the visible light spectrum can be attributed to a change in the band structure of the reduced Ti^{3+} sites. The IVCT band implies a delocalization of the excess negative charge associated with Ti reduction, and its correlation with H^- incorporation perhaps suggests that this charge transfer is mediated specifically by Ti-bonded hydride. Meanwhile, a *d-d* transition implies the localization of charge to Ti, forming a long-lived and possibly more isolated Ti^{3+} state. This isolated Ti^{3+} could be approximately equivalent

to the polaron-like state explored by Eklöf-Österberg et al. (2020) and Aleksis et al. (2022) in $BaTiO_3$ [4,32].

The process of transitioning between these states seems to be dependent mostly on temperature, as it occurred under both vacuum and a hydrogen atmosphere. This is because the 513 nm band was observed in every sample that was treated at temperatures of 500 °C or below (see visible light spectra in Figures 5.9 and 5.10) and was also observed coexisting with the 585 nm IVCT band in sample SC-6006h (Figure 5.6). One possibility is that heating at temperatures high enough for diffusion processes, but too low for significant O or H loss could allow H^- defect centers to become more spread out within the crystal. Initial CaH_2 treatments likely lead to zones of many adjacent occupations by H^- within the crystals. When the density of H^- occupations is high, the excess Ti electrons can become delocalized, and IVCT may occur. This results in the 585 nm band (and perhaps contributes to the 2170 cm^{-1} band as well). Once the crystals are heated, these H^- occupancies can become more dispersed, and their associated Ti^{3+} centers do as well. This is indirectly supported by our Raman results. If the emergent Raman modes are assigned to local lattice distortions resulting from high densities of H^- defects, then defect dispersal via heating from the Raman laser may explain why these modes are reduced with increased laser power. Additionally, we found that the Raman spectra of vacuum annealed and H_2/D_2 annealed samples were nearly identical to the untreated $SrTiO_3$ Raman spectrum, perhaps further implying that decreasing the local density of H^- defect states can relieve lattice distortion. More advanced studies utilizing techniques that can target nanoscale distributions of H and lattice distortions would be necessary to confirm whether this explanation is valid.

The second unusual change observed in the vacuum and H_2 annealed samples was the disappearance of the 2170 cm^{-1} IVCT band. Normally, the disappearance of this feature would be associated with oxidation of a reduced $SrTiO_3$ crystal, as its presence is a hallmark of oxygen vacancies (and possibly H^-), and by extension, Ti^{3+}. However, virtually no oxygen is available under either of the treatment conditions. This is especially puzzling for the sample Vac3, which appears to have returned to the pristine $SrTiO_3$ state after progressive annealing under high vacuum. Our current explanation for this is the

progressive loss of Sr into the vapor phase. By coupling a Sr vacancy to a preexisting oxygen vacancy, charge balance can be achieved without the need for oxygen to reincorporate into $SrTiO_3$. The coupled Sr and O vacancies carry a net neutral charge as a Schottky defect, effectively passivating the Ti^{3+} centers associated with the respective O vacancy or hydride and removing all IVCT and *d-d* bands. At the annealing temperatures tested, the vapor pressure of metallic Sr is below 1 mbar, but still high enough that a defect level concentration of Sr could conceivably be removed from the bulk sample. However, for Sr to be removed as a vapor, it must be reduced from Sr^{2+} to Sr^0 (metallic Sr). We believe that this reduction of Sr^{2+} is initially achieved through the simultaneous oxidation of H^- to H_2 and Ti^{3+} to Ti^{4+}. For samples under vacuum, as Sr is reduced, significant amounts of hydride are oxidized and lost as H_2. Under an atmosphere of H_2, this redox process may preferentially target Ti^{3+} centers for oxidation rather than H^-, as the partial pressure of H_2 is too high for hydrogen loss. This could explain how the 2170 cm^{-1} band could be reduced in sample H2-70024h while the 1308 cm^{-1} band remained virtually unchanged. Nevertheless, we emphasize that further work utilizing techniques that can monitor Sr loss would be necessary to confirm whether this truly is the mechanism at play.

5.3.8 Accuracy of DFT Applied to Hydride

DFT techniques have been applied extensively to making predictions about hydrogen's infrared behavior, although this is most in the context of OH^-. Through these studies, the PBE level of theory as employed by the VASP, CASTEP, and Quantum Espresso softwares has repeatedly demonstrated errors in assigning precise OH^- stretching mode frequencies. However, the origins of these errors are not precisely known, and both under- and over-estimations of the stretching frequencies are commonly observed, even when the calculated structural state of hydrogen is known to be accurate. Thus, although DFT can provide valuable context in interpreting IR spectra, this unpredictable inaccuracy puts inherent limits on making absolute predictions of this type for OH-containing systems. What has not been explored as extensively is the ability of these methods to make predictions about H^- related modes.

Assuming the assignment of the 1308 cm^{-1} mode to the Ti-H-Ti vibration is correct, our results indicate that the PBE functional can predict hydride's vibrational behavior in $SrTiO_3$ with fairly high accuracy. Our DFPT result differs from experiment by only 19 cm^{-1}, while the QMMD partial vDOS contains a peak at 1282 cm^{-1}, a difference on the order of 20 - 30 cm^{-1} (Figure 5.12). When considering the QMMD results, it is important to keep in mind that our simulation predicts an elevated pressure of ~2GPa for the given unit cell volume, which could result in shifts of the Ti-H-Ti mode, meaning that adjustments of cell volume could produce even more accurate results. Despite the apparent accuracy of theory applied to $SrTiO_3$, assessment of just one material is not enough to make claims about DFT's overall efficacy when applied to hydride-containing oxide systems. Eklöf-Österberg et al., 2020 were able to successfully observe Ti-H-Ti stretching and bending modes in hydride $BaTiO_3$ powders via inelastic neutron scattering and compare their results to frozen phonon (finite differences) calculations employing both PBE and HSE functionals[32]. Their analyses showed a tendency for the PBE functional to underestimate mode energies on the order of 15 to 60 cm^{-1}, while HSE techniques had greater accuracy. Janotti et al., 2007 predicted the positions of hydride-related modes for two other materials where IR or other vibrational spectroscopy exist: MgO and ZnO[33]. In multiple studies, hydride containing MgO has produced IR-active modes at 1024, 1032, and 1053 cm^{-1}, differing from Janotti et al. 2007's predicted position (950 cm^{-1}) by 74 to 103 cm^{-1} [11,33,34]. Koch et al., 2012 observed H^- associated modes in ZnO centered at 742 and 792 cm^{-1} via photoconductivity measurements, for a discrepancy of 22 to 32 cm^{-1} from Janotti et al., 2007 and 19 to 69 cm^{-1} from a later study[35,36]. In Be-doped natural Al_2O_3, Jollands and Balan 2022 predicted Be-H groups would have a vibrational mode of 2602 cm^{-1}, while they observed Be-associated modes at 2491 cm^{-1} and 2523 cm^{-1} giving a potential error range of 111 to 79 cm^{-1} [37]. Taken together, this series of computational and experimental comparisons suggest that DFT methods show promise for generally predicting the positions of hydride modes in oxides but may still be subject to errors similar to those seen for OH^-.

With our work on $SrTiO_3$ included, the available DFT-experimental comparisons for H^- in oxides remains limited to just a handful examples. For other materials where H^- is predicted as stable, like rutile-type TiO_2 [38] and SnO_2 [39], H^- associated vibrational modes

have yet to be experimentally identified. However, H^- modes have been observed in a variety of materials that have not yet been investigated via DFT: CaO, SrO, and Sr apatite ($Sr_5(PO_4)H$)[10,11], leaving open the possibility for future studies in this vein.

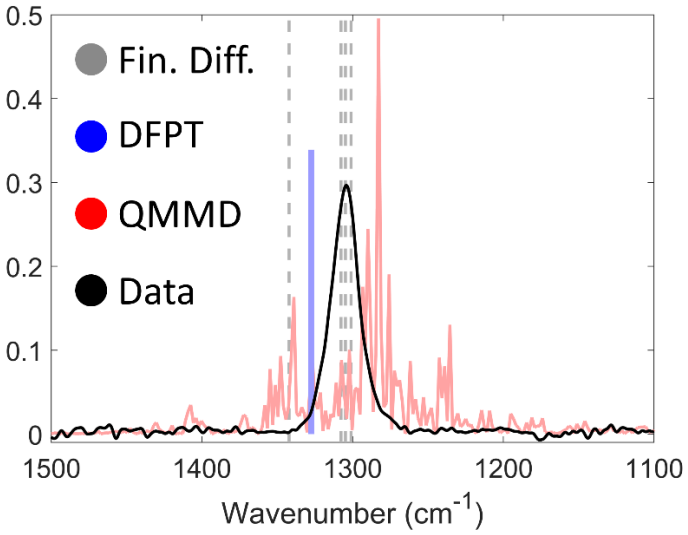

Figure 5.12 *– Comparison of the QM-MD calculated partial vDOS, 3x2x2 supercell DFPT calculated mode and the 1308 cm^{-1} mode isolated from the infrared spectrum of SC-70048h. The DFT methods employed seem to be accurate enough to predict the position of the Ti-H-Ti stretching mode within a few 10s of cm^{-1}.*

5.3.9 Expansion of Synthesis Parameters – $SrTiO_3$ and Beyond

Our experiments conclusively demonstrate that hydride may be incorporated into $SrTiO_3$ crystals through reaction with CaH_2 at temperature conditions up to at least 800 °C. In prior studies of titanate pervoskites, the upper limit of these reactions was placed at ~600° C, under the assumption that CaH_2 would completely decompose at these elevated temperatures. However, this does not hold true for CaH_2 under a H_2 atmosphere. Within a closed system in which the evolved H_2 gas from CaH_2 is not allowed to escape (like the evacuated tubes in the present work), CaH_2 will not completely decompose, but rather equilibrate to some pressure of H_2. At our highest investigated temperature of 800° C, this pressure is on the order of approximately 2.3×10^4 Pa[40]. In the volumes of our evacuated tubes, this corresponds to the decomposition of only about 2 mg of CaH_2, a small fraction of the total mass. Thus, even modest amounts of CaH_2 will be stable at elevated

temperatures and be available for reaction. Studies on hydride doping of other materials have already demonstrated this potential with reactions involving other hydride reagents, like the reaction of hydroxyapatite ceramics with TiH_2 [41]. The preferable kinetics afforded by higher temperature reactions with CaH_2 and other hydrides has yet to be explored in depth and could present new pathways for easily introducing hydride and oxygen vacancies into a range of oxide materials.

5.4 Conclusions

Aided by first-principles results, we have provided strong evidence for identifying hydride speciation in $SrTiO_3$ perovskite crystals through infrared spectroscopy. DFT predictions proved crucial in the identification of the hydride mode, as the feature both overlaps closely with a native $SrTiO_3$ feature and occurs in a highly absorbing region of reduced $SrTiO_3$'s infrared spectrum. The former of these factors could make low concentrations of hydride easy to overlook without the prior knowledge provided by DFT. Additionally, we have found that infrared spectroscopy can be significantly more sensitive to hydride than ^{1}H NMR, which is the technique most often employed in searching for hydride in oxide materials. Therefore, FTIR may prove valuable in the future studies of oxyhydrides, especially in materials where hydride is present in nonstoichiometric concentrations.

The use of FTIR could also expand the study of oxyhydrides to additional contexts where the more frequently used analytical methods of neutron scattering and ^{1}H NMR are either impossible or impractical to utilize. For example, FTIR is well-suited for making *in situ* measurements in high pressure cells and analyzing small sample volumes. These points in particular point to FTIR as a potentially key analytical tool for future studies of the interior of earth and other planetary bodies, where perovskite materials are abundant, and the possibility of hydride has been given limited consideration.

In addition to the identification of hydride via FTIR, we have also observed a number of unusual spectroscopic behaviors that seem to associate with incorporation of hydride and its structural evolution in the $SrTiO_3$ lattice. There is implication that the electronic

structure of $SrTiO_3$ could possibly be fine-tuned via manipulation of structural hydride, and future studies of the interplay between hydride and the electronic features at 513 nm, 585 nm, and 2170 cm^{-1} could prove fruitful.

References

(1) Sakaguchi, T.; Kobayashi, Y.; Yajima, T.; Ohkura, M.; Tassel, C.; Takeiri, F.; Mitsuoka, S.; Ohkubo, H.; Yamamoto, T.; Kim, J. eun; Tsuji, N.; Fujihara, A.; Matsushita, Y.; Hester, J.; Avdeev, M.; Ohoyama, K.; Kageyama, H. Oxyhydrides of (Ca,Sr,Ba)TiO_3 Perovskite Solid Solutions. *Inorg. Chem.* **2012**, *51* (21), 11371–11376. https://doi.org/10.1021/ic300859n.

(2) Kobayashi, Y.; Hernandez, O. J.; Sakaguchi, T.; Yajima, T.; Roisnel, T.; Tsujimoto, Y.; Morita, M.; Noda, Y.; Mogami, Y.; Kitada, A.; Ohkura, M.; Hosokawa, S.; Li, Z.; Hayashi, K.; Kusano, Y.; Kim, J. eun; Tsuji, N.; Fujiwara, A.; Matsushita, Y.; Yoshimura, K.; Takegoshi, K.; Inoue, M.; Takano, M.; Kageyama, H. An Oxyhydride of $BaTiO_3$ Exhibiting Hydride Exchange and Electronic Conductivity. *Nature Mater* **2012**, *11* (6), 507–511. https://doi.org/10.1038/nmat3302.

(3) Misaki, T.; Oikawa, I.; Takamura, H. Negative Knight Shift in Ba-Ti Oxyhydride: An Indication of the Multiple Hydrogen Occupation. *Chem. Mater.* **2019**, *31* (18), 7178–7185. https://doi.org/10.1021/acs.chemmater.9b01434.

(4) Aleksis, R.; Nedumkandathil, R.; Papawassiliou, W.; Carvalho, J. P.; Jaworski, A.; Häussermann, U.; Pell, A. J. Probing the Electronic Structure and Hydride Occupancy in Barium Titanium Oxyhydride through DFT-Assisted Solid-State NMR. *Phys. Chem. Chem. Phys.* **2022**, *24* (46), 28164–28173. https://doi.org/10.1039/D2CP04675J.

(5) Varley, J. B.; Janotti, A.; Van de Walle, C. G. Hydrogenated Vacancies and Hidden Hydrogen in $SrTiO_3$. *Phys. Rev. B* **2014**, *89* (7), 075202. https://doi.org/10.1103/PhysRevB.89.075202.

(6) Gao, T.; Nian, L.; Jin, L.; Sun, H.; Zhang, T.; Yang, J.; Gu, Z.; Peng, L.; Nie, Y. Giant Switchable Persistent Photoconductivity in Soft Chemistry Reduced $SrTiO_3$. *Adv Elect Materials* **2023**, *9* (7), 2300068. https://doi.org/10.1002/aelm.202300068.

(7) Yajima, T.; Takeiri, F.; Aidzu, K.; Akamatsu, H.; Fujita, K.; Yoshimune, W.; Ohkura, M.; Lei, S.; Gopalan, V.; Tanaka, K.; Brown, C. M.; Green, M. A.; Yamamoto, T.; Kobayashi, Y.; Kageyama, H. A Labile Hydride Strategy for the Synthesis of Heavily Nitridized $BaTiO_3$. *Nature Chem* **2015**, *7* (12), 1017–1023. https://doi.org/10.1038/nchem.2370.

(8) Nedumkandathil, R.; Jaworski, A.; Grins, J.; Bernin, D.; Karlsson, M.; Eklöf-Österberg, C.; Neagu, A.; Tai, C.-W.; Pell, A. J.; Häussermann, U. Hydride Reduction of $BaTiO_3$ − Oxyhydride Versus O Vacancy Formation. *ACS Omega* **2018**, *3* (9), 11426–11438. https://doi.org/10.1021/acsomega.8b01368.

(9) Guo, H.; Jaworski, A.; Ma, Z.; Slabon, A.; Bacsik, Z.; Nedumkandathil, R.; Häussermann, U. Trapping of Different Stages of $BaTiO_3$ Reduction with LiH. *RSC Adv.* **2020**, *10* (58), 35356–35365. https://doi.org/10.1039/D0RA07276A.

(10) Alexander Mutschke; Thomas Wylezich; Clemens Ritter; Antti J. Karttunen; Nathalie Kunkel. An Unprecedented Fully H^- -Substituted Phosphate Hydride $Sr_5(PO_4)_3H$ Expanding the Apatite Family. *European Journal of Inorganic Chemistry* **2019**, *48*, 5073–5076. https://doi.org/10.1002/ejic.201901151.

(11) González, R.; Chen, Y.; Mostoller, M. Substitutional H^- -Ion Vibrations in the Alkaline-Earth Oxides Reduced at High Temperatures. *Phys. Rev. B* **1981**, *24* (12), 6862–6869. https://doi.org/10.1103/PhysRevB.24.6862.

(12) Yajima, T.; Takahashi, K.; Nakajima, H.; Honda, T.; Ikeda, K.; Otomo, T.; Hiroi, Z. High-Pressure Synthesis of Transition-Metal Oxyhydrides with Double-Perovskite Structures. *Inorg. Chem.* **2022**, *61* (4), 2010–2016. https://doi.org/10.1021/acs.inorgchem.1c03162.

(13) Mao, H.-K.; Hu, Q.; Yang, L.; Liu, J.; Kim, D. Y.; Meng, Y.; Zhang, L.; Prakapenka, V. B.; Yang, W.; Mao, W. L. When Water Meets Iron at Earth's Core–Mantle Boundary. *National Science Review* **2017**, *4* (6), 870–878. https://doi.org/10.1093/nsr/nwx109.

(14) Perdew, J. P.; Burke, K.; Ernzerhof, M. Generalized Gradient Approximation Made Simple. *Phys. Rev. Lett.* **1996**, *77* (18), 3865–3868. https://doi.org/10.1103/PhysRevLett.77.3865.

(15) Perdew, J. P.; Burke, K.; Ernzerhof, M. Generalized Gradient Approximation Made Simple [Phys. Rev. Lett. 77, 3865 (1996)]. *Phys. Rev. Lett.* **1997**, *78* (7), 1396–1396. https://doi.org/10.1103/PhysRevLett.78.1396.

(16) Kresse, G.; Furthmüller, J. Efficiency of Ab-Initio Total Energy Calculations for Metals and Semiconductors Using a Plane-Wave Basis Set. *Computational Materials Science* **1996**, *6* (1), 15–50. https://doi.org/10.1016/0927-0256(96)00008-0.

(17) Kresse, G.; Furthmüller, J. Efficient Iterative Schemes for *Ab Initio* Total-Energy Calculations Using a Plane-Wave Basis Set. *Phys. Rev. B* **1996**, *54* (16), 11169–11186. https://doi.org/10.1103/PhysRevB.54.11169.

(18) Kresse, G.; Hafner, J. *Ab Initio* Molecular Dynamics for Liquid Metals. *Phys. Rev. B* **1993**, *47* (1), 558–561. https://doi.org/10.1103/PhysRevB.47.558.

(19) Kresse, G.; Joubert, D. From Ultrasoft Pseudopotentials to the Projector Augmented-Wave Method. *Phys. Rev. B* **1999**, *59* (3), 1758–1775. https://doi.org/10.1103/PhysRevB.59.1758.

(20) Blöchl, P. E.; Jepsen, O.; Andersen, O. K. Improved Tetrahedron Method for Brillouin-Zone Integrations. *Phys. Rev. B* **1994**, *49* (23), 16223–16233. https://doi.org/10.1103/PhysRevB.49.16223.

(21) Karhánek, D. Dakarhanek/VASP-Infrared-Intensities: VASP-Infrared-Intensities, 2020. https://doi.org/10.5281/ZENODO.3930989.

(22) Lin, S.-T.; Blanco, M.; Goddard, W. A. The Two-Phase Model for Calculating Thermodynamic Properties of Liquids from Molecular Dynamics: Validation for the Phase Diagram of Lennard-Jones Fluids. *The Journal of Chemical Physics* **2003**, *119* (22), 11792–11805. https://doi.org/10.1063/1.1624057.

(23) Lin, S.-T.; Maiti, P. K.; Goddard, W. A. Two-Phase Thermodynamic Model for Efficient and Accurate Absolute Entropy of Water from Molecular Dynamics Simulations. *J. Phys. Chem. B* **2010**, *114* (24), 8191–8198. https://doi.org/10.1021/jp103120q.

(24) Pascal, T. A.; Lin, S.-T.; Goddard III, W. A. Thermodynamics of Liquids: Standard Molar Entropies and Heat Capacities of Common Solvents from 2PT Molecular Dynamics. *Phys. Chem. Chem. Phys.* **2011**, *13* (1), 169–181. https://doi.org/10.1039/C0CP01549K.

(25) Mochizuki, S.; Fujishiro, F.; Ishiwata, K.; Shibata, K. Defect-Induced Optical Absorption and Photoluminescence of Verneuil-Grown SrTiO3 Crystal. *Physica B: Condensed Matter* **2006**, *376–377*, 816–819. https://doi.org/10.1016/j.physb.2005.12.204.

(26) Jalan, B.; Engel-Herbert, R.; Mates, T. E.; Stemmer, S. Effects of Hydrogen Anneals on Oxygen Deficient $SrTiO_{3-x}$ Single Crystals. *Applied Physics Letters* **2008**, *93* (5), 052907. https://doi.org/10.1063/1.2969037.

(27) Gong, W.; Yun, H.; Ning, Y. B.; Greedan, J. E.; Datars, W. R.; Stager, C. V. Oxygen-Deficient $SrTiO_{3-x}$, x = 0.28, 0.17, and 0.08. Crystal Growth, Crystal Structure, Magnetic, and Transport Properties. *Journal of Solid State Chemistry* **1991**, *90* (2), 320–330. https://doi.org/10.1016/0022-4596(91)90149-C.

(28) Hanzig, J.; Abendroth, B.; Hanzig, F.; Stöcker, H.; Strohmeyer, R.; Meyer, D. C.; Lindner, S.; Grobosch, M.; Knupfer, M.; Himcinschi, C.; Mühle, U.; Munnik, F. Single Crystal Strontium Titanate Surface and Bulk Modifications Due to Vacuum Annealing. *Journal of Applied Physics* **2011**, *110* (6), 064107. https://doi.org/10.1063/1.3638692.

(29) Ihinger, P. D.; Stolper, E. The Color of Meteoritic Hibonite: An Indicator of Oxygen Fugacity. *Earth and Planetary Science Letters* **1986**, *78* (1), 67–79. https://doi.org/10.1016/0012-821X(86)90173-1.

(30) Moulton, P. F.; Cederberg, J. G.; Stevens, K. T.; Foundos, G.; Koselja, M.; Preclikova, J. Characterization of Absorption Bands in Ti:Sapphire Crystals. *Opt. Mater. Express* **2019**, *9* (5), 2216. https://doi.org/10.1364/OME.9.002216.

(31) Iwazaki, Y.; Gohda, Y.; Tsuneyuki, S. Diversity of Hydrogen Configuration and Its Roles in $SrTiO_{3-\delta}$. *APL MATERIALS* **2014**, *2* (1), 012103. https://doi.org/10.1063/1.4854355.

(32) Eklöf-Österberg, C.; Mazzei, L.; Granhed, E. J.; Wahnström, G.; Nedumkandathil, R.; Häussermann, U.; Jaworski, A.; Pell, A. J.; Parker, S. F.; Jalarvo, N. H.; Börjesson, L.; Karlsson, M. The Role of Oxygen Vacancies on the Vibrational Motions of Hydride Ions in the Oxyhydride of Barium Titanate. *J. Mater. Chem. A* **2020**, *8* (13), 6360–6371. https://doi.org/10.1039/C9TA11912D.

(33) Janotti, A.; Van de Walle, C. G. Hydrogen Multicentre Bonds. *Nature Mater* **2007**, *6* (1), 44–47. https://doi.org/10.1038/nmat1795.

(34) González, R.; Vergara, I.; Cáceres, D.; Chen, Y. Role of Hydrogen and Lithium Impurities in Radiation Damage in Neutron-Irradiated MgO Single Crystals. *Phys. Rev. B* **2002**, *65* (22), 224108. https://doi.org/10.1103/PhysRevB.65.224108.

(35) Koch, S. G.; Lavrov, E. V.; Weber, J. Photoconductive Detection of Tetrahedrally Coordinated Hydrogen in ZnO. *Phys. Rev. Lett.* **2012**, *108* (16), 165501. https://doi.org/10.1103/PhysRevLett.108.165501.

(36) Du, M.-H.; Singh, D. J. Hydrogen in Anion Vacancies of Semiconductors. *Phys. Rev. B* **2009**, *79* (20), 205201. https://doi.org/10.1103/PhysRevB.79.205201.

(37) Jollands, M. C.; Balan, E. Beryllium Incorporation in Corundum. *MinMag* **2022**, *86* (5), 758–766. https://doi.org/10.1180/mgm.2022.63.

(38) Palfey, W. R.; Rossman, G. R.; Goddard, W. A. Structure, Energetics, and Spectra for the Oxygen Vacancy in Rutile: Prominence of the Ti–H_O–Ti Bond. *J. Phys. Chem. Lett.* **2021**, *12* (41), 10175–10181. https://doi.org/10.1021/acs.jpclett.1c02850.
(39) Singh, A. K.; Janotti, A.; Scheffler, M.; Van de Walle, C. G. Sources of Electrical Conductivity in SnO_2. *Phys. Rev. Lett.* **2008**, *101* (5), 055502. https://doi.org/10.1103/PhysRevLett.101.055502.
(40) Kilb, E. P. *Literature Survey on Calcium Hydride*; General Electric, Atomic Products Division, 1959.
(41) Hayashi, K.; Hosono, H. Green Apatites: Hydride Ions, Electrons and Their Interconversion in the Crystallographic Channel. *Phys. Chem. Chem. Phys.* **2016**, *18* (11), 8186–8195. https://doi.org/10.1039/C6CP00515B.

Chapter 6

POSSIBLE HYDROGEN COUPLING TO K AND Na in DAVEMAOITE

The contents of this chapter are part of a manuscript in preparation titled "Investigation of possible hydrogen coupling to K and Na in Davemaoite" by W.R. Palfey, W.A. Goddard III, and G.R. Rossman. In this work, W.R. Palfey led the DFT calculations, supervised by both W.A. Goddard III and G.R. Rossman. All authors were involved in designing the study and preparation of the manuscript.

6.1 Introduction

The discovery of davemaoite, a Ca-Si perovskite from the lower mantle, was an important landmark in the study of the deep earth. As the first naturally occurring example of what is likely the mantle's third most abundant phase, the discovery confirmed the presence of a lower mantle Ca-Si perovskite, but also presented surprising details. Notably, this davemaoite inclusion's composition deviates significantly from the ideal formula of $CaSiO_3$, containing Al, Fe, Cr, Mg, and perhaps most significantly, high concentrations of K and Na[1]. Additionally, Rietveld refinement of the diffraction data of the davemaoite inclusion showed that virtually all impurity species occur as substitutions on the Ca site, rather than the Si site. Considering the presence of Al, Fe, and Cr (possible trivalent ions), the most straightforward method for incorporating these alkali species would appear to be through coupled substitutions involving multiple Ca sites, in the following manner:

$$2Ca_{Ca}^{\times} \rightarrow (K, Na)_{Ca}^{/} + (Al, Fe, Cr)_{Ca}^{\cdot}$$

Coupled substitutions of this sort are known to occur in a variety of mineral species, such as the substitution of Cr^{3+} and Nb^{5+} for two Ti^{4+} in rutile[2]. While coupled cation substitutions are likely in the davemaoite inclusion, the measured concentrations of K^+ and Na^+ exceeded the concentrations of all trivalent species, as can be gleaned from the measured formula: $(Ca_{0.43}K_{0.20}Na_{0.06}Fe_{0.11}Al_{0.08}Mg_{0.06}Cr_{0.04})SiO_3$ [1]. Thus, it is possible that native defects with a net positive charge may couple to the excess monovalent ions to

achieve balance. Likely among these are oxygen vacancies, to which two substituting ions could couple:

$$2Ca_{Ca}^{X} + O_{O}^{X} \rightarrow 2(K, Na)_{Ca}^{/} + v_{O}^{\cdot\cdot}$$

While this presents an attractive explanation to account for excess K and Na, the concentration of oxygen vacancies required would be exceptionally high — in the range of 0.03 to 0.18 formula units — possibly ruling out these vacancies as the sole charge compensating mechanism. However, there is yet another class of defects that could account for davemaoite's composition: hydrogen-based defects. Laser ablation inductively coupled plasma mass spectrometry (LA-ICP-MS), the method employed to obtain davemaoite's composition, cannot detect hydrogen directly. Additionally, hydrogen is not typically reliably detectable via X-ray diffraction. Thus, hydrogen could be present in this davemaoite specimen, or potentially alkali-rich davemaoite generally.

The most conventional manner by which K and Na could couple to hydrogen in davemaoite is via a coupled substitution mechanism, akin to those seen in rutile and stishovite, among other phases[3–5]:

$$Ca_{Ca}^{\times} \rightarrow (K, Na)_{Ca}^{/} + H_{i}^{\cdot}$$

where an interstitial H^+ ion (H_i) protonates an O atom, forming an OH^- group. In minerals that are particularly receptive to OH^- incorporation, this type of mechanism can incorporate 1000s of µg/g H_2O[2]. However, OH^- defects are not the only type of hydrogen defect known to occur in perovskite materials. Over the last 10-15 years, much work has been done synthesizing and characterizing hydride in oxide perovskites, especially those in the (Ca,Sr,Ba)TiO_3 composition series[6–9]. Studies thus far indicate that oxide perovskites can incorporate exceptionally high amounts of hydride, reaching even stochiometric levels, with 20% O-site occupation[7]. Notably, this series of phases includes cubic perovskites that are isostructural with davemaoite, like the $SrTiO_3$ endmember[6,10]. Although the incorporation mechanism for hydride in these materials occurs via a reduction of the tetravalent cation, Ti^{4+} (a pathway that is unlikely in a Si-based perovskite), other work has shown that hydride solubility in perovskites is also facilitated by substitution of lower valence cations, such as Sc^{3+} , Na^+, and possibly Fe^{2+} for Ti^{4+} [11–13]. In fact, these

mechanisms can increase hydride solubility even more than cation reduction, especially at elevated pressures[12]. Thus, the coupled substitution of alkalis and hydride could also be considered:

$$Ca_{Ca}^{X} \rightarrow (K, Na)_{Ca}^{/} + H_{O}^{\cdot}$$

where O^{2-} is directly replaced by H^-. If either OH^- or H^- accounts for the high alkali concentrations in davemaoite, then this phase could play a part in earth's hydrogen budget, altering the current model for hydration in the lower mantle. Additionally, the latter of these two defect types would be the first instance of hydride playing a significant role in hydrogen sequestration in the mantle's oxide phases.

In this study, we used density functional theory (DFT) calculations to explore the possibility of either OH^- or H^- defects coupling to Na and K in naturally occurring davemaoite. We present the energetics of these defects, their simulated infrared behaviors, and contextualize these results in the setting of laboratory measurements to comment on the prospect of hydrogen detection in alkali-rich davemaoite.

6.2 Methods

6.2.1 Computational details

All calculations were carried out using the Vienna Ab initio Simulation Package (VASP, version 6.2.1 16May21). The exchange correlation was described via the Perdew-Burke-Ernerhof (PBE) generalized gradient approximation, with D3 van Der Waals corrections[14–19]. For structural relaxations, the energy cutoff was set to 500 eV, and a 6×6×6 gamma-centered, Monkhorst-Pack mesh was found to be sufficient for the larger 3×3×3 supercell, while an 8×8×8 mesh was used for 2×2×2 supercells. Smearing near the Fermi level was modeled via the tetrahedron method with an 0.05 smearing width and Blöchl corrections[20]. A force minimization criterion of 0.01 eV/Å was used for all relaxations.

The 0 K phonon modes for the defect states were calculated through two different means: finite differences, and perturbation theory (DFPT). The former of these is well-suited for calculating the positions of specific vibrational modes in a computationally

inexpensive manner via implementation of selective dynamics, while the latter can be used to estimate the relative infrared intensities of all vibrational modes in the system via simultaneous calculation of the Born-effective charges. More specifically, this application of DFPT can be used to more directly compare the intensity of the native davemaoite infrared modes against hydrogen-associated ones. Finite difference calculations were carried out for hydrogen atoms in all assessed defect states, with a Γ-centered k-point grid set to a 6×6×6 density. In contrast, the more computationally expensive DFPT calculations were carried out using a single Γ-centered k-point and were only carried out for the lowest energy defect states. The infrared intensities were calculated from the DFPT results using a code developed by David Karhanek[21].

Quantum mechanics molecular dynamics (QM MD) was also carried out on select defect structures in the 2x2x2 supercell. For these calculations, only the smaller super cell was chosen due to the resource-intensive nature of 3x3x3 supercell calculations. In all simulations, the temperature was set to 300 K (equivalent to the measurement temperature from the Tschauner et al., 2021 paper)[1]. The simulation was carried out using a canonical (NVT) ensemble, where temperature was set via a Nose-Hoover thermostat. A Γ-centered 1x1x1 k-point grid was used. From the results of these calculations, we derived atom velocities, from which the velocity autocorrelation function (VACF) and phonon density of states (pDOS) were calculated via the 2 phase thermodynamics (2PT) code[22–24].

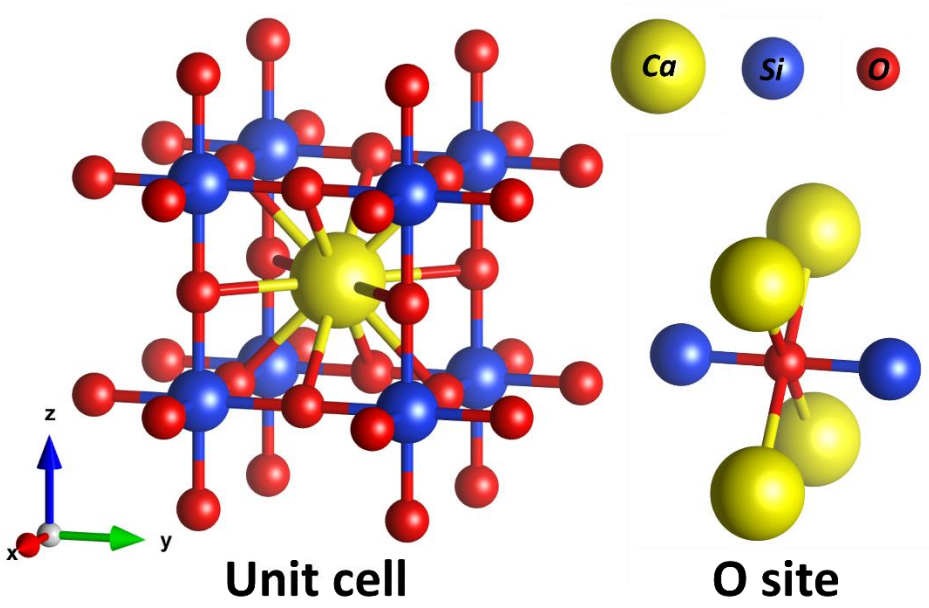

Figure 6.1 *– Structure of the defect-free davemaoite structure (left) and the isolated O site (right). As a cubic single perovskite, all Ca and Si sites have cubic symmetry and equivalent geometries. Oxygen equally coordinates to four Ca atoms in a square planar geometry and forms a linear bond between two Si atoms. All O sites are equivalent.*

6.2.2 Deriving the defect states

The number of symmetrically distinct possible defect states for both H^- and OH^- differed significantly between the 2×2×2 and 3×3×3 cell, with the latter presenting many more possibilities. This is because of the high symmetry of the davemaoite structure, including each of its individual cation sites. As a single ABO_3 type perovskite, davemaoite has the simplest possible unit cell for a perovskite phase. Within the unit cell, there are 12-coordinated Ca sites and 6-coordinated Si sites. In this high symmetry structure, every O^{2-} site that could be either protonated or substituted by H^- is symmetrically identical. Therefore, in the absence of a co-dopant (K^+ or Na^+) there is only one site for H^- and the possible nondegenerate OH^- groups that can form are extremely limited. However, in any cell size larger than a single unit cell, once Ca^{2+} is replaced, the oxygen sites in the supercell are no longer all symmetrically equivalent. For a 2×2×2 supercell, there are only two symmetrically distinct O sites relative to the substituted cation: one coordinated directly to

the substituted atom, and one that is not. In a 3×3×3 cell, these possibilities expand to include six distinct O^{2-} sites. For our derived defect states, we labeled each group of O sites based on its proximity to the substituting cation (denoted by subscripts A-F), with the O_A site being directly coordinated to K or Na. In the 2×2×2 cell, only O_A and O_B sites are possible.

Symmetrically distinct OH^- groups are distinguished not only by the O site they form from, but also the direction of the resulting O-H bond. Through preliminary testing, we found that OH^- tends to relax to directions pointing approximately parallel to *a*. Thus, we applied this limitation to our starting configurations. Depending upon the position of the O atom relative to the substituted cation, there may multiple unique directions that O-H can point, which we designate with a number (ex: OH^- group O_{A1} versus O_{D3}). This results in 4 possible OH^- groups in the 2×2×2 cell and 12 in the 3×3×3 cell for the K^+ and Na^+ cases each.

Because H^- tends to directly occupy the O^{2-} lattice site rather than occupying an interstitial site, there are comparatively few considerations for deriving possible defect states when compared to OH^-. However, we did perform some tests to see if H^- would deviate from this on-site occupation. This is because in the $BaTiO_3$ perovskite phase, there have been suggestions that hydride could also reside off of the O^{2-} site[25], and our prior work on $SrTiO_3$ in the prior showed that an offsite occupation could be stable under specific conditions. However, our testing of isolated defect states showed that these off-site occupations were not stable in davemaoite, at least for single pairs of H^- and K^+ or Na^+. Thus, there were only two and six H^- defect states to consider in the 2×2×2 and 3×3×3 supercells, respectively.

6.2.3 Assessing defect proportions

As previously discussed, hydrogen-related defects and monovalent-trivalent coupled substitutions act as counters to each other in the davemaoite system. In the absence of significant O^{2-} vacancy concentrations, K^+ and Na^+ could be incorporated via either hydrogen or trivalent cations. Thus, the theoretical concentration of hydrogen defects in

natural davemaoite is limited by the concentration of trivalent ions. This is an important consideration for making comparisons to the existing experimental infrared data, as is discussed in more detail later. Cations with possible trivalent states include Al, Fe and Cr. While Al is almost certainly present as Al^{3+}, Fe, and Cr can be either tri- or divalent, complicating this consideration. We therefore consider two possibilities: an oxidized case where only Fe^{3+} and Cr^{3+} are stable, and a reduced case where only Fe^{2+} and Cr^{2+} are stable. For the former case, the excess quantity of K^+ and Na^+ is: [K + Na] – [Al + Fe + Cr] = 0.03 moles per formula unit, while for the latter it is: [K + Na] – [Al] = 0.18 moles per formula unit. We consider these excess alkali concentrations as the upper limit for hydrogen concentrations in each redox state.

The next consideration is whether hydrogen defects and trivalent cations couple preferentially to K^+ or Na^+. For both the oxidized and reduced cases, it is possible that the trivalent cations could: *a)* couple to Na^+ first, leaving a higher proportion of K-based hydrogen defects, *b)* couple to K^+ first, leaving a higher proportion of Na-based hydrogen defects, or *c)* couple to K^+ and Na^+ equally, leaving hydrogen to be equally proportioned between K and Na. These scenarios can be considered as two endmembers with scenario *c)* as an intermediate state. Combining these three possibilities with the prior oxidized and reduced cases results in six evaluated states for hydrogen defects, summarized in Table 6.1.

	Formula units H, oxidized case	**Formula units H, reduced case**
M^{3+} couples to Na^+ first	0.03 coupled to K	0.18 coupled to K
M^{3+} couples to K^+ first	0.03 coupled to Na	0.12 coupled to K, 0.06 coupled to Na
M^{3+} couples without preference	0.023 coupled to K, 0.007 coupled to Na	0.138 coupled to K, 0.042 coupled to Na

Table 6.1 *– Summary of the possible abundances of H defects (in formula units) depending upon Na/K coupling preferences and the oxidation states of other substituted cations.*

For simplicity, we assumed equal partitioning between Na and K for hydrogen defects. H^- is assumed to be stable only under highly reducing conditions, so the reduced

case represents an upper bound on possible formula units of H^- (0.18). OH^- could also be stable under somewhat reduced conditions where Fe and Cr are divalent, so we also considered the same upper limit for OH^- incorporation.

6.3 Results and Discussion

We found that the two supercell sizes produced slightly different results for structural minimization. Therefore, we present our findings in the context of each cell size, beginning with the 2×2×2 cell.

6.3.1 Structural minimizations – the 2×2×2 supercell

OH^- groups in the 2×2×2 supercell have a definite energetic preference to locate close to the co-substituting cation, although there are significant differences between the K and Na cases. For K, the preference is relatively modest, on the order of 47 to 98 meV, while the preference in Na-based defects is extremely strong, 410 to 450 meV. Despite the limited number of configurations, it is also clear that OH^- placements become less energetically favorable the further they are from either K or Na. Ultimately, these energy differences mean that at room temperature, only a single structurally distinct OH^- group is likely to be associated with Na, while in the case of K, there could be a secondary, less dominant population of OH^- groups.

Relaxations of H^- substituted structures resulted in a much less clear-cut picture. For each defect case, the energetic differences between the two possibilities were relatively small: 11 meV between the two K defect structures and 24 meV between the Na structures. This result implies significant populations of defects in both states. In addition, the K- and Na-based defects showed different preferences for proximity; H^- preferred coordination only to Ca in the K case, while H^- preferred coordination to Na in the Na case. Regardless, having only two possible test configurations significantly limits what systematic behaviors for H^- can be learned from these calculations. This was one of the primary motivators we had for performing additional calculations in an expanded supercell. Even though the molar

proportions of K, Na and H are closer to the formula values of the davemaoite inclusion in the 2×2×2 cell, the limited number of possible structures in this smaller cell makes it hard to discern broader trends for H incorporation. Additionally, results from this supercell size carry inherent errors such as artificial defect ordering that likely influence the results of these calculations significantly. Accommodation of the H^- ion by the surrounding lattice was also limited.

6.3.2 Structural minimizations – the 3×3×3 supercell

For both the Na- and K-substituting cases, we find that the most favorable interstitial site for OH-forming hydrogen in the 3×3×3 supercell is the one closest to the substituting cation. In the case of Na, the energetic preference for this closest site (O_{A1}) is extremely high (the next lowest energy defect state has an energy ~290 meV higher), while the energy preference for the K substitution is comparatively more modest, but still significant (~80 meV difference). The energetic preference between the lowest and next lowest energy configurations for K was increased slightly compared to the 2×2×2 supercell and weakened for Na (although in the case of Na, both differences in energy are so high that this difference is insignificant). As H occupies interstitial sites further and further away from the substituted cation, the potential energy of the structure eventually converges to a stable value (Figure 6.3).

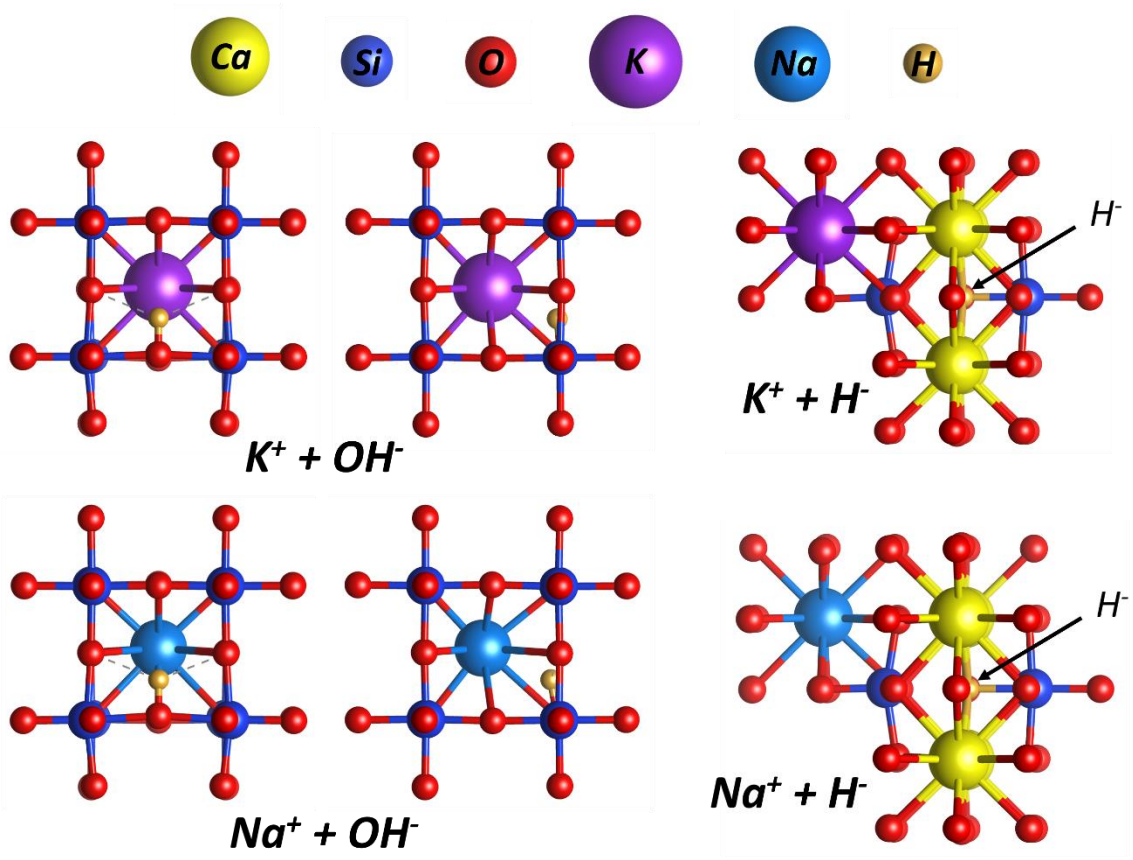

FIGURE 6.2 *– Results of relaxation for the lowest energy defect configurations in the 3x3x3 supercell. K-coupled defects are in the top row, while Na-coupled defects are on the bottom. OH^- defects are shown in two views. The substituted cation tends to deflect away from the OH^- group, an effect that is more pronounced for Na than K. For the H^- defects (which are both the O_B occupations), the adjacent substituted cation is also shown for reference. H^- appears to bond more closely to one Si than the other, moving away from K/Na. Distortion of the two Si octahedra occurs where both Si atoms are pushed away from the O site position.*

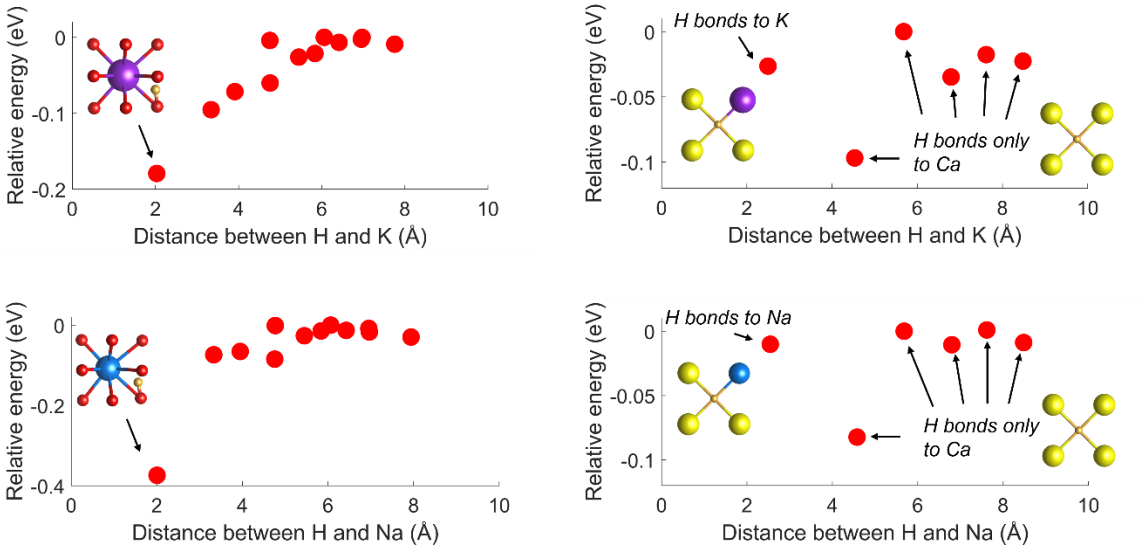

FIGURE 6.3 *– Plots showing the energetic preferences for H^- and OH^- placements in the 3×3×3 supercell relative to a substituted K^+ (top row) or Na^+ (bottom). The "Relative energy" is in relation to the highest energy defect, so that the lowest energy (most favorable) defect plots as the most negative. In the case of OH^- incorporation (left column), there is a clear inclination for H to be as close to the substituting cation as possible, a tendency which should be significantly stronger for Na than K. There is also a gradient of increasing energies as H is moved away from Na^+ or K^+, which appears to level off near ~5 Å for both cases. For cases of H^- incorporation (right column), hydrogen prefers to bond only to Ca while otherwise being as close to K^+ or Na^+ as possible. Direct bonding of H^- to K^+ or Na^+ is no more favorable than placements very far from K^+ or Na^+.*

Models of the local environment around each lowest-energy OH^- group configuration are presented in Figure 6.2. For both K and Na substitutions, the position of the substituted ion is deflected away from the Ca site, causing a distortion of the 12-coordinated site and significantly reducing local site symmetry. When K^+ is substituted, the resulting hydrogen bonding length (d(O…O)) as measured between the O atom of the OH^- and the O atom closest to H along the O-H bond length is 3.58 Å, with a K-O-H bond angle of 41.8°. In the case of Na^+ substitution, d(O…O) is 3.48 Å, while the Na-O-H bond angle is 38.0°. Based on these d(O...O) values, the two cases should produce two slightly separated vibrational modes with relatively high wavenumbers in the OH^- stretching range[26].

The relaxations of the H^- defects produced more systematic results than in the 2×2×2 cell. In both the Na- and K-substituting cases, we find that H prefers bonding exclusively to Ca atoms, rather than either Na or K. However, there is still a preference for H^- to reside as close as possible to either Na or K, while still being only bonded to Ca. The energy difference between the lowest and next lowest energy states is 62 meV for the K substitution and 72 meV for the Na substitution. For all minimized H^- defect states, there is a slight deflection of the adjacent Si atoms away from the substituted H^- ion. H^- on the B site has approximately equant bond lengths to all four Ca atoms (differences are on the order of 0.01 Å) while being biased in the direction away from either K or Na. When H^- does bond to the substituted cation, it bonds more closely to K or Na than Ca by 0.18 Å for K and 0.05 Å for Na. Overall, structural distortion in the 3×3×3 cell is localized to the vicinity of H^-. This is in contrast to the 2×2×2 supercell, where the limited cell volume means that virtually the entire structure is dominated by distorted sites, resulting in a more dramatic departure from the experimentally measured davemaoite structure.

One possibility for the energetic preference for hydride to bond only to Ca is the higher site symmetry compared to direct K or Na bonding. If the large break in O site symmetry is the origin of a Ca-only bonding preference for H^-, then there could still be alternate configurations where bonding directly to the substituted cation maintains a cubic (or somewhat lower) symmetry and becomes more favorable. However, this can only be accomplished through a larger cluster of defects encompassing several Ca sites, so we have chosen not to investigate this possibility here.

Overall, we regard the defect states in the 3×3×3 cell as more representative of individual OH^- or H^- defect behavior because they are free from unavoidable effects resulting from a smaller supercell (i.e., heavy structural distortion and unintentional defect ordering that are more akin to ‘networks’ or ‘clusters’ of defects). The smaller cell may be closer in H concentration to the maximum possible concentration in the natural davemaoite (0.125 formula units in the 2×2×2 supercell), but the effect of a small cell probably makes these results less instructive for understanding the general behavior of H^- and OH^-, especially across a range of concentrations. Additionally, if hydrogen incorporation is favorable in alkali-rich davemaoite, then it is probably more likely to occur in lower

concentrations. Nevertheless, we still present the phonon and QM-MD results from the smaller supercell, as they may still be generally instructive in illustrating the effects of high defect concentration, albeit with the caveats presented above.

6.3.3 Finite differences and QM-MD – the 2×2×2 supercell

Analyses of the vibrational modes of H in the 2×2×2 cell were carried out using both finite differences and QM-MD. For the OH-based defects, only the lowest energy defect structures were considered, as the energetic preferences for these configurations were clear cut. For the hydride-containing structures, we considered both defect positions, both because of the less conclusive energetics, and to analyze the effect of bonding to K and Na on the frequencies of hydride vibrations. The results of these calculations are presented in Table 6.2. These calculations predict a set of two OH^- modes centered at 3420.6 cm^{-1} and 3125.3 cm^{-1} for the K- and Na-coupled defects, respectively. For the H^- defect states, all the predicted modes fall within the range of ~1000 to 1200 cm^{-1}.

Defect – OH^-	**O-H stretch (ω_1) (cm^{-1})**	**M-O-H bend (ω_2) (cm^{-1})**
K, site O_{A1}	3420.6	1316.8
Na, site O_{A1}	3125.3	1313.5

Defect – H^-	**Si-H-Si stretch (cm^{-1})**	**Si-H-Si bend (cm^{-1})**	**Si-H-Si bend (cm^{-1})**
K, site O_A	1195.5	1067.0	1080.9
K, site O_B	1110.2	1103.7	1080.9
Na, site O_A	1090.3	1080.2	994.6
Na, site O_B	1115.3	1089.6	1021.7

Table 6.2 *– Hydrogen mode positions calculated from finite differences in the 2x2x supercell. For OH-, the lowest energy defect results are presented (position O_{A1}), while for H^-, all four cases were calculated.*

The vibrational densities of states from the 300 K QM-MD simulations of the same six defect states are presented in Figure 6.4, alongside the finite differences results. For the hydroxyl defects, a predicted O-H stretching mode and corresponding bending mode are

clearly present. There is general agreement between the 0 K predicted O-H stretching modes and the equivalent vibrational densities, although the finite differences method estimates slightly lower energies. This is indicative of a possible temperature or pressure effect (or a combination of the two). For both the K- and Na-coupled defects, the DOS indicates the possibility of more than one O-H stretching mode. In the case of K substitution, a prominent major peak is predicted with a substantially lower intensity minor peak at higher wavenumbers. Meanwhile, the Na-substituted structure produces a broader distribution for the O-H stretch with possibly two resolvable peaks that have more similar associated densities. Splitting effects like this could be indicative of proton dynamics (i.e., hydrogen bond "hopping" between different O atoms). For a density profile like the one predicted for the Na-coupled OH^- group, this may result in a broader, more difficult to detect series of modes that also resembles multiple defect states.

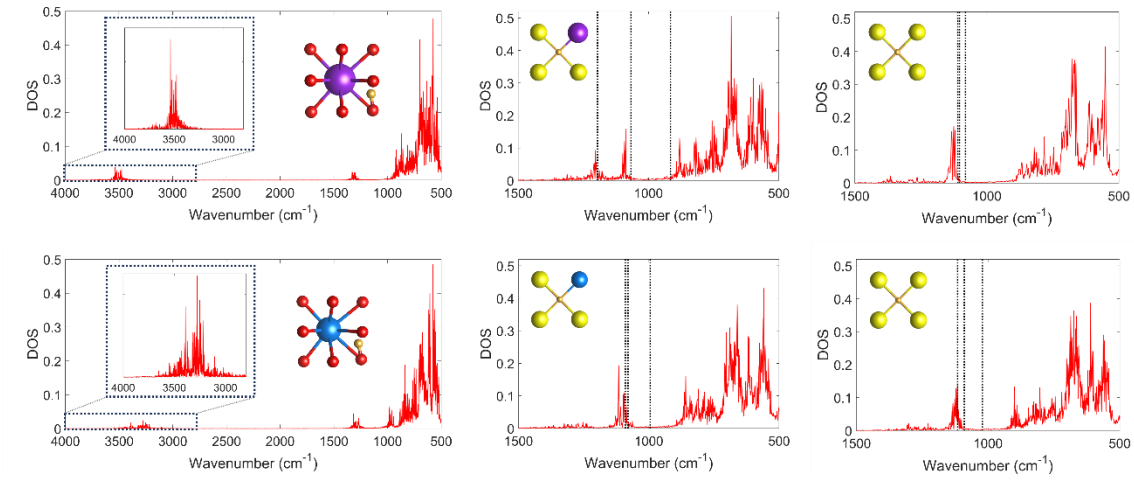

FIGURE 6.4 *– Compilation of the vibrational density of states for each of the defects simulated via QM-MD in the 2x2x2 supercell. The top row consists of all of the K-coupled defects, while the bottom row consists of the Na-coupled defects. The left column contains spectra that result from the formation of the most energetically stable OH^- group, the O_{A1} case. For the four hydride cases, the positions of the corresponding 0 K modes calculated via finite differences from Table 6.2 are plotted with vertical dotted lines. The two spectra from the center column correspond to hydride bonding to the substituted alkali cation, while the rightmost column contains the more favorable Ca-only hydride bonding scenario. Differences between the 0 K positions and the phonon densities are likely due to temperature effects; this generally seems to push vibrations to higher cm^{-1} positions.*

0 K calculations for the H^- defects and the corresponding QM-MD results show slight discrepancies, similar to the OH^- defects. Although overlaps between the Si-H-Si stretch calculated via finite differences and the vDOS tend to have close agreement, the 0 K position of the lower energy bending mode tends not to line up with the vDOS. Like with the OH^- modes, this could simply be a predicted effect of temperature, which can cause the positions of modes to shift. Generally, bands associated with H^- are predicted to be fairly prominent, and therefore easier to detect. (This contrasts with the distribution of modes predicted for O-H stretching in the Na-OH substitution, for example.) At higher wavenumber positions from the primary H^- mode densities, a much broader, lower density is predicted, but the precise origin of this density (i.e. what motion exactly that it corresponds to) is not known. However, regardless of how broad or sharp the QM-MD results predict these modes to be, nearly all of them overlap with the features of diamond (between ~1100 and 1350 cm^{-1}), potentially presenting problems for detection in natural, diamond inclusion hosted samples, or diamond anvil cell experiments.

6.3.4 DFPT – the 3×3×3 supercell

Perturbation theory calculations carried on a 3×3×3 supercell of pristine, cubic davemaoite indicate that only three infrared-active modes, centered at 221 cm^{-1}, 393 cm^{-1}, and 706 $cm^{-1,}$ should be present. The latter of these three modes is an O-atom dominated, asymmetric stretching mode with motions oriented along the principal axes of the octahedral SiO_6 sites (Figure 6.5). Owing to davemaoite's cubic geometry, the mode at 706 cm^{-1} consists of three overlapping degenerate modes, each polarized to *a*, *b* or *c*. Local structural perturbation of oxygen sites in the high symmetry davemaoite structure (discussed below) can easily remove this symmetric degeneracy, which leads to a partial broadening or splitting of this feature. Our calculated 706 cm^{-1} feature is equivalent to the ~720 cm^{-1} mode observed by Tschauner et al., 2021 in natural davemaoite[1]; the only IR-active normal mode visible in typically measured infrared ranges. This result is also roughly consistent with prior calculations adapted to davemaoite's cubic structure[1,27].

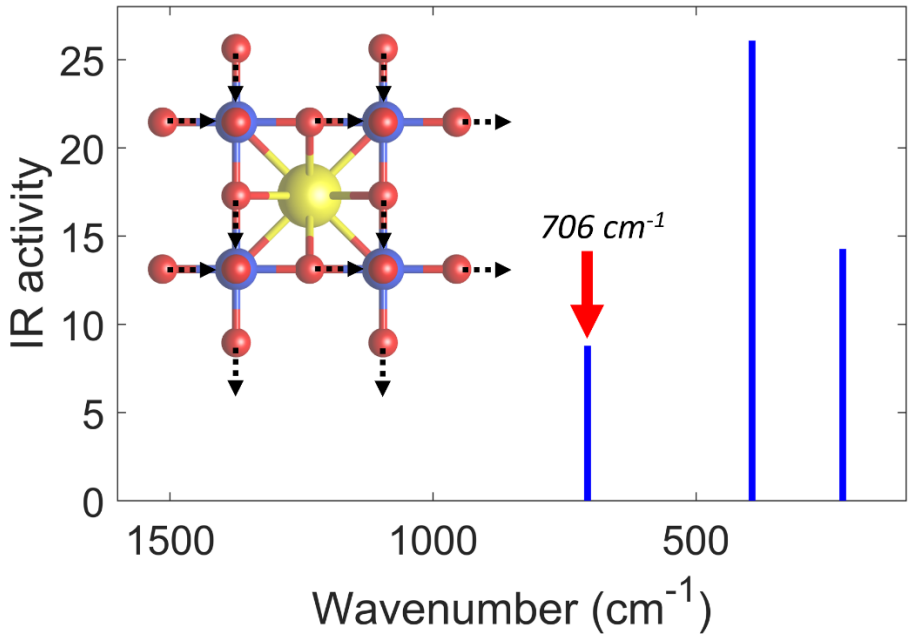

FIGURE 6.5 *– DFPT results for the pristine 3×3×3 davemaoite supercell. There should only be one IR-active mode within the typically measured range (above ~650 cm^{-1}). This corresponds to an asymmetric Si-O-Si stretching mode, which we predict to occur at 706 cm^{-1}. Note that the bar presented in this plot for the 706 cm^{-1} represents the intensity of just one of the three degenerate components of this vibration.*

O-H stretching modes in the 3×3×3 supercell are predicted to occur at higher wavenumber positions than their counterparts in the 2×2×2 supercell, while bending modes are predicted to occur at lower wavenumber positions. When OH^- couples to K^+, the resulting stretching and bending modes occur at 3604 cm^{-1} and 1128 cm^{-1}, respectively. Distortion of the surrounding lattice perturbs the 706 cm^{-1} mode, resulting in additional IR-active modes up to ~100 cm^{-1} higher. In the case of Na^+ substitution, the OH^- modes are located at 3579 cm^{-1} and 1062 cm^{-1}, and additional modes above 706 cm^{-1} emerge as a consequence of structural distortion. Plots showing the positions of these features weighted to their corresponding infrared activities can be seen in Figure 6.6.

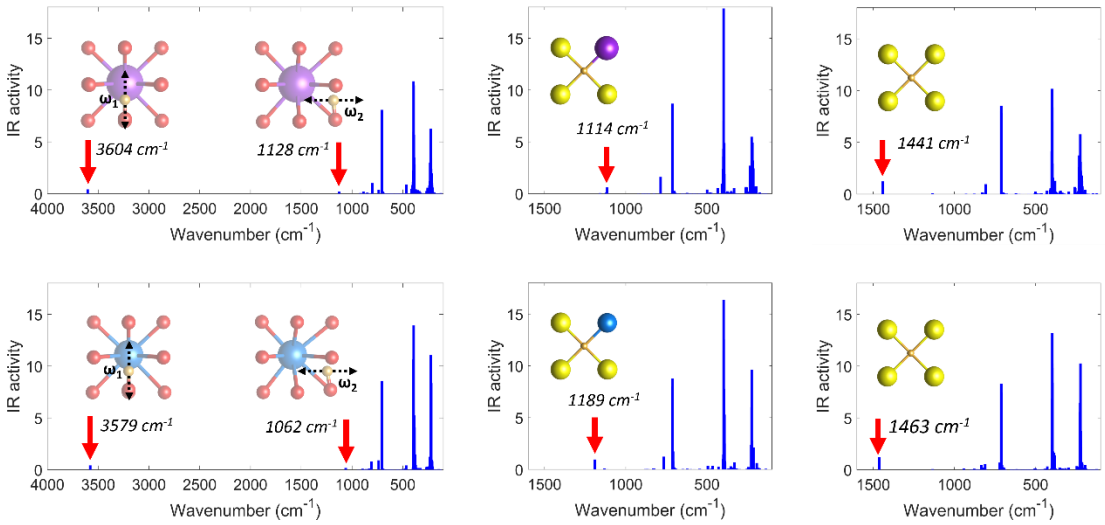

FIGURE 6.6 *– DFPT results for H^- and OH^- defects coupled to K^+ incorporation (top) and Na^+ incorporation (bottom) in the 3×3×3 supercell. The positions of the calculated normal modes are presented and scaled to their relative infrared intensities. The leftmost column contains the DFPT results for the most energetically favorable OH^- defects. Both the O-H stretching mode and the most infrared active bending mode (ω_1 and ω_2) are highlighted with red arrows. In the right two columns, the results from two hydride bonding scenarios are presented: O_A (coordinated directly to K/Na) and O_B (coordinated only to Ca). In all four instances, the Si-H-Si stretching mode is highlighted with a red arrow.*

The positions of H^- bands similarly differ between the 2×2×2 and 3×3×3 supercells. For the lowest energy defects (oxygen site "B" occupation), the Si-H-Si stretching modes lie at positions over 300 cm^{-1} higher for the expanded supercell (1441 cm^{-1} for K substitution and 1463 cm^{-1} for Na substitution). Meanwhile, the predicted Si-H-Si frequencies for defects with direct K-H and Na-H bonding are very similar between the two cell sizes. Much like with the OH^- defects, a portion of the 706 cm^{-1} mode is predicted to shift to a slightly high wavenumber in response to structural distortion resulting form the incorporation of K, Na and H^-. The infrared activities of the Si-H-Si stretching modes are predicted to be between 1.5 to 3 times as high as the calculated O-H stretching modes. This, coupled with the predicted positions of modes associated with the most energetically favorable defect, makes detection of H^- more likely.

6.3.5 Comparisons to measurement

Detection of hydrogen in a natural specimen of davemaoite may prove difficult for a variety of reasons. First, is the factor of being non-quenchable. Because calcium silicate perovskites cannot be quenched, intact examples are few (limited only to one example for now) and can only be observed as diamond inclusions. This latter point also means that samples will tend to be quite small (possibly making collection of high-quality spectra difficult) and that infrared spectra must be taken that include a significant signal from the surrounding diamond. These factors mean that spectra taken of davemaoite will be superimposed onto comparatively more intense diamond spectra and will likely have a nonideal signal to noise ratio. This was the case for the spectrum taken by Tschauner et al. (2021), where the ~720 cm^{-1} davemaoite vibrational mode was significantly weaker than the coexisting IR features of diamond[1]. It is because of these complicating factors that we have tried to consider our results in the context of experimental conditions.

Four factors will determine whether our proposed H-related vibrational modes could be visible in a real measurement. First, is the position of the modes. As just mentioned, one of the main barriers to H detection could be the presence of intense diamond features. Modes located in the same region as these diamond features will probably need to be fairly intense to detect. This factor is mostly in play for H^-, as O-H stretching modes occur well outside the bounds of interference from diamond modes. Second and third are the infrared activities and relative abundances of the associated defects. Fourth, is the line shape of the mode (i.e., whether the infrared band is thin and sharp, wide and low, or somewhere in between). This final factor can have a potentially large influence on feature detection, as even defects with relatively high associated infrared activities have the potential to be obscured by signal noise if they have a broad shape. We developed compilation spectra based on our DFT results and available experimental data that account for these factors, a process we detail below.

The DFPT results from the 3×3×3 supercell were used to set the mode positions for H^-, OH^-, and pristine davemaoite. As mentioned previously, although the 2×2×2 supercell may be closer to the maximum possible H defect concentrations, the results of those calculations were probably influenced by the extreme structural distortion imposed on the

lattice by confining the defects to a small volume. Alternate configurations that represent equivalent concentrations of defects could be constructed to reduce distortion, but in the 2×2×2 cell (where there are only two unique O sites), these cannot be tested. Thus, we have assumed that isolating defects in the expanded supercell will produce more representative spectral behavior for a range of H concentrations. These same DFPT results were also used to set the infrared activities of the defect modes.

We considered several possibilities for fixing the line shapes of the simulated defect features. Initially, we intended to use the vDOS distributions calculated from the QM-MD simulations. However, the general divergence between the mode positions between the two supercell sizes (which is probably due in part to the factors related to cell size detailed above) led us to choose other options. For setting the shapes of the O-H stretching modes, we looked to prior experimental work on perovskites. Prior experimental studies observed possible OH^- modes in $CaSiO_3$, and these modes had a broad line shape[28]. Despite this, these modes were identified in a pure (no dopant) $CaSiO_3$ composition, implying that they were a consequence of OH^- coupling to cation vacancies. This should result in a fundamentally different hydrogen bonding environment than the coupled substitution mechanisms we present above, so we opted for a different approach. In our prior work on $SrTiO_3$, we had observed an OH^- stretching mode at 3500 cm^{-1} in the pristine starting material, which has been previously observed[29]. Given the structural similarities between davemaoite and $SrTiO_3$, and the similar mode positions (which could imply a similar hydrogen bonding environment), we fixed the widths of our OH^- modes to this feature. Assigning a width to the primary H^- mode was comparatively simple, as we assigned it the same shape as the only recorded IR mode for H^- in perovskite — the 1308 cm^{-1} mode from our prior $SrTiO_3$ work. Lastly, the shifted and unshifted asymmetric Si-O-Si modes around 706 cm^{-1} were assigned the same line shape as the ~720 cm^{-1} feature from Tschauner et al. (2021).

We simulated two cases for defect concentrations: one with 0.02 H per formula unit, and one with 0.18 H per formula unit. These two values correspond to approximately 0.155 to 0.156 wt% H_2O and 1.40 to 1.44 wt% H_2O, with the former representing a significant, but not extremely high H solubility, and the latter representing a virtually

complete coupling of alkali species to H in a composition equivalent to Tschauner et al.'s specimen (note that the mass fractions are ranges due to oxygen loss in the case of hydride incorporation). Our choice of partitioning H between either K or Na was simple; rather than iterate through the possible preferences for K or Na to couple to H, we opted for H concentrations to be directly proportional to the K and Na concentrations measured in the natural davemaoite sample. Simulated spectral features were proportioned relative to H defect concentrations, which included proportional reductions of the native 706 cm^{-1} Si-O-Si mode corresponding to the emergence of higher wavenumber features tied to structural distortion. Finally, after being scaled to IR intensity, H concentration and Na/K ratios, the spectra were scaled in proportion to the data from Tschauner et al. (2021) by matching the integrated intensities of the simulated 706 cm^{-1} features with the measured ~720 cm^{-1} feature. The results are plotted against this experimental data in Figure 6.7.

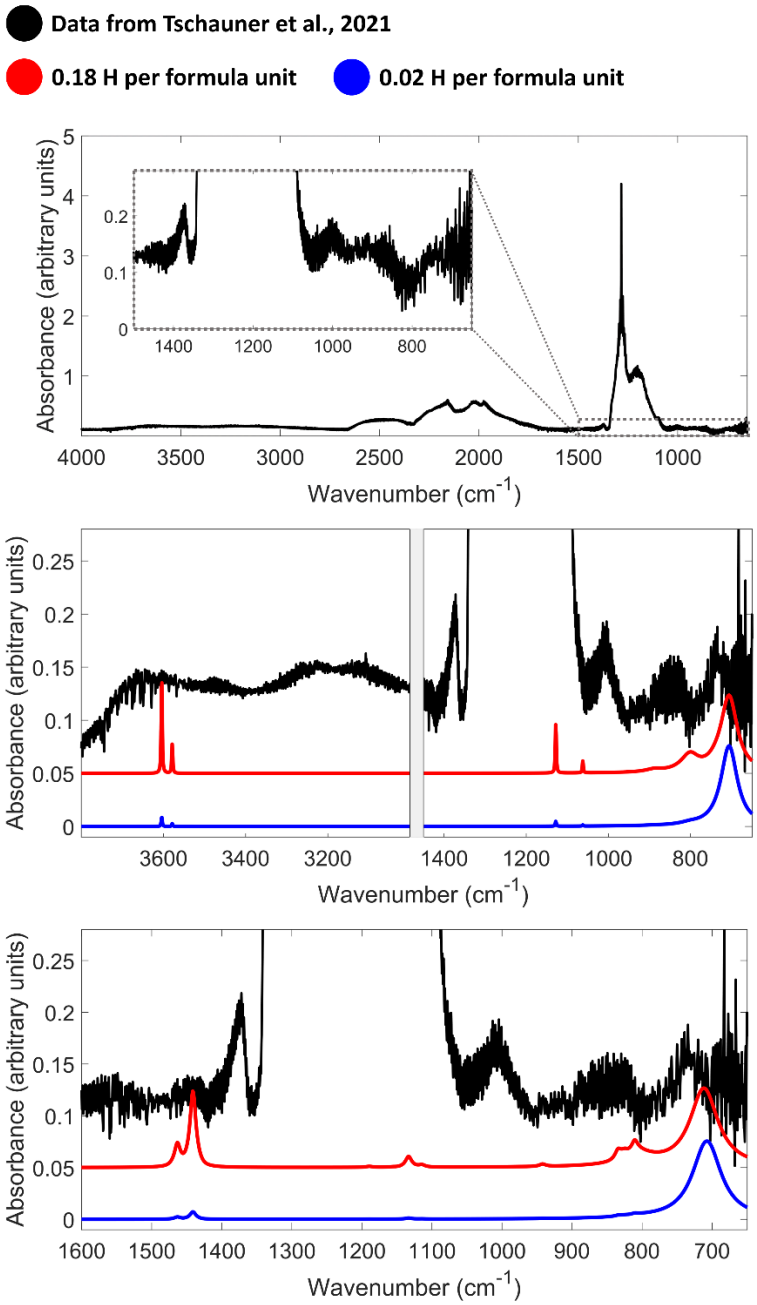

FIGURE 6.7 *– The spectrum of diamond from Tschauner et al. (2021) (top) simulated spectra for OH^- defects (middle) and H^- defects (bottom) coupled to both K and Na in davemaoite, presented in comparison to the davemaoite spectrum from Tschauner et al. (2021). For both OH^- and H^-, the most infrared active components of the spectra should be in ranges that make detection potentially feasible. However, outside of high H concentrations, detection may be difficult due to interference from noise and spectral artifacts. Note that although the Si-H-Si stretched around 1450 cm^{-1} seem to line up with a feature in the experimental spectrum, our analysis of this data leads us to believe the feature is most likely an artifact, like an interference fringe.*

6.3.6 Is it possible to see either OH^- or H^- in an inclusion?

When compared against the infrared spectrum for naturally occurring davemaoite, our simulated spectra show that hydrogen may be detectable, but possibly only under certain circumstances. In the case of hydroxyl groups, our predicted stretching modes are located far away from most spectral features that could provide interference, as is typical in other phases. Indeed, even if our calculated modes demonstrated discrepancies on the order of 100s of cm^{-1} from experiment, there would still be no doubt as to their identities as OH^-. Under similar measurement conditions, high concentrations of OH^- (equivalent to low wt% levels of H_2O) should be easy to detect, as indicated by the model spectrum corresponding to 0.18 formula units H. However, it is important to remember that this concentration of OH^- would be exceptionally high and is not typical among most nominally anhydrous minerals. The OH stretching modes of the 0.02 formula unit model, which represents a more plausible concentration of H, could possibly still be detected, although their intensities are beginning to approach an intensity similar to the noise. Concentrations below this point might not be easily detected at all. Additionally, we emphasize that the line shape chosen for the OH modes in this model were quite thin and prominent, essentially providing a best-case scenario for detection. Broader shaped features, more akin to our QM-MD results for Na coupled OH for example, would present a greater challenge for OH^- detection.

The projected visibility of H^- modes is aided by their predicted infrared activities; the most abundant defect configurations should produce IR features about three times as intense as their OH^- counterparts. This is reflected by the prominence of these features in the modeled spectra. However, for the 0.02 formula unit spectrum, the intensities of the H^- bands are sufficiently low that they could easily be lost in the noise of the experimental spectrum. Given that H^- can be present in oxide perovskites at stoichiometric levels[6,11], it could be possible for hydride concentrations could reach a level where they would be easily detectible. The positions of the H^- modes are generally advantageous for detection; they are completely outside of the strong diamond absorption region and are just offset from the nitrogen-based defect feature centered just below 1400 cm^{-1}. Nonetheless, although we have decided that the band positions and intensities from the 3×3×3 supercell are

representative, it should be recalled that the 2×2×2 supercell band positions differed significantly. In the smaller cell, modes are predicted to cluster near the 1100 to 1200 cm^{-1} range, directly beneath the diamond features. While we attributed these shifts in position to a severe and possibly unrealistic structural distortion, it is not clear from our calculations whether similar mode shifts would still occur when H^- and K/Na concentrations are greatly increased while allowing defects to rearrange to lower energy configurations. Thus, while our best estimates place H^- modes within a spectral range with relatively high transmission, it is still possible that these features could be lost under far more intense diamond absorptions. These uncertainties surrounding the location of H^- modes emphasize the necessity of identifying H^- via infrared in controlled experiments before such modes can be identified in natural davemaoite.

6.3.7 Feasibility of Na and K coupling to H

Coupled substitutions are common in a few mantle phases like stishovite and rutile[4,5]. However, Chen et al. (2019) found that at least one such mechanism involving Al^{3+} is not favorable in davemaoite, with hydrogen partitioning into δ-AlOOH instead[28]. This rules out at least one possible mechanism that had previously been proven in silicates. However, Liu et al. (2019) did find that under high pressure, water-rich conditions, basaltic starting materials can produce Ca perovskites with highly variable compositions and measurable oxide deficits[30]. These could be indicative of coupled substitutions to significant quantities of OH^-, as is the case for electron microprobe analyses of phases with stoichiometric hydroxyl. Therefore, the possibility for H-coupled substitutions involving the many other possible dopants in davemaoite could still prove to be viable. With respect to an alkali-containing davemaoite, *in-situ* high pressure experiments probing the solubility of K and Na in davemaoite and the effect of hydrogen on these solubilities would need to be carried out to determine if these coupled substitution mechanisms are valid.

One question regarding the feasibility of hydride in davemaoite is the source of highly reduced hydrogen. In laboratory settings, transition metal perovskites are shown to readily react with hydride salts to incorporate hydride[7,31]. In synthetic hydroxyapatite, hydride incorporation has been accomplished either through a reaction with TiH_2 or Ti

metal, resulting in a corresponding decrease in hydroxyl[32,33]. This latter case suggests that, in addition to hydride compounds acting as a source for hydride in oxides, the presence of hydride-free reduced metals can also reduce preexisting OH^- to form H^- in oxides. Therefore, there are a few possible pathways for hydride incorporation in alkali-rich davemaoite. One is the reaction between either an oxygen vacancy- or hydroxyl-containing, alkali-rich davemaoite and FeH_x, which is stable at lower mantle conditions[34]. This reaction would be effectively equivalent to the hydride salt reactions performed on transition metal perovskites. Similalrly, OH-containing, alkali-rich davemaoite could react with Fe^0, akin to the hydroxyapatite-Ti metal reaction. In either case, not much is known yet about alkali-rich davemaoite, and these types of reactions could be the subject of future investigations.

6.3.8 Possible alternative defect states

These K- and Na-coupled defects that we have proposed here are just a few of many potential mechanisms for hydrogen incorporation in davemaoite and other deep earth perovskites. Although the davemaoite inclusion's high alkali content represents the only structurally intact davemaoite specimen to date, its composition is almost certainly not representative of all mantle davemaoite compositions. More likely, davemaoite serves as a "garbage can", incorporating many impurities, potentially allowing for many possible H-based defects. For example, synthetically produced Ca-Si perovskites can incorporate Ti up to stoichiometric concentrations[35]. Although no non-inverted natural examples of a Ti-rich davemaoite specimen have been recorded, the existence of this composition in the lower mantle is supported by measurements of Ti-rich diamond inclusion materials that are likely to be products of inverted davemaoite[36]. A significant Ti component to mantle davemaoite would provide yet another pathway for H incorporation in the form of OH^- and H^-. This could be accomplished via reduction of Ti^{4+} to Ti^{3+}, as occurs in the $(Ca,Sr,Ba)TiO_3$ family of perovskites[6].

6.3.9 Detecting hydride in mantle phases

Although our calculations predict that hydride could be observed in future alkali-rich davemaoite inclusions, the detection of hydride in non-quenchable diamond inclusion phases probably presents a technical challenge. Commonly, the positions of H^- modes overlap directly or partially with either intense primary diamond features, or those related to common diamond dopants (i.e., nitrogen). For example, our prior work on $SrTiO_3$ identified a mode at 1308 cm^{-1} that would be obscured by the ~1050 to 1350 cm^{-1} diamond features. Other examples include a hydride mode in $BaTiO_3$ centered at 1032 cm^{-1} and hydride in MgO, which produces vibrational modes between 1024 and 1053 cm^{-1}. This is not to mention the fact that features in the typical H^- vibrational region (below 1500 cm^{-1}) can often just as easily be ascribed to fundamentals and overtones of native vibrations or other defect states, the vast majority of which are poorly characterized. If H^- is to be detected in a davemaoite inclusion, there needs to be significant confidence in mode position and shape, which will probably result from future calculations and experiments on a variety of davemaoite compositions.

6.4 Conclusions

We have proposed hydrogen-based defects that could account for the high alkali content of natural davemaoite. Our first-principles calculations provide the structures of the resulting defect states, and their expected spectroscopic signatures. For OH^- defects coupled to both Na and K, we predict that only a single OH^- stretching mode should result, and these modes should be in the upper range of the typical O-H stretching region. For H^- coupled to Na and K, it is potentially less clear. Our best predictions place the most IR-active signals for H^- just outside of the range of interference from intense diamond signals, but there is a possibility that these H^- modes could still be obscured.

While we predict that the presence of very large concentrations of K- or Na-coupled hydrogen in the form of OH^- or H^- will be highly visible via IR spectroscopy, significant concentrations in the range of 1000s of μg/g may be easy to overlook. Future experiments exploring the possibility of alkali-hydrogen coupling could clarify whether the mechanisms

we have outlined are truly viable in davemaoite, and if so, what spectral features they produce. If a high solubility of OH^- or H^- is found for davemaoite, then this could place davemaoite in focus as a major component of the deep earth hydrogen cycle. Additionally, if davemaoite can incorporate large quantities of H^- in the same manner as Ti-based perovskites, then this raises the possibility of significant and yet-to-be-considered reservoirs for hydrogen in the deep earth.

References

(1) Tschauner, O.; Huang, S.; Yang, S.; Humayun, M.; Liu, W.; Gilbert Corder, S. N.; Bechtel, H. A.; Tischler, J.; Rossman, G. R. Discovery of Davemaoite, $CaSiO_3$ - Perovskite, as a Mineral from the Lower Mantle. *Science* **2021**, *374* (6569), 891–894. https://doi.org/10.1126/science.abl8568.

(2) Vlassopoulos, D.; Rossman, G. R.; Haggerty, S. Coupled Substitution of H and Minor Elements in Rutile and the Implications of High OH Contents in Nb- and Cr-Rich Rutile from the Upper Mantle. *American Mineralogist* **1993**, *78* (11–12), 1181–1191.

(3) Pawley, A. R.; McMillan, P. F.; Holloway, J. R. Hydrogen in Stishovite, with Implications for Mantle Water Content. *Science* **1993**, *261* (5124), 1024–1026. https://doi.org/10.1126/science.261.5124.1024.

(4) Litasov, K. D.; Kagi, H.; Shatskiy, A.; Ohtani, E.; Lakshtanov, D. L.; Bass, J. D.; Ito, E. High Hydrogen Solubility in Al-Rich Stishovite and Water Transport in the Lower Mantle. *Earth and Planetary Science Letters* **2007**, *262* (3–4), 620–634. https://doi.org/10.1016/j.epsl.2007.08.015.

(5) Swope, R. J.; Smyth, J. R.; Larson, A. C. H in Rutile-Type Compounds: I. Single-Crystal Neutron and X-Ray Diffraction Study of H in Rutile. *American Mineralogist* **1995**, *80* (5–6), 448–453. https://doi.org/10.2138/am-1995-5-604.

(6) Sakaguchi, T.; Kobayashi, Y.; Yajima, T.; Ohkura, M.; Tassel, C.; Takeiri, F.; Mitsuoka, S.; Ohkubo, H.; Yamamoto, T.; Kim, J. eun; Tsuji, N.; Fujihara, A.; Matsushita, Y.; Hester, J.; Avdeev, M.; Ohoyama, K.; Kageyama, H. Oxyhydrides of $(Ca,Sr,Ba)TiO_3$ Perovskite Solid Solutions. *Inorg. Chem.* **2012**, *51* (21), 11371–11376. https://doi.org/10.1021/ic300859n.

(7) Kobayashi, Y.; Hernandez, O. J.; Sakaguchi, T.; Yajima, T.; Roisnel, T.; Tsujimoto, Y.; Morita, M.; Noda, Y.; Mogami, Y.; Kitada, A.; Ohkura, M.; Hosokawa, S.; Li, Z.; Hayashi, K.; Kusano, Y.; Kim, J. eun; Tsuji, N.; Fujiwara, A.; Matsushita, Y.; Yoshimura, K.; Takegoshi, K.; Inoue, M.; Takano, M.; Kageyama, H. An Oxyhydride of $BaTiO_3$ Exhibiting Hydride Exchange and Electronic Conductivity. *Nature Mater* **2012**, *11* (6), 507–511. https://doi.org/10.1038/nmat3302.

(8) Aleksis, R.; Nedumkandathil, R.; Papawassiliou, W.; Carvalho, J. P.; Jaworski, A.; Häussermann, U.; Pell, A. J. Probing the Electronic Structure and Hydride Occupancy in Barium Titanium Oxyhydride through DFT-Assisted Solid-State NMR. *Phys.*

Chem. Chem. Phys. **2022**, *24* (46), 28164–28173. https://doi.org/10.1039/D2CP04675J.

(9) Eklöf-Österberg, C.; Mazzei, L.; Granhed, E. J.; Wahnström, G.; Nedumkandathil, R.; Häussermann, U.; Jaworski, A.; Pell, A. J.; Parker, S. F.; Jalarvo, N. H.; Börjesson, L.; Karlsson, M. The Role of Oxygen Vacancies on the Vibrational Motions of Hydride Ions in the Oxyhydride of Barium Titanate. *J. Mater. Chem. A* **2020**, *8* (13), 6360–6371. https://doi.org/10.1039/C9TA11912D.

(10) Gao, T.; Nian, L.; Jin, L.; Sun, H.; Zhang, T.; Yang, J.; Gu, Z.; Peng, L.; Nie, Y. Giant Switchable Persistent Photoconductivity in Soft Chemistry Reduced $SrTiO_3$. *Adv Elect Materials* **2023**, *9* (7), 2300068. https://doi.org/10.1002/aelm.202300068.

(11) Takeiri, F.; Aidzu, K.; Yajima, T.; Matsui, T.; Yamamoto, T.; Kobayashi, Y.; Hester, J.; Kageyama, H. Promoted Hydride/Oxide Exchange in $SrTiO_3$ by Introduction of Anion Vacancy via Aliovalent Cation Substitution. *Inorg. Chem.* **2017**, *56* (21), 13035–13040. https://doi.org/10.1021/acs.inorgchem.7b01845.

(12) Yajima, T.; Takahashi, K.; Nakajima, H.; Honda, T.; Ikeda, K.; Otomo, T.; Hiroi, Z. High-Pressure Synthesis of Transition-Metal Oxyhydrides with Double-Perovskite Structures. *Inorg. Chem.* **2022**, *61* (4), 2010–2016. https://doi.org/10.1021/acs.inorgchem.1c03162.

(13) Steinsvik, S.; Larring, Y.; Norby, T. Hydrogen Ion Conduction in Iron-Substituted Strontium Titanate, $SrTi_{1-x}Fe_xO_{3-x}$ ($0 \leq x \leq 0.8$). **2001**.

(14) Perdew, J. P.; Burke, K.; Ernzerhof, M. Generalized Gradient Approximation Made Simple. *Phys. Rev. Lett.* **1996**, *77* (18), 3865–3868. https://doi.org/10.1103/PhysRevLett.77.3865.

(15) Perdew, J. P.; Burke, K.; Ernzerhof, M. Generalized Gradient Approximation Made Simple [Phys. Rev. Lett. 77, 3865 (1996)]. *Phys. Rev. Lett.* **1997**, *78* (7), 1396–1396. https://doi.org/10.1103/PhysRevLett.78.1396.

(16) Kresse, G.; Hafner, J. *Ab Initio* Molecular Dynamics for Liquid Metals. *Phys. Rev. B* **1993**, *47* (1), 558–561. https://doi.org/10.1103/PhysRevB.47.558.

(17) Kresse, G.; Furthmüller, J. Efficiency of Ab-Initio Total Energy Calculations for Metals and Semiconductors Using a Plane-Wave Basis Set. *Computational Materials Science* **1996**, *6* (1), 15–50. https://doi.org/10.1016/0927-0256(96)00008-0.

(18) Kresse, G.; Furthmüller, J. Efficient Iterative Schemes for *Ab Initio* Total-Energy Calculations Using a Plane-Wave Basis Set. *Phys. Rev. B* **1996**, *54* (16), 11169–11186. https://doi.org/10.1103/PhysRevB.54.11169.

(19) Kresse, G.; Joubert, D. From Ultrasoft Pseudopotentials to the Projector Augmented-Wave Method. *Phys. Rev. B* **1999**, *59* (3), 1758–1775. https://doi.org/10.1103/PhysRevB.59.1758.

(20) Blöchl, P. E.; Jepsen, O.; Andersen, O. K. Improved Tetrahedron Method for Brillouin-Zone Integrations. *Phys. Rev. B* **1994**, *49* (23), 16223–16233. https://doi.org/10.1103/PhysRevB.49.16223.

(21) Karhánek, D. Dakarhanek/VASP-Infrared-Intensities: VASP-Infrared-Intensities, 2020. https://doi.org/10.5281/ZENODO.3930989.

(22) Lin, S.-T.; Blanco, M.; Goddard, W. A. The Two-Phase Model for Calculating Thermodynamic Properties of Liquids from Molecular Dynamics: Validation for the Phase Diagram of Lennard-Jones Fluids. *The Journal of Chemical Physics* **2003**, *119* (22), 11792–11805. https://doi.org/10.1063/1.1624057.

(23) Lin, S.-T.; Maiti, P. K.; Goddard, W. A. Two-Phase Thermodynamic Model for Efficient and Accurate Absolute Entropy of Water from Molecular Dynamics Simulations. *J. Phys. Chem. B* **2010**, *114* (24), 8191–8198. https://doi.org/10.1021/jp103120q.

(24) Pascal, T. A.; Lin, S.-T.; Goddard III, W. A. Thermodynamics of Liquids: Standard Molar Entropies and Heat Capacities of Common Solvents from 2PT Molecular Dynamics. *Phys. Chem. Chem. Phys.* **2011**, *13* (1), 169–181. https://doi.org/10.1039/C0CP01549K.

(25) Misaki, T.; Oikawa, I.; Takamura, H. Negative Knight Shift in Ba-Ti Oxyhydride: An Indication of the Multiple Hydrogen Occupation. *Chem. Mater.* **2019**, *31* (18), 7178–7185. https://doi.org/10.1021/acs.chemmater.9b01434.

(26) Libowitzky, E. Correlation of O-H Stretching Frequencies and O-H···O Hydrogen Bond Lengths in Minerals. *Chemical Monthly* **1999**, *130*, 1047–1059.

(27) Caracas, R.; Wentzcovitch, R.; Price, G. D.; Brodholt, J. $CaSiO_3$ Perovskite at Lower Mantle Pressures. *Geophysical Research Letters* **2005**, *32* (6), 2004GL022144. https://doi.org/10.1029/2004GL022144.

(28) Chen, H.; Leinenweber, K.; Prakapenka, V.; Prescher, C.; Meng, Y.; Bechtel, H.; Kunz, M.; Shim, S.-H. Possible H_2O Storage in the Crystal Structure of CaSiO3 Perovskite. *Physics of the Earth and Planetary Interiors* **2020**, *299*, 106412. https://doi.org/10.1016/j.pepi.2019.106412.

(29) Jalan, B.; Engel-Herbert, R.; Mates, T. E.; Stemmer, S. Effects of Hydrogen Anneals on Oxygen Deficient $SrTiO_{3-x}$ Single Crystals. *Applied Physics Letters* **2008**, *93* (5), 052907. https://doi.org/10.1063/1.2969037.

(30) Liu, X.; Matsukage, K. N.; Nishihara, Y.; Suzuki, T.; Takahashi, E. Stability of the Hydrous Phases of Al-Rich Phase D and Al-Rich Phase H in Deep Subducted Oceanic Crust. *American Mineralogist* **2019**, *104* (1), 64–72. https://doi.org/10.2138/am-2019-6559.

(31) Nedumkandathil, R.; Jaworski, A.; Grins, J.; Bernin, D.; Karlsson, M.; Eklöf-Österberg, C.; Neagu, A.; Tai, C.-W.; Pell, A. J.; Häussermann, U. Hydride Reduction of $BaTiO_3$ − Oxyhydride Versus O Vacancy Formation. *ACS Omega* **2018**, *3* (9), 11426–11438. https://doi.org/10.1021/acsomega.8b01368.

(32) Hayashi, K.; Sushko, P. V.; Hashimoto, Y.; Shluger, A. L.; Hosono, H. Hydride Ions in Oxide Hosts Hidden by Hydroxide Ions. *Nat Commun* **2014**, *5* (1), 3515. https://doi.org/10.1038/ncomms4515.

(33) Hayashi, K.; Hosono, H. Green Apatites: Hydride Ions, Electrons and Their Interconversion in the Crystallographic Channel. *Phys. Chem. Chem. Phys.* **2016**, *18* (11), 8186–8195. https://doi.org/10.1039/C6CP00515B.

(34) Mao, H.-K.; Hu, Q.; Yang, L.; Liu, J.; Kim, D. Y.; Meng, Y.; Zhang, L.; Prakapenka, V. B.; Yang, W.; Mao, W. L. When Water Meets Iron at Earth's Core–Mantle Boundary. *National Science Review* **2017**, *4* (6), 870–878. https://doi.org/10.1093/nsr/nwx109.

(35) Chao, K.-H.; Berrada, M.; Wang, S.; Peckenpaugh, J.; Zhang, D.; Chariton, S.; Prakapenka, V.; Chen, B. Structure and Equation of State of Ti-Bearing Davemaoite: New Insights into the Chemical Heterogeneity in the Lower Mantle. *American Mineralogist* **2024**. https://doi.org/10.2138/am-2023-9104.

(36) Smith, E. M.; Shirey, S. B.; Nestola, F.; Bullock, E. S.; Wang, J.; Richardson, S. H.; Wang, W. Large Gem Diamonds from Metallic Liquid in Earth's Deep Mantle. *Science* **2016**, *354* (6318), 1403–1405. https://doi.org/10.1126/science.aal1303.

Chapter 7

CONCLUSION

7.1 Summary of Results

The main goal of this thesis was to gain a better understanding of hydrogen's structural state as a defect component of nominally anhydrous minerals and synthetic crystalline materials. Although the chapters survey hydrogen defects of several types in a variety of materials, the two through lines are the techniques of density functional theory and infrared spectroscopy. We have shown that in a variety of contexts, these techniques can be combined in a targeted approach to gain information on hydrogen's structural state.

Beginning with Chapter 2, we were able to use theory to adequately clarify ambiguities and assumptions about ultra hydrous stishovite. In particular, we investigated the assumption that the broad infrared modes observed in this material were a direct consequence of the coexistence of numerous hydrogarnet-like configurations (a distinct possibility, given the octahedral coordination of Si). By exhaustively testing dozens of possible defect configurations, we found that only seven were energetically stable, and of those seven, one should dominate. The most conventionally used vibrational analysis techniques, which don't take temperature into account, predicted hydroxyl stretches and bends with positions within the broad experimentally observed distributions. However, these alone could not account for the shapes of these spectral features. Only with the addition of *ab-initio* molecular dynamics simulations did we find that a single defect state could produce a distribution of vibrations that matched experimental data, supporting the existence of limited defect states in ultrahydrous stishovite. Not only did this study elucidate the structure of the hydroganet-like defect state in stishovite, but it also demonstrated the potential capabilities of DFT to interpret the complex behaviors that are possible in the infrared spectra of hydroxyl defects.

In Chapter 3, we used theory to investigate the interaction between oxygen vacancies and hydrogen in rutile-type TiO_2. When a single hydrogen is introduced to an oxygen-deficient rutile structure, we found that hydrogen migrates to the vacant oxygen

site, bonds to two Ti, and takes on a negative charge. This configuration is energetically preferred over OH^- to an overwhelming degree. Adding another hydrogen atom to this structure gives an equivalent result, with the formation of hydride and hydroxyl favored over the formation of two hydroxyls. Because the Ti-H bond state differs so radically from O-H, the infrared mode for hydride in rutile should be located at a significantly lower wavenumber position, in a region that has been largely neglected by most investigations. This raises many unusual possibilities for hydrogen in rutile and other phases, like "hidden" or overlooked hydrogen, or the implied stability of mixed-valence hydrogen systems. The extreme stability predicted for the hydride ion is particularly intriguing to consider in the context of the reducing deep earth.

Following the calculations from Chapter 3, we carried out experiments on synthetic rutile in Chapter 4 to determine whether the hydride state could be induced and detected. The single crystal samples subjected to H_2 gas treatments across a range of temperatures were studied in detail via complementary methods of ^1H NMR, FTIR, and EPR. Despite the predictions made in the prior chapter, there was no hydride detected in these samples. Thus, rutile would not be the test case for hydride analysis via FTIR that we had hoped for. While this result did appear to contradict our calculations, our experiments did clarify the dynamics between the OH^- and V_O defect states. We were able to ascertain the temperatures over which OH^- versus V_O are dominant, and the point at which rutile will decompose into Magnéli phases, demonstrating how rutile's defect chemistry can be tuned. Additionally, our results imply that hydride states may be more challenging to produce in rutile than is suggested just by theory alone. Despite the enormous, predicted stability of hydride in rutile, creating hydride defects in the lab may only be possible under very specific conditions, which could be the case for other phases as well.

Given the difficulties encountered for hydride detection in rutile, we moved on to analyzing a phase where hydride had already conclusively been observed: $SrTiO_3$ perovskite. In Chapter 5, we documented our efforts to identify structural H^- via FTIR in this phase, with the goal of integrating theory with experiments as a test case for advanced studies on earth-abundant phases. Like in the case of rutile, the powerful combination of FTIR and ^1H NMR was employed to study hydrogen's defect state. However, these

measurements encountered some difficulties. In particular, we found that there was a push and pull between hydride incorporation and hydride detection: incorporating too much hydride could make samples too absorbing for FTIR, while ensuring samples achieved spectral transmission meant not enough hydride was incorporated for ^{1}H NMR detection. Ultimately, this meant that ^{1}H NMR could not serve as a compliment to FTIR, which led us to pursue more detailed spectroscopic studies involving vacuum and deuterium annealing. This led to a confirmation of the Ti-H-Ti stretching mode, the position of which agreed with theory. This work can now serve as a benchmark for future infrared studies of H^- in perovskites, including those of earth-abundant compositions. The good agreement between DFT and experiment was particularly encouraging, as future work on these materials will require accurate predictive capabilities.

Chapter 6 built from the existing knowledge base of structural hydroxyl and hydride in a variety of phases to propose potential methods for hydrogen incorporation in davemaoite. The davemaoite inclusion's complex composition opens the possibility for diverse defect chemistries. Specifically, the high alkali concentration implies the existence of positively charged defect states, which we speculate that either OH^- or H^- could fulfill. We used DFT to investigate these possibilities. Our calculations predicted a limited number of defect configurations resulting from the coupling of Na/K to OH^- and H^-, along with their associated infrared active modes. While hydroxyl-based defects should produce modes in a spectral region largely free from interference, we found that hydride-based defect modes may experience obstruction from largely unavoidable diamond modes. Additionally, by placing these calculations into the context of realistic measurement conditions, we found that substantial concentrations of hydrogen in davemaoite inclusions (on the order of 1000s of μg/g) could be overlooked.

7.2 Future Work

While our experiments in Chapter 4 did not find evidence for hydride in rutile, there are still more experimental conditions to test that could lead to hydride incorporation. First, is the use of a static, rather than flowing H_2 atmosphere. In the context of prior experiments on rutile, this has the potential to produce very different results. Another approach could

be the use of metallic hydrides or hydride salts, although care must be taken with these treatments not to reduce rutile completely into metallic Ti or convert it into a Magnéli phase. In any case, there is still more work to be done to interrogate the possibility of this controversial defect state.

Our calculations in Chapter 6 posit methods for hydrogen incorporation in davemaoite facilitated by Na and K, but experimental verification of these defect complexes is necessary to further study this possibility. Although it is possible that other davemaoite inclusions of similar composition could be discovered for study, the points of ambiguity from our calculations like line shapes and mode positions (for hydride) mean that there could still be barriers to H detection in a natural sample, where analysis conditions are nonideal. Carefully controlled experimental studies probing the solubility of Na, K, OH^-, and H^- in davemaoite using diamond anvil cell techniques will be necessary to provide context for future measurements in natural samples.

As was mentioned in Chapter 6's discussion, one clear target for studies of hydrogen in earth-abundant perovskites is the titanium component. Ti has a high potential solubility in davemaoite, more or less representing a $CaTiO_3$ component of this phase. As we have demonstrated in our work presented here, titanium reduction is a viable mechanism for the incorporation of both hydroxyl and hydride, so Ti-bearing davemaoite could be a candidate for incorporation of both hydrogen ions. $CaTiO_3$ has already demonstrated an ability to incorporate H^- in equivalent concentrations to $SrTiO_3$, so a combined DFT-laboratory study like the one detailed in Chapter 5 is the next logical step. Similarly, a detailed spectroscopic study of H^- in $BaTiO_3$ also makes sense as a follow up study for gaining more insight on the behavior of H^- in perovskites generally.

Beyond just perovskite phases, the topic of hydride in oxide materials undoubtedly presents numerous opportunities for future research activities. Many unknowns remain surrounding the formation of oxyhydrides, including limitations on composition, structure and substitution mechanism. For example, direct substitutions of either OH^- or halogens by H^- have only been investigated in a handful of instances, but these processes could be more common, and provide a viable pathway for converting between OH^- and H^-. Some phases, like MgO, have demonstrated an ability to incorporate small amounts of H^- when

otherwise compositionally pure, but the limits on H^- solubility have not been thoroughly tested. The stability of H^- in silicates has also not been studied in depth, although there are silicate minerals of several compositions that could conceivably facilitate H^- incorporation via reduction, coupled substitution, or halogen-replacing mechanisms. By and large, naturally sourced materials have also not yet been analyzed for H^-, or experimentally doped with H^-, limiting our understanding of how H^- might behave in a more chemically complex and inhomogeneous material. Pursuing these and other lines of research could prove valuable for contextualizing hydride's potential as a component of the mantle.

Appendix A

ADDITIONAL RESULTS AND COMMENTARY FROM CHAPTER II

The contents of this appendix are part of a published article titled "Behavior of Hydrogarnet-Type Defects in Hydrous Stishovite at Various Temperatures and Pressures" by W.R. Palfey, G.R. Rossman, and W.A. Goddard III in the Journal of Geophysical Research, Solid Earth. In this work, W.R. Palfey led the DFT calculations, supervised by both W.A. Goddard III and G.R. Rossman. All authors were involved in designing the study and preparation of the manuscript.

A.1 Notes on defect configurations

There are many possible arrangements for the hydrogarnet defect in stishovite, due to both the mismatch in number of unbonded O atoms and H atoms, and the orthorhombic symmetry of the modified octahedral Si site. The following section is an overview of how starting configurations were derived.

A single Si site was focused on in the 2x2x3 supercell. The O atoms of this Si site were lettered A through F, as shown in **Figure A1**. O atoms E and F are equivalent and form the long axis of the distorted octahedral site. We refer to these as the "axial" atoms. O atoms A through D are also equivalent by symmetry and represent the "equatorial atoms of the site. Although these four atoms are symmetrically equivalent, they form two different O-Si-O angles — thus creating the orthorhombic symmetry of the site.

Preliminary testing of the positions of H revealed that OH will almost universally orient at an angle to *a* and *c*, slightly skewed from the diagonal edges of the octahedral site. Thus, all starting positions for H were chosen in line with this constraint. Given this, there are two possible starting positions for H that forms OH on the equatorial O atoms and four possible positions for H that forms OH on the axial atoms. We denote the H positions on each O atom by a number (see **Figure A1**). By this naming scheme, each of the 16 OH groups can be referred to by a letter-number nomenclature (i.e., "A1", "F3", etc.).

The 16 OH groups can be combined in 64 symmetrically unique groups of four. As discussed in the main text, despite the large number of starting combinations, structural minimization results in just seven OH arrays. **Table A1** summarizes both the starting configurations and the resulting minimized structures, including the energy differences with relation to the most favorable configuration, the tetrahedral case. **Tables A2** and **A3** give atomic coordinates for both the tetrahedral and square planar cases. Diagrams of the final minimized structures (except for the tetrahedral and square planar cases from the main text) are shown in **Figure A2**. The tetrahedral case, which has the lowest energy in the stishovite defect system, is compared to the lowest energy defects for rutile and pyrolusite in **Figure A3.**

Figure A4 presents the phonon DoS for the square planar case at 50 K, showing the behavior of this defect at low temperatures and accounting for the apparent discrepancy between DFPT and QM MD calculations. **Figure A5** shows vibrational density of states from 25 °C to 500 °C for the tetrahedral and square planar cases with the low frequency modes included.

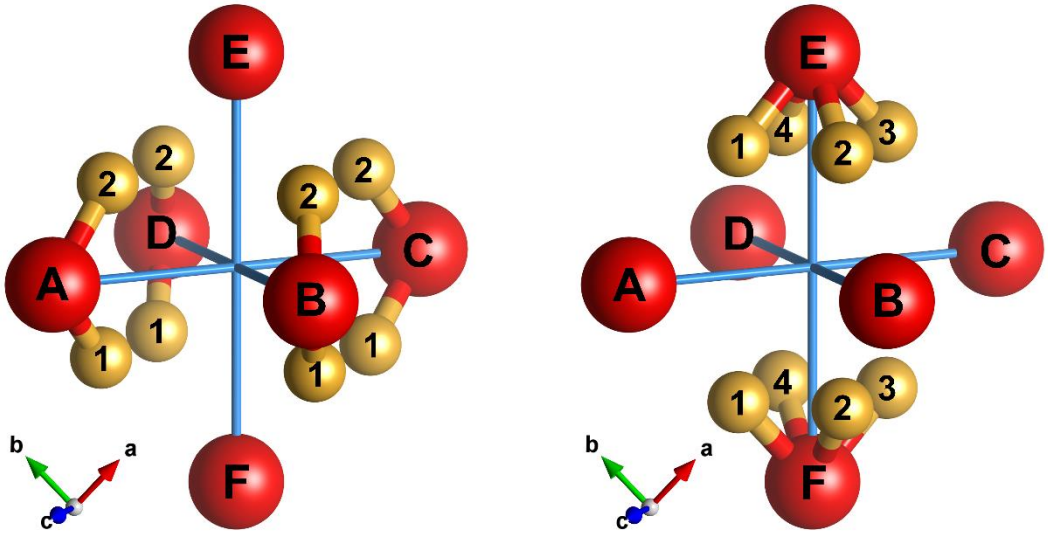

Figure A1. *Diagram showing the 16 possible OH positions, given the constraints discussed in the main text and* ***A.1****. Red spheres represent oxygen and bronze spheres represent hydrogen. On the left, the equatorial O atoms are populated with their respective OH groups, while the axial OH groups are represented on the right.*

Irregular tetrahedral (1): **Irregular tetrahedral (2):** **Square planar (c-parallel):**

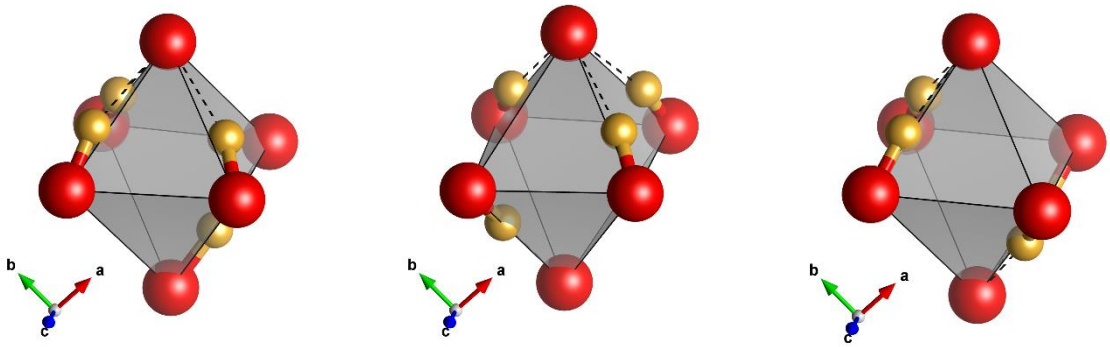

Rotated tetrahedral: **Square planar (quartet):**

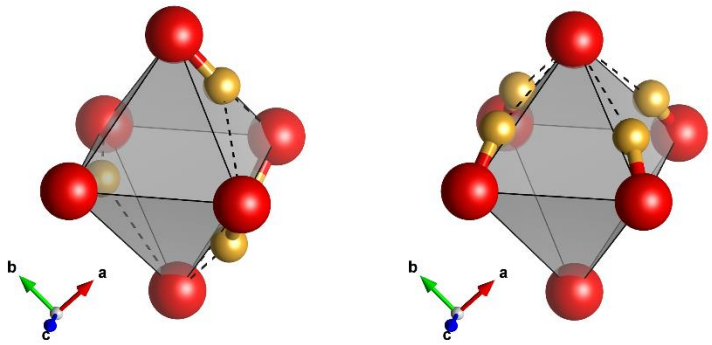

Figure A2. *Diagrams of the five higher energy minimized defect configurations. Red spheres represent oxygen and bronze spheres represent hydrogen. Note that all OH is oriented just off the diagonal of the octahedron except for the rotated tetrahedral case (bottom left). In this case, one axial OH points in between two equatorial O atoms, while another OH points roughly in the c direction.*

Favorable in stishovite: **Favorable in rutile and pyrolusite:** **Favorable in rutile:**

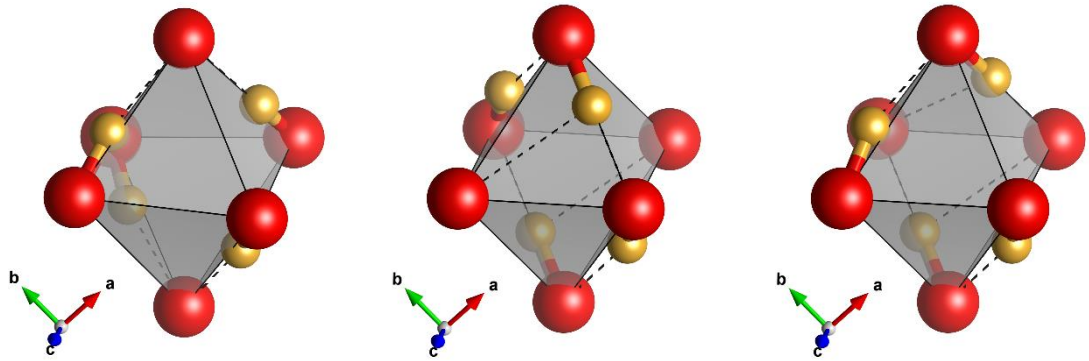

Figure A3. *Comparison of the stable configurations for a hydrogarnet/Reutschi-type defect in three different rutile-structured phases. To the left is the tetrahedral defect in stishovite (this study). In the center is the defect type found to be stable in rutile (TiO_2) and pyrolusite (MnO_2) by Bjørheim et al., 2013 and Balachandran et al., 2003, respectively. On the right is the defect configuration found to be stable in rutile by Bjørheim et al., 2010 and 2013. The center configuration is equivalent to starting positions B1, D2, E2, F4 and the configuration on the right is equivalent to starting positions A2, B1, E3, F4. In both cases, these configurations are unstable in stishovite.*

A.2 Additional results

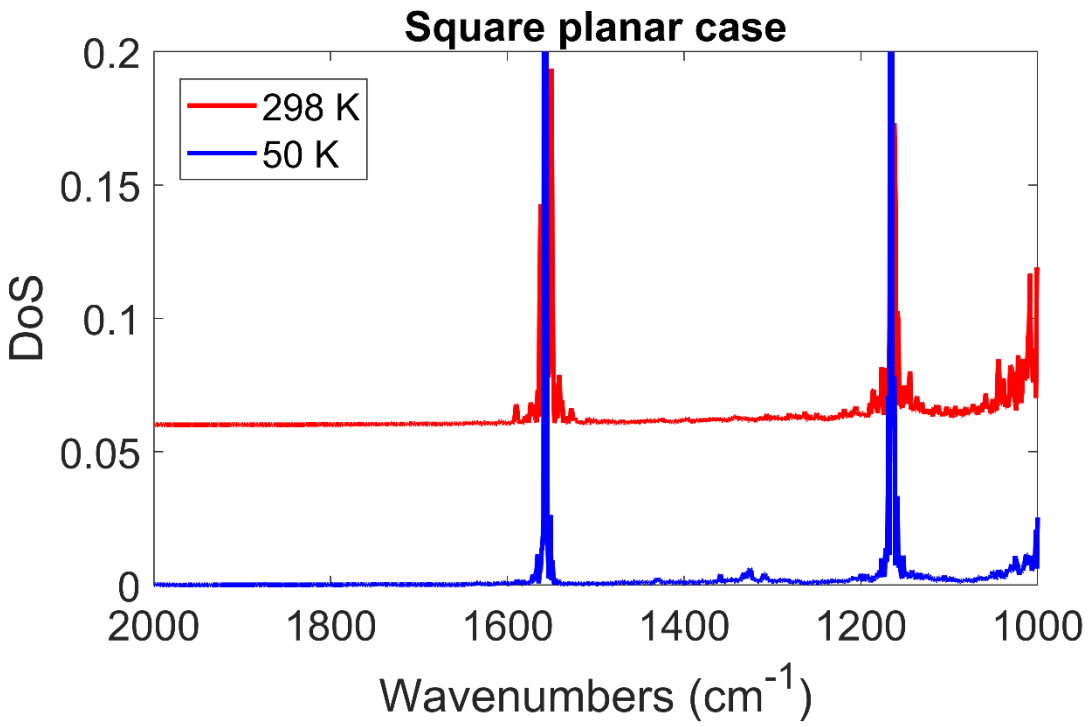

Figure A4. *Comparison of 298 K and 50 K calculations for the square planar case. Although the DFPT calculations predict that modes should be located between ~1400 cm^{-1} and 1300 cm^{-1}, no modes could be observed in this area for the square planar case DoS at any temperature from 25 °C to 500 °C. However, modes do emerge in this region when QM MD is performed at 50 K. This suggests that both the DFPT modes and DoS are accurate; there is just a temperature dependence for modes in this region. Because DFPT is fundamentally a 0 K calculation, the modes will only appear in a DoS derived from a low temperature dynamics calculation.*

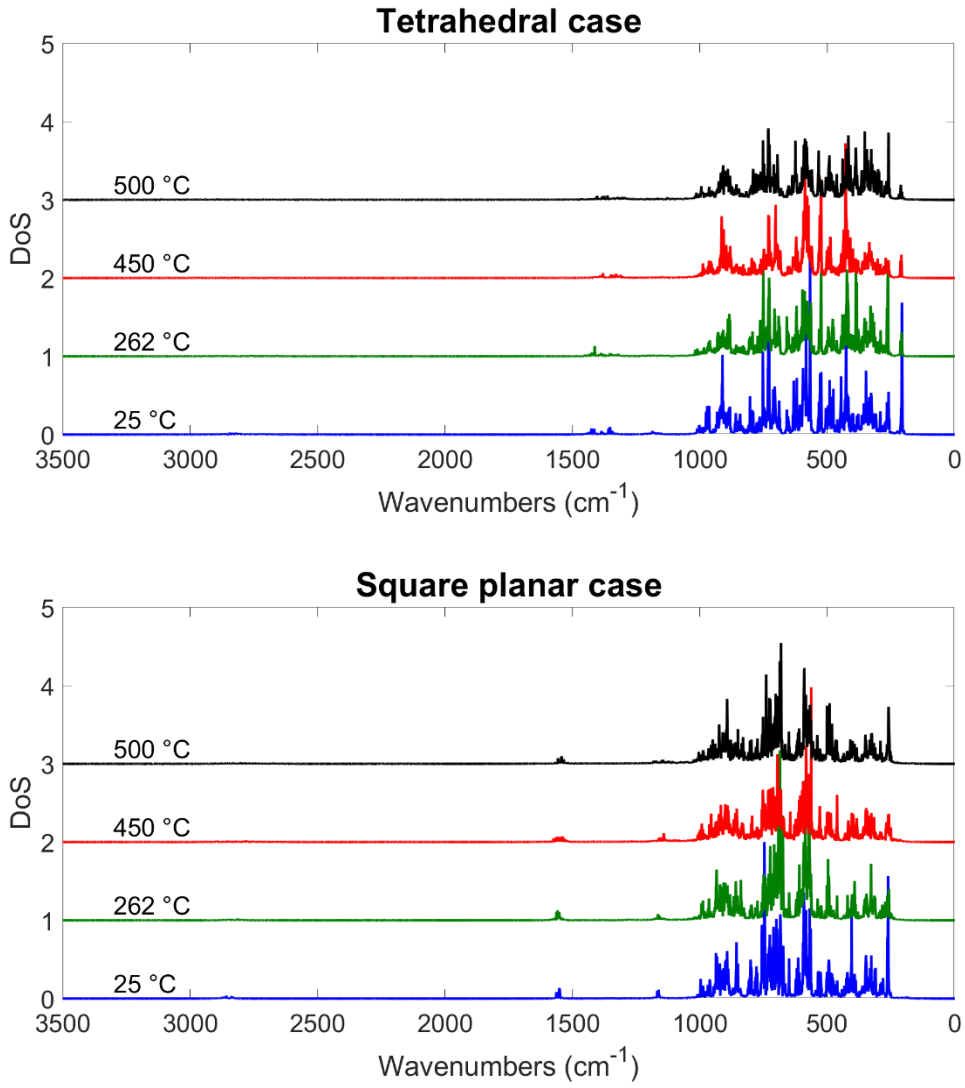

Figure A5. *The full vibrational density of states between 0 and 3500 cm^{-1} for the tetrahedral case (top) and Square planar case (bottom) for each of the temperatures simulated through QM-MD.*

Starting OH combination	**Classification (post minimization)**	**Total energy difference (eV)**
C2, D1, E4, F3	Tetrahedral	*Lowest energy*
C1, D1, A2, B2	Tetrahedral	1.12 E-05
A2, B1, E2, F3	Tetrahedral	3.67 E-04
A2, B1, E3, F1	Tetrahedral	3.69 E-04
A1, B2, C1, E1	Tetrahedral	4.11 E-04
A2, D1, E4, F2	Tetrahedral	4.16 E-04
A2, D1, E3, F1	Tetrahedral	4.18 E-04
A2, D1, E2, F2	Tetrahedral	4.39 E-04
A2, D1, E3, F3	Tetrahedral	4.68 E-04
A1, B2, C1, E3	Tetrahedral	5.69 E-04
A2, D1, E3, F2	Tetrahedral	7.16 E-04
A2, D1, E4, F1	Tetrahedral	7.40 E-04
A1, B2, C1, E4	Tetrahedral	9.67 E-04
A2, B1, E3, F4	Tetrahedral	9.78 E-04
B2, D1, E1, F2	Square planar (c-perpendicular pairs)	0.140
B2, D1, E4, F3	Square planar (c-perpendicular pairs)	0.140
A1, B1, C2, E1	Square planar (c-perpendicular pairs)	0.140
A1, B1, C2, E2	Square planar (c-perpendicular pairs)	0.140
A2, D1, E2, F1	Square planar (c-perpendicular pairs)	0.140
A2, D1, E4, F3	Square planar (c-perpendicular pairs)	0.140
A1, B1, C2, D2	Square planar (c-perpendicular pairs)	0.140
B1, D2, E2, F4	Square planar (c-perpendicular pairs)	0.140

A2, D1, E2, F3	Square planar (c-perpendicular pairs)	0.140
B2, D1, E1, F3	Square planar (c-perpendicular pairs)	0.140
A1, B1, C2, E4	Square planar (c-perpendicular pairs)	0.140
A1, B2, C2, E1	Irregular tetrahedral 1	0.503
A2, B1, C2, E4	Irregular tetrahedral 1	0.504
A1, B1, C1, D2	Irregular tetrahedral 1	0.504
A2, B2, C1, E4	Irregular tetrahedral 1	0.504
A1, B2, C2, E4	Irregular tetrahedral 1	0.504
A1, B1, C1, E1	Irregular tetrahedral 2	0.517
A2, B2, E3, F1	Irregular tetrahedral 2	0.517
B2, D2, E3, F4	Irregular tetrahedral 2	0.517
A1, B1, C1, E4	Irregular tetrahedral 2	0.518
A2, D2, E3, F3	Irregular tetrahedral 2	0.518
B2, D2, E3, F1	Irregular tetrahedral 2	0.518
A2, B2, E3, F4	Irregular tetrahedral 2	0.518
A2, D2, E3, F2	Irregular tetrahedral 2	0.518
A2, B1, C1, E4	Square planar (c-parallel pairs)	0.667
A2, B1, E4, F3	Square planar (c-parallel pairs)	0.667
A1, D1, B2, C2	Square planar (c-parallel pairs)	0.667
B2, D1, E3, F1	Square planar (c-parallel pairs)	0.667
A2, B1, C1, E2	Rotated tetrahedral	0.725
A2, B1, E4, F1	Rotated tetrahedral	0.725
A1, B1, C1, E2	Rotated tetrahedral	0.725
A2, B1, E2, F3	Rotated tetrahedral	0.725

A2, B1, C1, E3	Rotated tetrahedral	0.725
B2, D1, E3, F3	Rotated tetrahedral	0.725
B2, D1, E1, F1	Rotated tetrahedral	0.725
B2, D1, E4, F1	Rotated tetrahedral	0.725
B2, D1, E3, F2	Rotated tetrahedral	0.725
A2, B1, E3, F3	Rotated tetrahedral	0.725
A1, B1, C1, E3	Rotated tetrahedral	0.725
A2, B1, E4, F4	Rotated tetrahedral	0.725
A2, B2, E3, F2	Rotated tetrahedral	0.725
B2, D2, E3, F2	Rotated tetrahedral	0.725
A2, D2, E3, F1	Rotated tetrahedral	0.725
A2, B1, C2, E2	Rotated tetrahedral	0.726
B2, D2, E3, F3	Rotated tetrahedral	0.726
A2, D2, E3, F4	Rotated tetrahedral	0.726
A2, B2, E3, F3	Rotated tetrahedral	0.726
A2, B2, C1, E3	Rotated tetrahedral	0.726
A1, B1, C1, D1	square planar (quartet)	1.306
A2, B2, C2, E4	square planar (quartet)	1.307

Table A1. *Results of all 64 structural relaxations. Starting combinations of OH (as designated in A.1 and Figure A1) are presented in the first column. The resulting defects are listed in order of increasing energy, with the energy difference from the most favorable case presented in the last column. Note that minimization rarely results in protonation of the same O atoms as the starting structure.*

Atom	a	b	c
H1	2.457	1.229	-0.690
H2	0.168	1.397	-0.690
H3	1.395	0.169	0.688
H4	1.230	2.457	0.688
O1	2.213	0.511	-1.372
O2	0.412	2.115	-1.372
O3	2.113	0.411	1.371
O4	0.512	2.214	1.371
O5	2.625	2.626	0.000
O6	0.000	0.000	0.000

Table A2. *Positions of H and O atoms in the tetrahedral defect, given in units of angstroms with the origin placed at O6 (an axial oxygen).*

Atom	a	b	c
H1	1.418	0.134	0.619
H2	2.491	1.207	-0.753
H3	1.207	2.491	-0.753
H4	0.134	1.418	0.619
O1	2.217	0.502	-1.439
O2	0.502	2.217	-1.439
O3	2.122	0.408	1.305
O4	0.408	2.122	1.305
O5	2.625	2.625	-0.134
O6	0.000	0.000	0.000

Table A3. *Positions of H and O atoms in the square planar defect, given in units of angstroms with the origin placed at O6 (an axial oxygen).*

Appendix B

ADDITIONAL RESULTS FROM CHAPTER III

The contents of this appendix are part of a published article titled "Structure, Energetics and Spectra for the Oxygen Vacancy in Rutile: Prominence of the Ti-H_O-Ti Bond" by W.R. Palfey, G.R. Rossman, and W.A. Goddard III in the Journal of Physical Chemistry Letters. In this work, W.R. Palfey led the DFT calculations, supervised by both W.A. Goddard III and G.R. Rossman. All authors were involved in designing the study and preparation of the manuscript.

B.1 Additional figures and tables

Table B.1. *The energies, hydrogen bonding distances and hydrogen bond angles for all 21 of the single H defects. Ending positions of "Hi" are all CC oriented.*

Defect site	Final H position	Total energy (eV)	d(OH···O) (Å)	Ti-O-H angle
H_{A2}	H_O	-432.066	N/A	N/A
H_{K2}	H_i	-430.647	2.95	173.0
H_{D3}	H_i	-430.629	2.83	174.3
H_{M2}	H_i	-430.623	2.95	173.2
H_{E4}	H_i	-430.577	2.91	172.7
H_{G3}	H_i	-430.550	2.83	172.8
H_{J3}	H_i	-430.539	2.96	172.0
H_{H4}	H_i	-430.501	2.90	171.7
H_{F3}	H_i	-430.489	2.97	172.4
H_{J4}	H_i	-430.488	3.21	168.3
H_{B2}	H_i	-430.484	3.00	173.4
H_{I3}	H_i	-430.478	3.01	171.4
H_{H3}	H_i	-430.47	3.08	171.3
H_{F4}	H_i	-430.443	2.96	172.4
H_{I4}	H_i	-430.44	2.95	175.7
H_{E3}	H_i	-430.385	N/A	N/A
H_{D4}	H_i	-430.374	2.88	164.4
H_{G4}	H_i	-430.37	2.96	170.1
H_{C2}	H_i	-430.295	2.94	173.1
H_{L2}	H_i	-430.238	2.96	175.2
H_{N2}	H_i	-430.187	2.95	172.9

Table B.2. *The energies, hydrogen bonding distances, hydrogen bond angles and average Ti-H distances for all 21 of the two H defects. Ending positions of "H_i" are all CC oriented.*

Defect sites	Final H positions	Total energy (eV)	d(OH···O) (Å)	Avg. Ti-H (Å)	Ti-O-H angle	
H_{A2}, H_{M2}	H_O, H_i	-435.093	2.94	2.04	173.1	
H_{A2}, H_{E4}	H_O, H_i	-435.085	2.91	2.03	173.1	
H_{A2}, H_{K2}	H_O, H_i	-435.084	2.96	2.03	173.4	
H_{A2}, H_{G3}	H_O, H_i	-435.074	2.83	2.04	174.9	
H_{A2}, H_{D3}	H_O, H_i	-435.070	2.81	2.04	173.6	
H_{A2}, H_{F3}	H_O, H_i	-435.041	2.95	2.04	172.8	
H_{A2}, H_{I3}	H_O, H_i	-435.037	2.89	2.03	173.5	
H_{A2}, H_{J3}	H_O, H_i	-435.023	2.92	2.04	173.1	
H_{A2}, H_{H4}	H_O, H_i	-435.017	2.92	2.03	173.4	
H_{A2}, H_{J4}	H_O, H_i	-435.015	3.04	2.04	171.4	
H_{A2}, H_{B2}	H_O, H_i	-435.000	2.91	2.04	173.6	
H_{A2}, H_{D4}	H_O, H_i	-434.961	2.97	2.03	169.5	
H_{A2}, H_{G4}	H_O, H_i	-434.959	2.91	2.04	174.0	
H_{A2}, H_{L2}	H_O, H_i	-434.856	2.90	1.96	173.0	
H_{A2}, H_{N2}	H_O, H_i	-434.839	2.89	1.98	173.2	
H_{A2}, H_{C2}	H_O, H_i	-434.797	2.84	1.97	175.8	
Defect sites	**Final H positions**	**Total energy (eV)**	**d(OH···O) 1 (Å)**	**d(OH···O) 2 (Å)**	**Ti-O-H angle 1**	**Ti-O-H angle 2**
H_{D3}, H_{M2}	H_i, H_i	-433.671	2.82	2.83	176.1	174.8
H_{K2}, H_{G3}	H_i, H_i	-433.588	2.91	2.94	173.1	171.6
H_{D3}, H_{K2}	H_i, H_i	-433.579	2.87	2.99	175.3	172.6
H_{D3}, H_{G3}	H_i, H_i	-433.491	2.61	2.75	170.7	173.0
Defect sites	**Final H positions**	**Total energy (eV)**	**d(OH···O) (Å)**	**Avg. Ti-H (Å)**	**Ti-O-H angle**	
H_{K2}, H_{M2}	H_i, H_{alt}	-432.258	3.03	1.81	171.7	

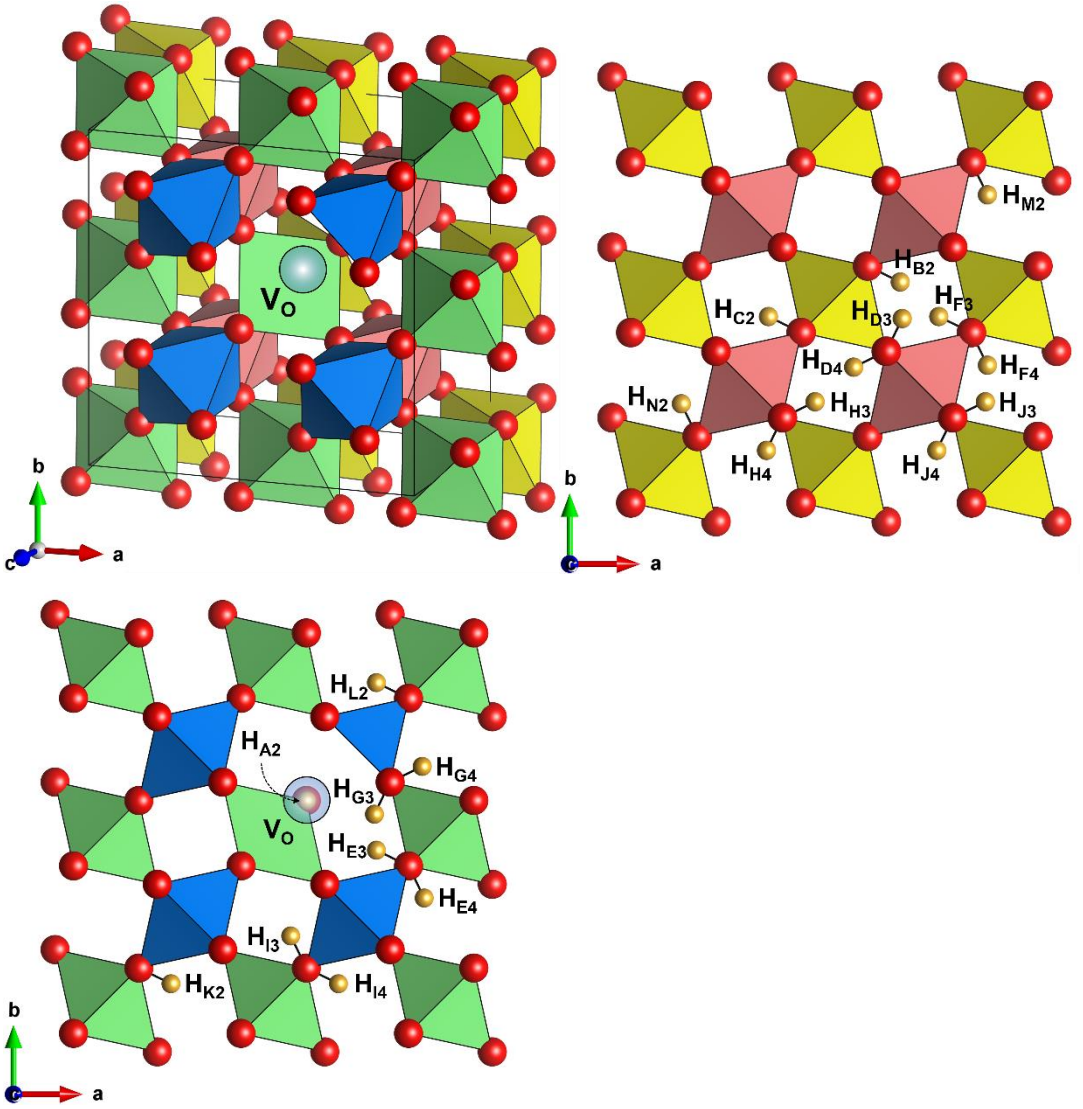

Figure B.1. *Comprehensive summary of the O vacancy structure and H positions from fully relaxed structures with one O vacancy and one added H. Octahedral Ti sites are color coded by layer in the c-direction. O atoms are represented by red spheres, H atoms by bronze spheres, and the O vacancy (VO) by a transparent blue sphere. All OH-bonds are in a channel-centered orientation. Upon structural relaxation, H starting in the A2 position moves to the O vacancy, rather than forming an OH bond. All 21 final positions for H are presented. There are four layers ordered in the c direction: gold, red, green, and blue in sequence. The O vacancy is in the blue layer.*

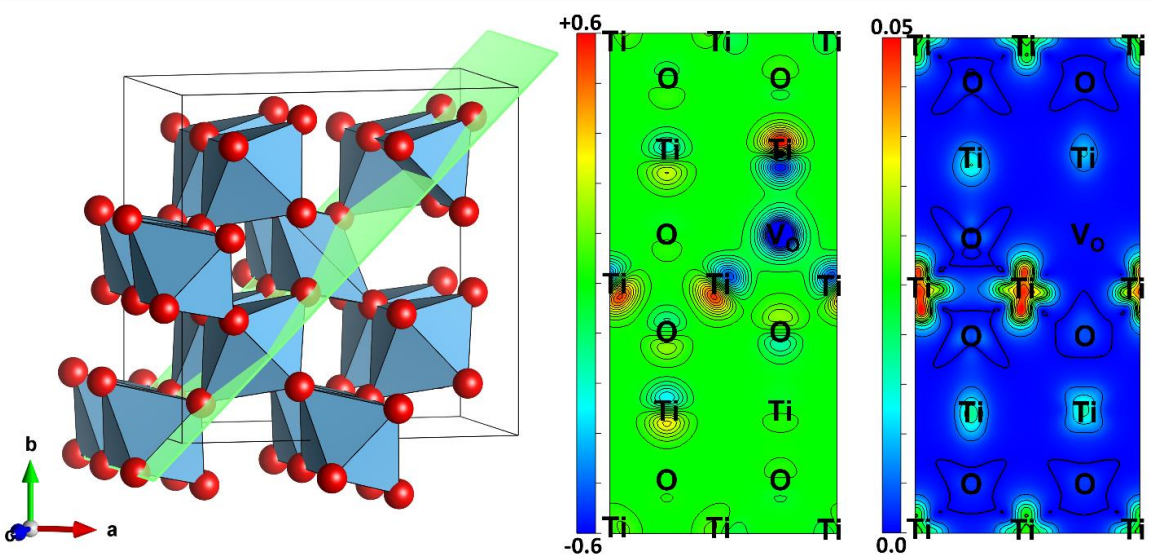

Figure B.2. *Charge and spin densities for the O vacancy system with no added H. Left: the (-110) plane, over which the charge and spin densities are plotted, is highlighted in green. Center: The charge density difference between the O vacancy structure and a perfect rutile crystal. A significant loss of charge is attributed to the O vacancy. Right: The absolute value spin density for the O vacancy structure. Despite similar changes in charge between the three Ti atoms surrounding the O vacancy, the unpaired spin is mostly limited to the two atoms adjacent in the c direction. The shape of the spin density surrounding these Ti atoms suggests occupation of the dxy orbital. Additionally, some unpaired spin is predicted to occupy Ti atoms further away from the O vacancy, also adjacent in the c direction.*

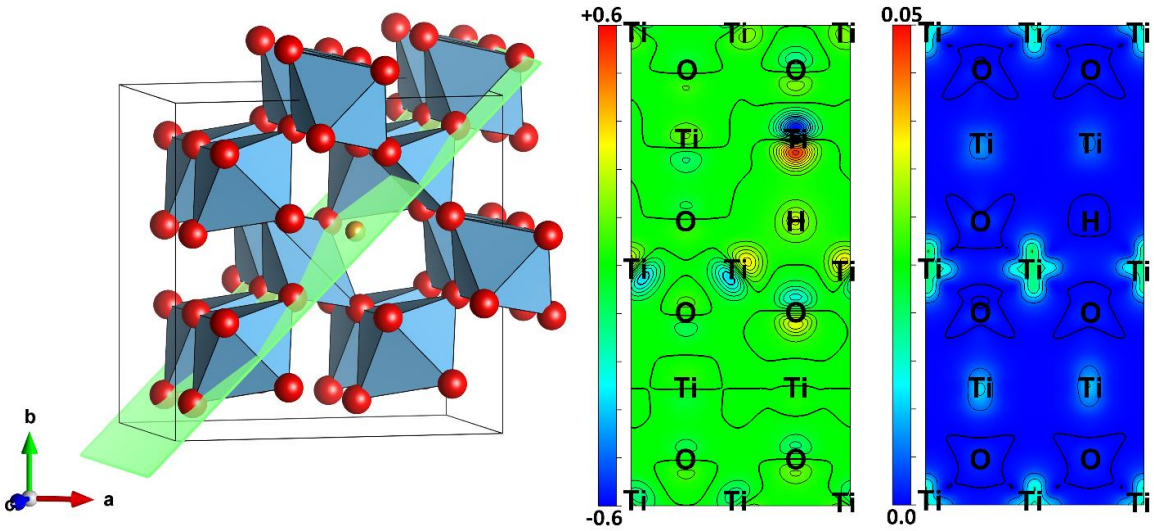

Figure B.3. *Charge and spin densities for the H_O defect for the case of one H added to the O vacancy structure.* ***Left:*** *the (-110) plane, over which the charge and spin densities are plotted, is highlighted in green.* ***Center:*** *The charge density difference between the H_O and O vacancy structure. As expected, there is an increase in charge associated with the inclusion of H. Of the three Ti atoms surrounding H_O, the one furthest away experiences the greatest net increase in charge, while the two closer Ti atoms experience a relatively modest charge increase.* ***Right:*** *The absolute value spin density for the H_O structure. Similar to the O vacancy structure, most of the unpaired spin is on the two Ti atoms adjacent in the c direction, while virtually none is associated with the third H-adjacent Ti atom. This shows the bonding between H_O and the two adjacent Ti atoms in the c-direction.*

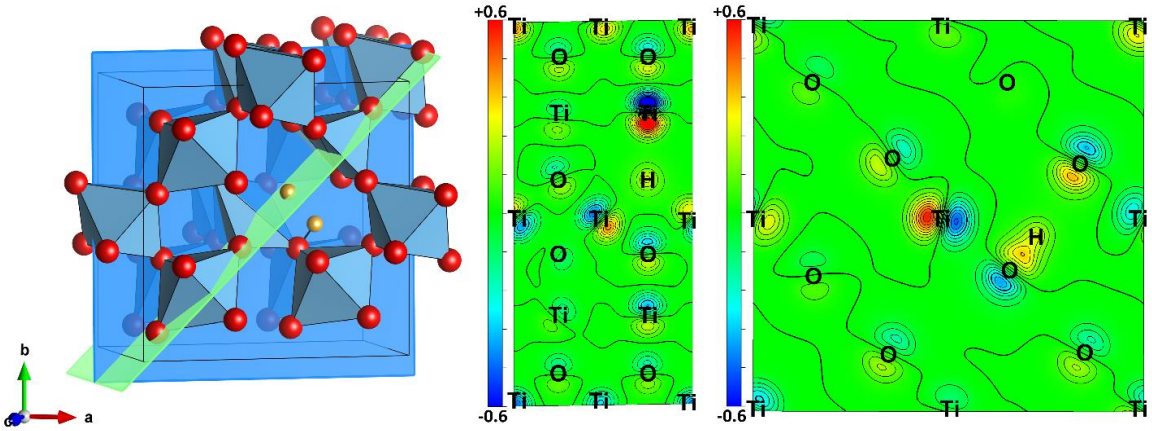

Figure B.4. *Two H added to O vacancy structure. Charge densities for the H_O defect and OH in the 2H system with the OH bond at the D3 site. Spin density plots are not presented, as virtually no unpaired spin was predicted in these systems. Left: The (-110) and plane (green) and (002) plane (blue), over which the charge density differences have been plotted. Center: The charge density difference in the plane of H_O and its surrounding Ti atoms. The charge distribution is largely similar to the single H_O case. Right: The absolute value spin density is plotted to highlight the charge densities associated with the OH bond. A continuous positive charge volume exists between H and its bonded O, revealing the covalent character of the OH bond. This is in stark contrast with H_O in the same structure.*

Table B.3. *Results of Bader charge analyses for the H_i positioned hydrogen atom in the 2H defects. Both the charge values and Bader volumes are significantly lower than for H_O, consistent with the formation of OH.*

Defect Sites	**H_i Charge**	**H_i Volume (Å^3)**
H_{A2}, H_{M2}	0.356	1.345
H_{A2}, H_{E4}	0.375	1.359
H_{A2}, H_{K2}	0.369	1.375
H_{A2}, H_{G3}	0.364	1.310
H_{A2}, H_{D3}	0.366	1.288
H_{A2}, H_{F3}	0.354	1.309
H_{A2}, H_{I3}	0.372	1.347
H_{A2}, H_{J3}	0.371	1.342
H_{A2}, H_{H4}	0.380	1.378
H_{A2}, H_{J4}	0.393	1.476
H_{A2}, H_{B2}	0.361	1.304
H_{A2}, H_{D4}	0.390	1.440
H_{A2}, H_{G4}	0.372	1.353
H_{A2}, H_{L2}	0.364	1.327
H_{A2}, H_{N2}	0.370	1.327
H_{A2}, H_{C2}	0.360	1.281
AVERGE	0.370	1.348

Table B.4. *Results of Bader charge analyses for the H_O positioned hydrogen atom in the 2H defects and H_{A2}. Both the charge values and Bader volumes are significantly higher than for H_i, consistent with anionic hydrogen.*

DEFECT	H_O CHARGE	H_O VOLUME (Å^3)
H_{A2}, H_{M2}	1.571	8.157
H_{A2}, H_{E4}	1.578	8.126
H_{A2}, H_{K2}	1.572	8.061
H_{A2}, H_{G3}	1.569	7.868
H_{A2}, H_{D3}	1.563	7.891
H_{A2}, H_{F3}	1.579	8.203
H_{A2}, H_{I3}	1.575	8.174
H_{A2}, H_{J3}	1.570	8.126
H_{A2}, H_{H4}	1.572	8.131
H_{A2}, H_{J4}	1.572	8.179
H_{A2}, H_{B2}	1.567	8.235
H_{A2}, H_{D4}	1.574	8.247
H_{A2}, H_{G4}	1.580	8.403
H_{A2}, H_{L2}	1.573	7.595
H_{A2}, H_{N2}	1.578	7.800
H_{A2}, H_{C2}	1.573	7.746
H_{A2}	1.567	8.174
AVERAGE	1.573	8.066

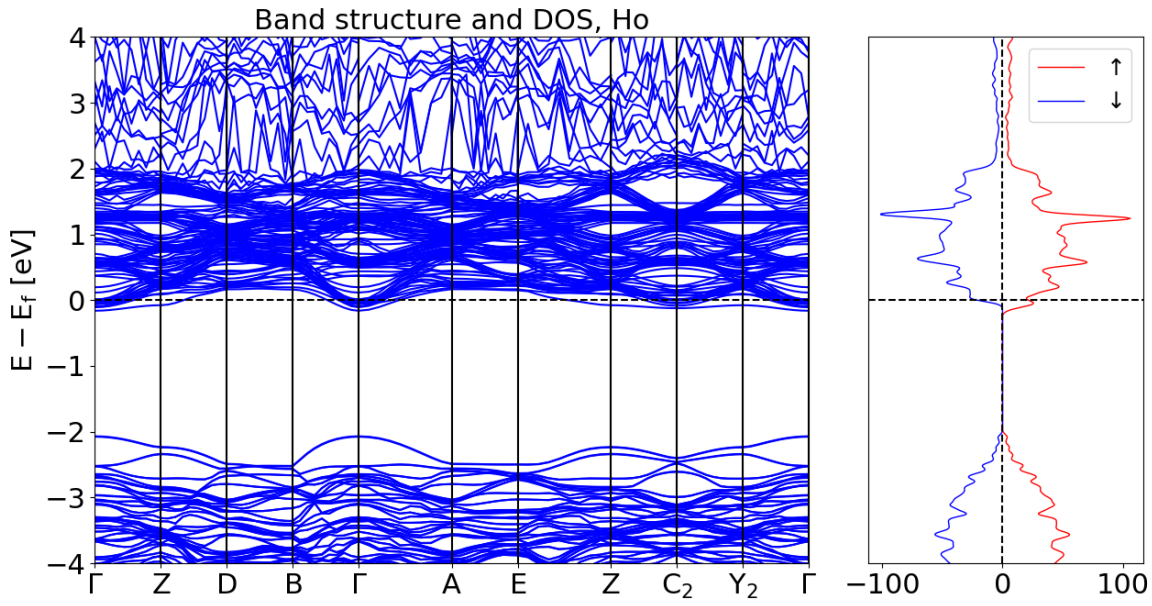

Figure B.5. *Band structure (left) and density of states (right) for the single hydrogen, H_O defect (H_{A2} case). Note the states and unpaired spin present just below the Fermi energy. This is attributed to the excess electrons resulting from V_O which have been delocalized across Ti atoms throughout the structure. The largest portion of the unpaired spin and excess charge is confined to the two Ti atoms bonded to H_O.*

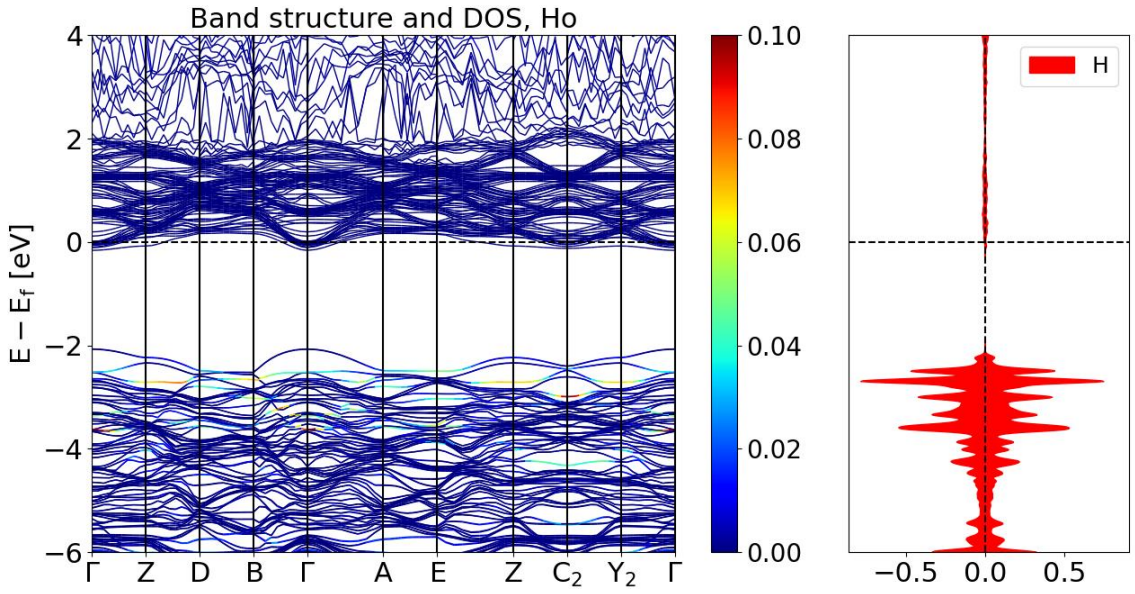

Figure B.6. *Band structure (left) and density of states (right) for the single hydrogen, H_O defect (H_{A2} case). Only the states attributed to H are plotted on the right, and the corresponding bands are highlighted on the left, with warmer colors indicating higher levels of occupation. The Ti_{dxy}-H_s-Ti_{dxy} to Ti_{dxy}-Ti_{dxy} transition is measured from the highest H band to the Ti bands present just below the Fermi energy.*

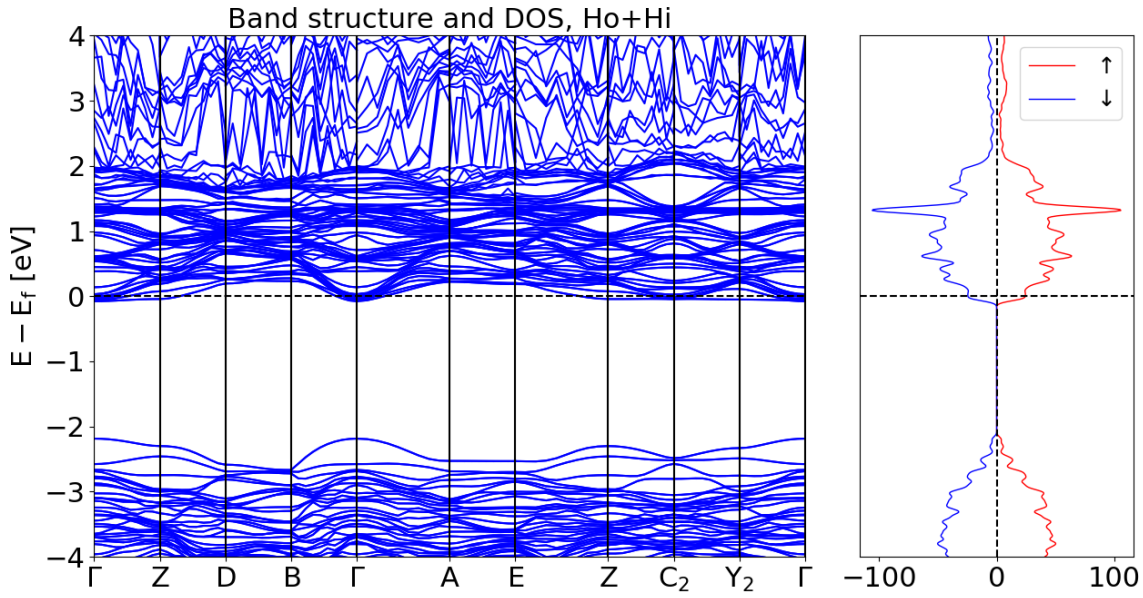

Figure B.7. *Band structure (left) and density of states (right) for the two hydrogen, H_O + H_i defect system (H_{A2}, H_{M2} case). Note the states present just below the Fermi energy, similar to the single hydrogen case. However, in contrast to the single hydrogen case, this system has no unpaired spins. The largest portion of the excess charge resulting from V_O is confined to the two Ti atoms bonded to H_O, with the remained being delocalized across other Ti pairs.*

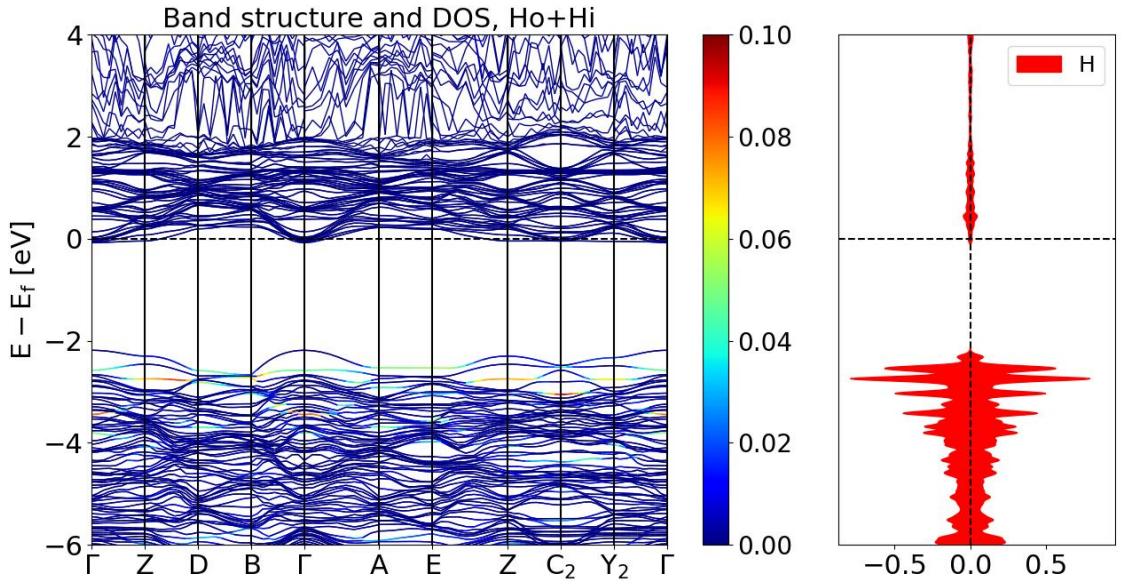

Figure B.8. *Band structure (left) and density of states (right) for the two hydrogen, H_O + H_i defect system (H_{A2}, H_{M2} case). Only the states attributed to H are plotted on the right, and the corresponding bands are highlighted on the left, with warmer colors indicating higher levels of occupation. The Ti_{dxy}-H_s-Ti_{dxy} to Ti_{dxy}-Ti_{dxy} transition is again measured from the highest H band to the Ti bands present just below the Fermi energy, similar to the single hydrogen case.*

Table B.5. *All calculated H-associated vibrational modes are presented above. Emphasis was placed on calculating modes for either structures with unusual geometries (i.e. short or long bond lengths) or the lowest energy structures (i.e. those with Boltzmann factors of 0.05 or more at 25 C).*

Defect site	**OH mode (cm^{-1})**	**Ho mode (cm^{-1})**	**25 ˚C Boltzmann Factor**
H_{A2}	N/A	1198.1	1.00
H_{K2}	3316.3	N/A	1.02E-24
H_{D3}	3171.7	N/A	5.01E-25
H_{M2}	3287.1	N/A	4.06E-25
H_{E4}	3242.5	N/A	6.75E-26
H_{G3}	3118.6	N/A	2.35E-26
H_{J4}	3454.8	N/A	2.09E-27
H_{B2}	3330.9	N/A	1.78E-27
H_{I3}	3339.5	N/A	1.40E-27
H_{H3}	3383.5	N/A	1.04E-27
Defect sites	**OH mode (cm^{-1})**	**Ho mode (cm^{-1})**	**25 ˚C Boltzmann Factor**
H_{A2}, H_{M2}	3270.3	1201.5	1.000
H_{A2}, H_{E4}	3251.4	1239.7	0.715
H_{A2}, H_{K2}	3298.8	1243.1	0.700
H_{A2}, H_{G3}	3151.3	1212.5	0.465
H_{A2}, H_{D3}	3130.8	1211.3	0.408
H_{A2}, H_{F3}	3295.7	1220.0	0.131
H_{A2}, H_{I3}	3238.6	1210.2	0.112
H_{A2}, H_{J3}	3259.3	1197.9	0.065
H_{A2}, H_{H4}	3267.7	1196.0	0.051
H_{A2}, H_{J4}	3364.9	1217.9	0.047
H_{A2}, H_{B2}	3255.4	1216.7	0.027
H_{A2}, H_{D4}	3279.4	1224.6	5.81E-03
H_{A2}, H_{G4}	3231.5	1214.7	5.47E-03
H_{A2}, H_{L2}	3194.7	1503.0	9.74E-05
H_{A2}, H_{N2}	3188.8	1328.2	5.03E-05
H_{A2}, H_{C2}	3088.3	1301.7	1.00E-05
Defect sites	**OH mode 1 (cm^{-1})**	**OH mode 2 (cm^{-1})**	**25 ˚C Boltzmann Factor**

H_{D3}, H_{G3}	2798.5	3003.0	8.42E-28
Defect sites	**OH mode (cm^{-1})**	**25 ˚C Boltzmann Factor**	
H_{K2}, H_{M2}	3370.2	1.21E-48	

A.2 Commentary on the relation between d(OH···O) and OH frequencies

Figure S9 compares our predicted OH stretching frequencies and hydrogen bonding distances to the relation derived by Libowitzky et al. (1999). Although the trends are generally similar (longer bonding distances correspond to higher wavenumber vibrations), the behavior of our calculated modes deviates somewhat from the experimental observations. These systemic errors in the OH modes may arise from the PBE level of DFT. Although the energies of the vibrational modes we report here are likely close to their true values (within ~100 cm^{-1}), we suggest that these calculations may lack the accuracy required to confidently identify defects contributing to specific vibrational modes.

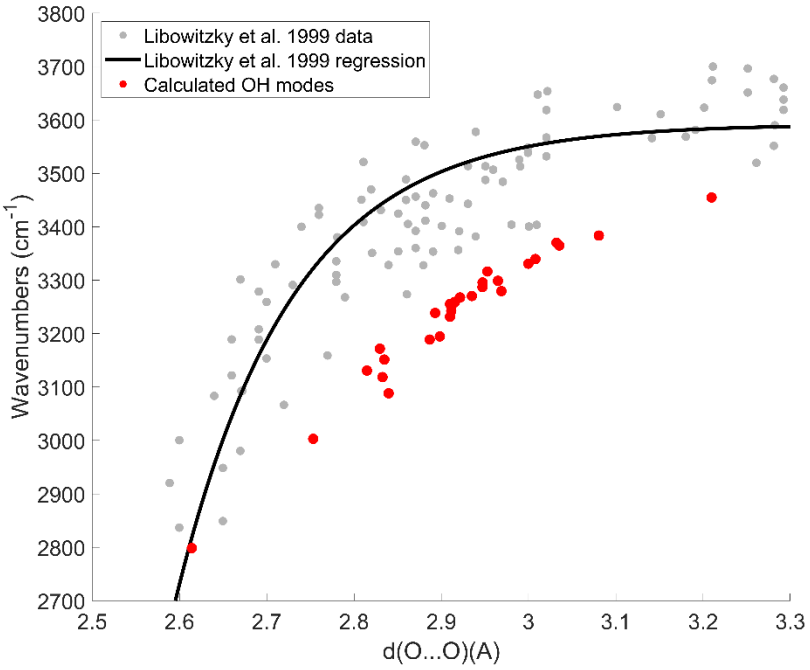

Figure B.9. *Plot of hydrogen bonding distance (d(OH···O)) versus DFPT-calculated OH stretching frequencies for both 1H and 2H defects (red) compared to the survey data and regression curve from Libowitzky et al., 1999 (gray and black, respectively). Although the two datasets show similar trends, the DFPT calculated modes generally lie outside the experimental data scatter, suggesting a possible underestimation of frequency for given d(OH···O) values.*

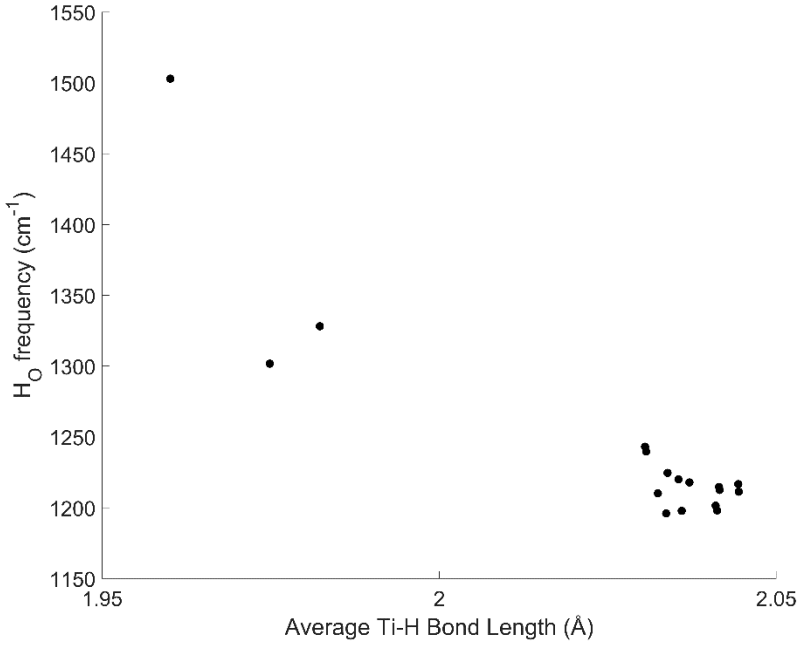

Figure B.10. *Plot of average Ti-H distance versus DFPT-calculated HO stretching frequencies. Although most of the HO frequencies are clustered in a narrow range of Ti-H distances, expanding the plot to include unusually short Ti-H lengths reveals the response of HO frequencies to bonding lengths. The overall relation mimics trends observed in other types of bonds, further supporting the possibility of H bonded to Ti.*